

Scuola Normale Superiore



Ph.D. Thesis

In Biophysical Sciences

**Structural and functional alterations of the kinase domain: impact  
on membrane trafficking of receptor tyrosine kinases**

*Candidate*

Rosy Amodeo

*Advisor*

Laura Marchetti

Supervisor

Stefano Luin

2020

*“La saga del NGF  
prospettata con la dovuta umiltà come paradigmatica del decorso a tappe successive delle ricerche scientifiche  
ha seguito un percorso tortuoso non programmato e imperfetto.  
Come tale avvalorà il concetto che l'imperfezione e non la perfezione sono alla base dell'operato umano.”*

Elogio dell'imperfezione, Rita Levi Montalcini

## Foreword

This thesis is the result of my research activity at the NEST Laboratory of Scuola Normale Superiore in Pisa. I started to work on TrkA receptor tyrosine kinase during my master thesis in 2014. I continued and extended my studies during my PhD in Biophysical Sciences at NEST since 2015. This research activity was performed within a joint PhD program sponsored by Scuola Normale Superiore and Istituto Italiano di Tecnologia.



# CONTENTS

---

LIST OF ABBREVIATIONS	7
LIST OF PUBLICATIONS	10
INTRODUCTION	11
1. TRKA AS A PARADIGM OF HUMAN TYROSINE KINASE RECEPTORS	14
<b>1.1 Tyrosine Kinase Receptors .....</b>	<b>14</b>
1.1.1 Structural architecture of RTKs	15
1.1.2 The Tyrosine kinase domain	16
1.1.3 Mechanisms of activation and autoinhibition of RTKs	19
1.1.4 The family of pseudokinases	23
<b>1.2 TrkA receptor and the Neurotrophin signaling network.....</b>	<b>24</b>
1.2.1 TrkA structure and signaling	26
1.2.2 TrkA mechanism of activation	29
1.2.3 TrkA trafficking	30
1.2.4 TrkA ubiquitination	32
1.2.5 The involvement of TrkA receptor in HSAN IV disease	33
<b>1.3 VEGFR2 Receptor structure and mechanism of activation.....</b>	<b>36</b>
<b>1.4 Experimental strategies to detect RTKs kinase activity: from biochemical to advanced imaging approaches.....</b>	<b>37</b>
1.4.1 Single-molecule imaging and tracking of membrane receptors	40
2. MOLECULAR INSIGHT ON THE ALTERED MEMBRANE TRAFFICKING OF TRKA KINASE DEAD MUTANTS	48
<b>2.1 Background and rationale of the work .....</b>	<b>48</b>

2.2	valuation of membrane mobility and surface exposure of dead-kinase receptors .....	49
2.3	A structural rearrangement is responsible for TrkA-K547N membrane immobilization .....	54
2.4	TrkA-K547N membrane mobility depends on the integrity of cortical actin .....	60
2.5	Role of TrkA post-translational modifications on NGF-induced membrane-related dynamics and functions .....	62
2.6	Concluding remarks .....	66
3.THE HSAN IV RELATED TRKA-R649W MUTANT: EVIDENCE FOR DELAYED DEGRADATION AND CYTOSOLIC ACCUMULATION OF AUTOPHAGOSOMAL VESICLES		68
3.1	BACKGROUND AND RATIONALE OF THE WORK .....	68
3.2	Membrane and intracellular trafficking of TrkA-R643W in DRG neurons .....	69
3.3	Involvement of TrkA-R649W in the alteration of autophagic flux .....	73
3.4	Concluding remarks .....	75
4.MATERIALS AND METHODS		76
4.1	Constructs .....	76
4.2	Immortalized and primary cell cultures and transfection .....	77
4.3	Preparation of viral stocks for neurotrophin receptors .....	79
4.4	Transduction of immortalized and primary cells .....	79
4.5	Immunoblotting and Immunoprecipitation .....	80
4.6	TrkA detection by immunofluorescence.....	81
4.7	Drug treatments.....	82
4.8	FluoNGF binding assay .....	83
4.9	Differentiation assay .....	83

4.10	SFP synthase production and purification .....	84
4.11	Single molecule labeling and imaging of surface receptors .....	85
4.12	Single molecule internalization assay.....	86
4.13	Single step photobleaching assay.....	86
4.14	TIRF microscopy .....	87
4.15	SPT data analysis.....	88
4.16	Structural MD simulations .....	88
4.17	Statistical Analysis .....	89
APPENDIX AFLUOROLABELLING OF THE PPTASE-RELATED CHEMICAL TAGS: COMPARATIVE STUDY OF DIFFERENT MEMBRANE RECEPTORS AND DIFFERENT FLUOROPHORES IN THE LABELLING REACTIONS		91
A.1	Comparative Qdot- and fluorophore- labelling of different S6-tagged membrane receptors .....	93
A.2	Comparative study of S6-TrkA labelling by different CoA-fluorophore substrates in the PPTase labelling reaction	96
APPENDIX B AN OPTIMIZED PROCEDURE TO SCALE UP SAMPLING IN SMI EXPERIMENTS		100
B.1	Schematic timeline for investigation of TrkA-wt and TrkA-K547N membrane dynamics in response to actin cytoskeleton alterations.....	102
B.2	Schematic timeline for investigation of p75 <sup>NTR</sup> membrane dynamics in response to membrane cholesterol modulation.....	103
BIBLIOGRAPHY		105

# LIST OF ABBREVIATIONS

---

**ACP:** Acyl carrier protein  
**A-loop, AL:** Activation loop  
**APE:** Alanine-Proline-Glutamate  
**AVs:** Autophagosomal vesicles  
**CD:** Cytochalasin D  
**CIPA:** Congenital Insensitivity to Pain and Anhidrosis  
**CNS:** Central Nervous System  
**CoA:** Coenzyme A  
**CRD:** cysteine rich domain  
**CSD:** Cumulative Square Displacement  
**C-tail:** Carboxyl-tail  
**DAG:** Diacylglycerol  
**DFG:** Aspartate-Phenylalanine-Glycine  
**DRG:** Dorsal Root Ganglia  
**ECD:** Extracellular domain  
**EGF:** Epidermal Growth factor  
**EGFR:** Epidermal Growth factor receptor  
**EM-CCD:** Electron-multiplying charge coupled device  
**FGFR:** Fibroblast growth factor receptor  
**FPs:** Fluorescent proteins  
**FRAP:** Fluorescence Recovery After Photobleaching  
**FRET:** Fluorescence Resonance Energy Transfer  
**GAB-1:** GRB2-associated binding protein 1  
**GBR2-SOS:** Growth factor receptor-Bound protein-2- SOS  
**G-loop:** Glycine- rich loop  
**HRD:** Histidine-Arginine-Aspartate  
**HSAN:** Hereditary Sensory and Autonomic Neuropathy  
**ICD:** Intracellular domain  
**Ig:** Immunoglobulin

**IGFR-1:** Insulin-like Growth factor  
**INSR:** Insulin receptor  
**IP:** Immunoprecipitation  
**IP3:** Inositol Triphosphate  
**JK:** Jasplakinolide  
**JM:** Juxta-membrane domain  
**KDR:** Kinase Insert Domain receptor  
**KID:** Kinase insert domain  
**KIT:** Tyrosine protein kinase KIT  
**KM:** Kinase mutant  
**LB:** Latrunculin B  
**LRR:** Leucine rich repetition  
**MAPK:** Mitogen-activated protein kinase  
**MDS:** Molecular Dynamic Simulation  
**MSD:** Mean Square Displacement  
**MSS:** Moment Scaling Spectrum  
**NGF:** Nerve Growth factor  
**NTRK1:** Neurotrophic Receptor Tyrosine Kinase 1  
**NTs:** Neurotrophins  
**PAABD:** Phospho-amino acid binding domain  
**PI3K:** Phosphoinoside 3-kinase  
**PIP2:** Phosphatidylinositol 4,5-bisphosphate  
**PKA:** Protein kinase A  
**PLC- $\gamma$ :** Phospholipase C-  $\gamma$   
**PNS:** Peripheral Nervous System  
**PPTase:** Phosphopantetheinyl transferase  
**PTB:** Phosphotyrosine binding  
**PTMs:** Post Translational Modifications  
**RM:** Recruitment mutant  
**RTKs:** Receptor Tyrosine Kinases  
**SH2:** Src homology-2  
**SHC:** SH<sub>2</sub> containing protein  
**SMI:** Single Molecule Imaging

**SPA:** Scintillation Proximity Assay  
**SPT:** Single Particle Tracking  
**TIRF:** Total Internal Reflection Fluorescence  
**TKD:** Tyrosine Kinase Domain  
**TMD:** Transmembrane domain  
**TNFRs:** Tumor Necrosis Factor receptors  
**TrkA:** Tropomyosin related kinase A  
**Ub:** Ubiquitin  
**VAIK:** Valine-Alanine-Isoleucine-Lysine  
**VEGFR2:** Vascular Endothelial Growth factor receptor type 2  
**WB:** Western blot  
**WNK:** Lysine deficient protein kinase A

# LIST OF PUBLICATIONS

---

- “Fluorolabelling of the PPTase-related chemical tags: comparative study of different membrane receptors and different fluorophores in the labelling reactions”. **Amodeo R\***, Convertino D, Calvello M, Ceccarelli L, Bonsignore F, Ravelli C, Cattaneo A, Martini C, Luin S, Mitola S, Signore G, Marchetti L. Under revision on Frontiers Molecular Biosciences.
- “*Molecular insight on the altered membrane trafficking of tyrosine kinase dead receptors.*” **Amodeo R\***, Nifosi R, Giacomelli C, Ravelli C, La Rosa L, Callegari A, Trincavelli ML, Mitola S, Luin S, Marchetti L. Biochim Biophys Acta Mol Cell Res. 2019. 1867(2):118614.
- “*Fast diffusing p75<sup>NTR</sup> monomers support apoptosis and growth cone collapse by neurotrophin ligands.*” Marchetti L\*, Bonsignore F\*, Gobbo F\*, **Amodeo R**, Calvello M, Jacob A, Signore G, Schirripa Spagnolo C, Porciani D, Mainardi M, Beltram F, Luin S, Cattaneo A. Proc Natl Acad Sci U S A. 2019. 116(43):21563-21572.
- “*Site-Specific Direct Labeling of Neurotrophins and Their Receptors: From Biochemistry to Advanced Imaging Applications.*” Gobbo F\*, Bonsignore F\*, **Amodeo R**, Cattaneo A, Marchetti L. Methods in Molecular Biology. 2018. 1727:295-314.
- “*Probing labelling-induced lysosome alterations in living cells by imaging-derived mean squared displacement analysis.*” D’Urso W\*, D’Autilia F, **Amodeo R**, Marchetti L, Cardarelli F. Biochemical and Biophysical Research Communications (BBRC). 2018. 503(4):2704-2709.

Asterisks are assigned to first authors of publications

# INTRODUCTION

---

Human receptor tyrosine kinases (RTKs) are master regulators of the principal cell functions during embryonic development and adult homeostasis [1]. Their mechanism of action and structural organization are maintained between different species [2], highlighting the importance of a deeper understanding of the role of their catalytic core, the Tyrosine Kinase Domain (TKD). Mutations in the TKD are frequently related to the pathogenesis of cancer, type 2 diabetes, cardiovascular, neurodegenerative and developmental disorders [3]–[6]; for these reasons commonly employed drugs act through the modulation of RTKs activity and/or target specifically their ATP binding site [7], [2], [8]. However, little is known about the specific aberrant mechanisms brought by different mutations of RTKs in these diseases. In particular, while it is established that several hyper-activating oncogenic mutations cause disruption of auto-inhibitory interactions [9], [10] and alterations in membrane disposition, cytoskeletal organization and intracellular trafficking of RTKs leading to prolonged RTKs signaling [11], the role of inactivating mutations looks more heterogeneous. For example, an increased expression of Ryk, ROR and several ephrin (Eph) receptors was found associated with cell motility and metastasis in different cancers, despite the lack of kinase activity of these proteins [12], [13]; on the other hand, other inactivating mutations of RTKs lead to a loss-of-function responsible for neuronal disorders [14]. It appears clear that understanding the role that different mutations have in the onset of diseases represents a big turn on how to treat patients with these specific RTKs alterations [15].

My thesis is focused on the different impact that several mutations inside the TKD have on the structure, membrane distribution, subcellular trafficking and post-translational modifications (PTMs) of one member of the RTK family, the Tropomyosin-related receptor kinase A (TrkA), the high-affinity nerve growth factor receptor, essential in development and survival of selected neuron populations in the nervous system.

More in details, I found that the mutation of lysine 544 (numeration of the human sequence), crucial to allocate ATP and thus to kinase activity, is responsible for the *altered membrane dynamics and distribution of TrkA receptor in absence of Nerve Growth Factor (NGF) stimulation*. Using a single particle tracking (SPT) approach I discovered that this mutation causes a restricted membrane mobility and an increase of cell surface pool, without affecting the membrane oligomerization state of the receptor. Molecular dynamics simulations (MSD) revealed that this mutation is predicted to drive a breakage of a salt bridge between Lys544 in the  $\beta$ 3 sheet and the Glu560 in the  $\alpha$ C helix of the N lobe, responsible for different arrangements of this helix with the C lobe; this conformational change probably leads to new interactions of the mutant with the cortical actin cytoskeleton, causing the increase of TrkA membrane pool and its slow dynamics. On the other side, other mutations for TrkA

catalytic, scaffolding and ubiquitination activities revealed no alterations in membrane dynamics in resting conditions; however, none of these mutants, despite being able to bind the ligand, immobilizes its membrane pool after NGF treatment, thus allowing us to conclude that not only phosphorylation, but also ubiquitination are fundamental for *NGF-dependent membrane immobilization of TrkA* at the plasma membrane.

In parallel, during my thesis I also found that the TrkA-R649W mutation (corresponding to the human R643W residue), positioned in the HRD (Histidine-Arginine-Aspartate) domain of the catalytic loop and responsible for the onset of *Hereditary Sensory and Autonomic Neuropathy type IV (HSAN IV) disease*, is characterized by an altered membrane distribution of receptors in both neuroblastoma and Dorsal Root Ganglia (DRG) neurons in an actin-dependent manner. Furthermore, despite its absence of kinase activity, TrkA-R649W is rapidly internalized in response to ligand stimulation and probably not recycled as its wt counterpart. Finally, the increased number of autophagosomal vesicles (AVs) found in neuroblastoma cells overexpressing the mutant, can candidate the alteration of the autophagic flux as a possible molecular effect characterizing the neuropathy.

My thesis is organized in four chapters plus two appendixes; in *Chapter 1* I introduce the structural organization, mechanisms of action and auto-inhibition of RTKs and of a subclass of kinase receptors, able to signal also with an impaired kinase activity. The second part of the chapter is focused on the structure, dynamics, activation and PTMs of TrkA receptor. Finally, in the third part I describe biochemical and biophysical methods adopted to evaluate the RTKs activation, giving particular importance to the state of the art of advanced imaging techniques studies applied to RTKs.

*Chapter 2* deals about the evaluation of membrane dynamics and PTMs in response to different mutations inside the TKD of TrkA receptor. First, I described the membrane dynamics and exposition of a dead-kinase mutant, TrkA-K544N, analyzing possible causes for its changes in membrane dynamics also exploiting the results of computational analysis, using Molecular Dynamic Simulation (MDS). I then tested the interactions of cytoskeleton with TrkA-K544N, analyzing its changes in dynamics and membrane exposition in response to pharmacological treatments. Finally, I moved on with the evaluation of the dynamics, membrane exposition and PTMs of mutants for TrkA kinase, recruitment and ubiquitination activity.

In *Chapter 3* I collect the characterization of the membrane distribution, intracellular trafficking, signaling and protein turn-over of the TrkA-R649W, a kinase inactive mutant found associated with HSAN IV congenital neuropathy. I evaluated changes in dynamics of TrkA-R649W in response to cytoskeleton alterations, such as the internalization of this receptor in response to NGF treatment. Finally, I also measured the number of AVs shown by cell overexpressing this mutant in resting condition, to evaluate possible involvement of the disease with dysfunction of autophagic flux.

In *Chapter 4* I describe into details the methods and materials used for biochemical experiments, the methods adopted to perform MDS, the microscopy set-up used for our imaging experiments and the relative adopted data analysis.

Finally, in *Appendix A* I report a methodological work that allowed me to optimize the phosphopantetheinyl transferases labelling method used to fluorolabel molecules for single molecule imaging. In details, I compared the labelled cell fraction for two types of labelling strategies on TrkA and VEGFR2 receptors, belonging to the RTKs family and P75<sup>NTR</sup>, member of the Tumor Necrosis Factor receptor (TNFR). I also evaluated the physico-chemical properties of different fluorophores used in this labelling reactions and their suitability for high-end microscopy techniques such as Total Internal Reflection Fluorescence (TIRF) microscopy, with particular respect to signal-to-background ratio and fluorophore aspecific adhesion to or internalization in cells.

*Appendix B* presents a methodological scheme of an experimental timeline that I used during the preparation of samples to be imaged at the TIRF microscope during my thesis work. This allowed me to maximize the number of samples that can be collected in one-day-work, so as to ensure an optimal sampling and reproducibility in Single Molecule Imaging (SMI) experiments.

# 1. TRKA AS A PARADIGM OF HUMAN TYROSINE KINASE RECEPTORS

---

## 1.1 TYROSINE KINASE RECEPTORS

Human tyrosine kinase receptors constitute a large family of 58 single-pass transmembrane proteins, divided in 20 subfamilies, which through their intrinsic enzymatic activities are able to catalyze the phosphorylation of tyrosine residues of target proteins using ATP as a phosphate donor. RTKs are known to be fundamental components of cellular signal transduction, regulating the main cellular functions as survival, proliferation, differentiation, cell-cell communications and metabolism [1]. Moreover their structural organization, mechanism of action and interaction with specific intracellular effectors are highly conserved from *Caenorhabditis Elegans* to humans [2], highlighting the importance of understanding the biological role of each conserved protein domain of the TKD [2]. It is now well known that RTKs transduce signals coming from the extracellular environment to the interior of the cell, starting kinase-dependent signaling cascades leading to different and specific cellular responses. However, the first fundamental contribution to the RTKs knowledge dates back to the 1950 when Rita Levi Montalcini and Stanley Cohen discovered the first soluble growth factor, called Nerve Growth Factor, for its ability to induce neurites outgrowth when administered to cells [16]. Only few years later Cohen discovered another growth factor, the Epidermal Growth Factor (EGF), but the mechanisms underlying the cellular outputs induced by these molecules remained unknown until 1978, when he demonstrated the existence of the first RTK named EGF receptor (EGFR). EGFR was discovered as a membrane protein that resulted to increase its phosphorylation status after the binding with EGF [17]. The current concept of RTKs occurred around the 80s with the discovery of kinases and phosphatases roles, which are enzymes able to reversibly phosphorylate and de-phosphorylate proteins, respectively, modifying their functions thereby regulating their activities [17], [18]. Just for the important role played by these enzymes in regulating different cellular responses, aberrations in the activation of RTKs leads to the onset of a wide range of diseases including cancer, type 2 diabetes, cardiovascular and neurodegenerative diseases [19]. About these, the most famous example is probably the EGFR, that was the first RTK discovered to be linked to human cancer [20], leading the way to the development of drugs with important roles in cancer therapy through the modulation of RTKs activity [2], [8].

### 1.1.1 Structural architecture of RTKs

The structural architecture of RTKs is maintained among the members of this family and reflects their functional organization composed by three main domains (Fig. 1.1):

- i) the *extracellular domain* (ECD) is the portion exposed to the external side of the plasma membrane, responsible for ligand binding. The ECD represents the most variable portion among the RTKs, generally divided in different sub-domains like immunoglobulin (Ig-) like domains, cysteine-rich domains, fibronectin type III-domains or EGF-like domains [21].
- ii) The *transmembrane domain* (TMD) is the single-pass  $\alpha$ -helix that connects the ECD with the intracellular domain of the receptor, contributing to the stability of dimers and sometimes playing also an active role in signaling [22].
- iii) The *intracellular domain* (ICD) has a structural organization conserved among the RTKs, composed by the juxta-membrane region (JM), the catalytic TKD and the carboxy (C-) terminal. The TKD as well as the JM and C-term regions typically contain Tyr residues that are auto-phosphorylated upon ligand binding to the receptor [21].

In the absence of stimulation, the majority of RTKs exists as a single polypeptide chain organized in a monomeric form, and the ligand binding induces dimerization and receptor activation [23]. However Met, INSR-1 and insulin receptors are exceptions: Met receptor is a heterodimer composed by an extracellular short  $\alpha$ -chain connected by a disulfide bond to a membrane spanning  $\beta$ -chain, while insulin receptor and IGFR-1 are expressed at plasma membrane already in form of disulfide linked- $(\alpha\beta)_2$  heterodimers (Fig. 1.1) [1], [24]. Furthermore, there are several studies reporting also that EGF molecules activates EGFR through binding to pre-existing oligomers, and also that Tie2 and Eph receptors require the formation of larger oligomers for their activation [25]–[28]. In any case, ligand binding is always necessary for RTKs activation.

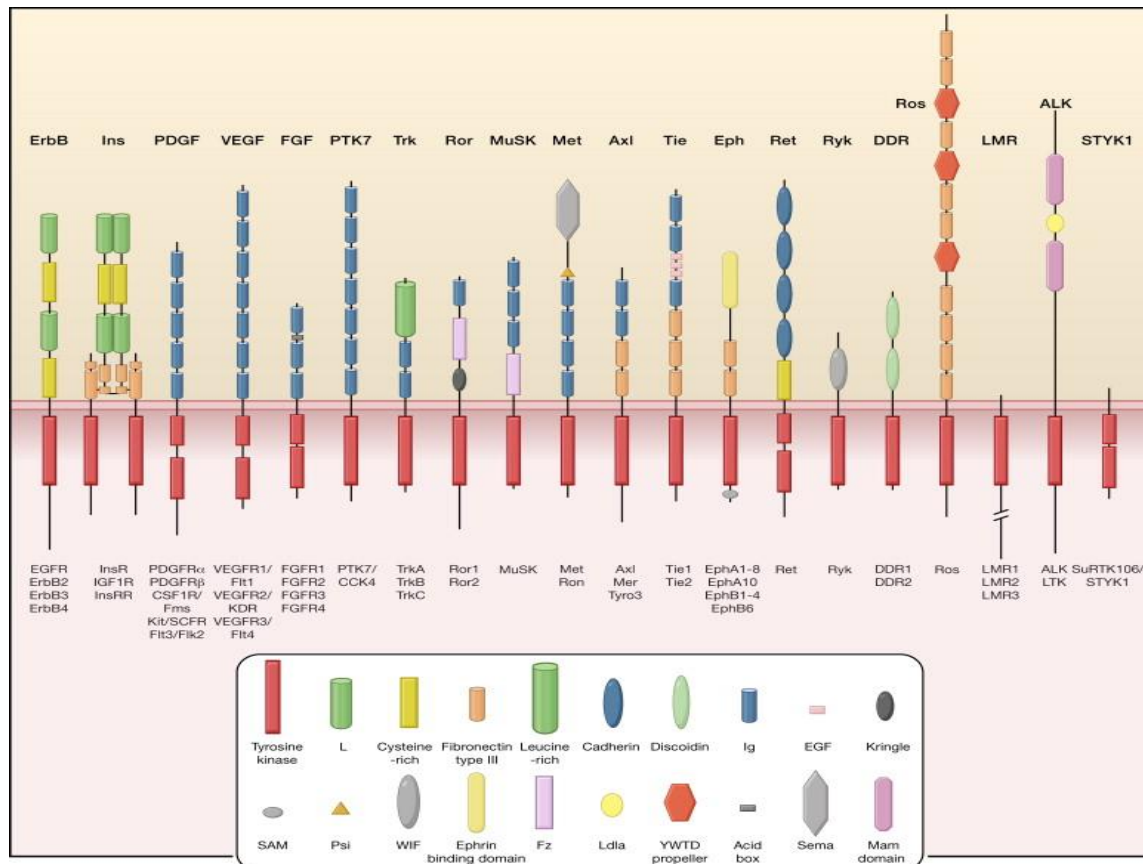


**Figure 1.1.** Schematic representation of the 20 subfamilies of human tyrosine kinase receptors; different ECD (legend in box on the bottom of the figure) are identified by structure determination or sequence analysis, ICD are shown as red rectangles. L: leucine, Ig: immunoglobulin, SAM: sterile alpha motif, PSI: plexin-semaphorin-integrin, WIF: Wnt inhibitory factor, FZ: Frizzled domain, LDLA: low-density lipoprotein receptor class A, YWTD: Tyr-Trp-Thr-Asp, SEMA: structural domain of semaphoring, Mam: mephrin/A5-protein/PTP mu. Taken from [2].

### 1.1.2 The Tyrosine kinase domain

The TKD is an amino-acid domain approximately 300-500 aa long, responsible for the catalysis of the transfer of the  $\gamma$ -phosphate from ATP to the hydroxy groups of Tyr residues on the target protein. From a structural point of view, the TKD is organized in two lobes, the N-terminal small lobe (N-lobe) and the C-terminal large lobe (C-lobe), connected by the kinase insert domain (KID) characterized by a variable length, spanning from few to up to 100 amino acid (Fig. 1.2) [29]. The N-lobe, structured in antiparallel  $\beta$ -sheets and one single  $\alpha$ -helix denoted as  $\alpha$ C helix, has the important role of binding and stabilizing the ATP complexed with  $Mg^{2+}$  ions [30]. The C lobe is mainly composed by  $\alpha$ -helices and loops [31], and enhances the chelation of  $Mg^{2+}$  ions with ATP, binds the intracellular protein to be phosphorylated and finally transfers a phosphate group from ATP to the Tyr residues [21]. Between the N-lobe and the C-lobe resides the substrate cleft, where ATP, divalent cations, and peptide

substrate are bound. More in details, the TKD is characterized by the following defined and conserved structural motifs (Fig. 1.2):

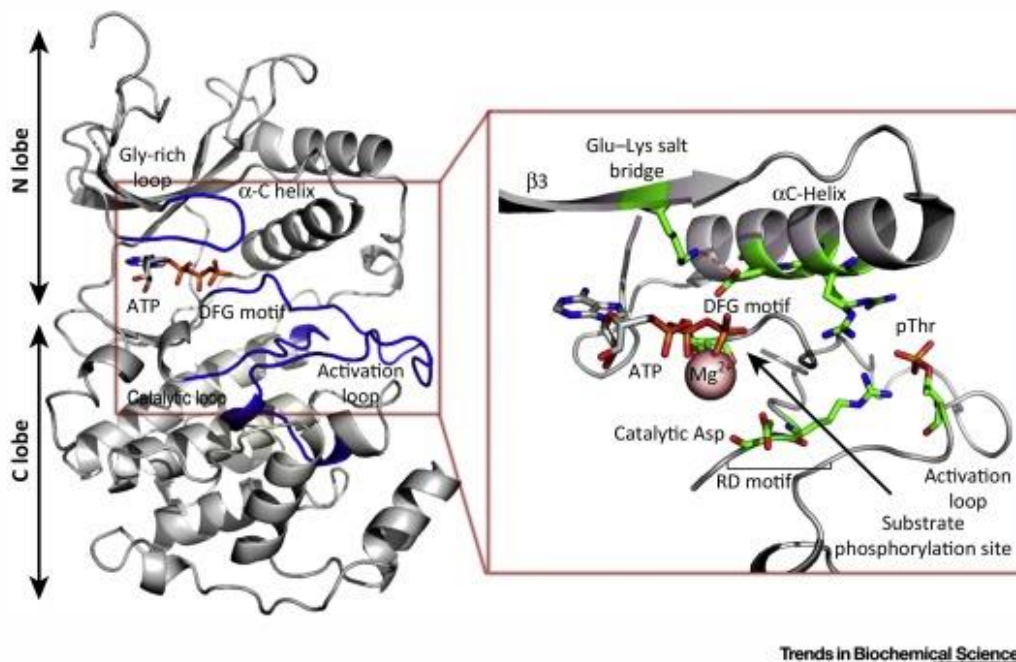


**Figure 1.2.** Representation of functional elements in the TKD of the active p38/ (PDB 3PY3). The active site, which is zoomed, is located between the N-lobe and the C-lobe, with the ATP-binding domain positioned in the cleft between these two lobes. During the receptor activation, the phosphorylation of residues in the Activation loop (A-loop) promotes the interaction with an Arg located in the catalytic loop and with the N-terminal residues of the  $\alpha$ C helix, inducing the alignment of the DFG motif and Glu-Lys salt bridge. Image taken from [32].

**i)  $\alpha$ C-helix** positioned in the N-lobe, containing a glutamate, whose residue is fundamental for ATP binding and catalytic activity, because it is involved, in the active configuration of protein kinases, in the formation of a conserved salt bridge with a residue of lysine (Lys) positioned in the  $\beta$ 3 sheet [31]. This Lys is also involved in the interaction with the  $\alpha$ - and  $\beta$ -phosphates of the bound Mg-ATP, necessary for its positioning for the phosphotransfer. In inactive kinases, this specific C-helix can assume non-canonical conformations [33] and mutations at the  $\beta$ 3 Lys are typically related to ‘kinase dead’ variants of canonical kinases [34].

**ii) Glycine-rich loop** (G-loop or P-loop), containing the consensus sequence GxGxxG between strands  $\beta$ 1 and  $\beta$ 2 and associating closely with the phosphate groups of bound ATP through backbone interactions [34].

**iii) Activation loop** (A-loop, AL), a region with high flexibility characterized by different phosphorylation sites that lead to efficient receptor catalytic activity [35]. Its specific phosphorylation and orientation regulates the switch between inactive and active configuration of TKD and is responsible of substrate binding [30]. This motif is usually 20-30 amino acids long [36] and is limited by the DFG motif at the N-term and the APE (Ala-Pro-Glu) motif at the C-term.

**iv) DFG motif** present in the first part of the A-loop, and composed by aspartate-phenylalanine-glycine triplet; it has an important role in the binding of the phosphates of ATP. The Asp residue critically coordinates divalent cations within the A-loop, and is one of the most important, conserved residues in TKD [34].

**v) Catalytic loop**, a conserved motif positioned between  $\beta 6$  and  $\beta 7$  sheets, containing the **HRD domain** formed by a sequence of histidine-arginine-aspartate residues; the aspartate residue therein ( $\beta 7$  Asp) is thought to function as a catalytic base and/or to correctly orient the hydroxyl group of the Tyr to be phosphorylated [32], [34].

**vi) APE motif** is a conserved alanine-proline-glutamate motif involved in the anchoring of the A-loop with the kinase domain core and in substrate binding.

Generally, after receptor-activation-driven protein phosphorylation, the AL interacts with the positive residues of the  $\alpha C$ -helix and of the catalytic loop. This process induces conformational changes of the DFG motif and of the  $\alpha C$ -helix; in particular the rotation of the  $\alpha C$ -helix promotes the formation of the Glu-Lys salt bridge and the start of catalytic activity (Fig. 1.3) [32].

Previous studies made on the active and inactive IRK and Protein Kinase A (PKA) structures obtained from crystal X-ray studies revealed the existence of an open conformation referred to as the inactive receptor configuration, and a close one as the active counterpart (Fig. 1.3) [37] (Hubbard, 1997; Hubbard et al., 1994). It was reported that one of the mechanisms regulating the switch between active and inactive forms of RTKs depends on the specific orientation of the  $\alpha C$  helix towards the C-lobe and in particular the A-loop [36]. A specific auto-inhibitory conformation between the  $\alpha C$  helix and the A-loop ensures the receptor inactivation in absence of stimulation; on the contrary, ligand binding induces a conformational switch that allows the ATP allocation in its binding site and the beginning of the catalysis.

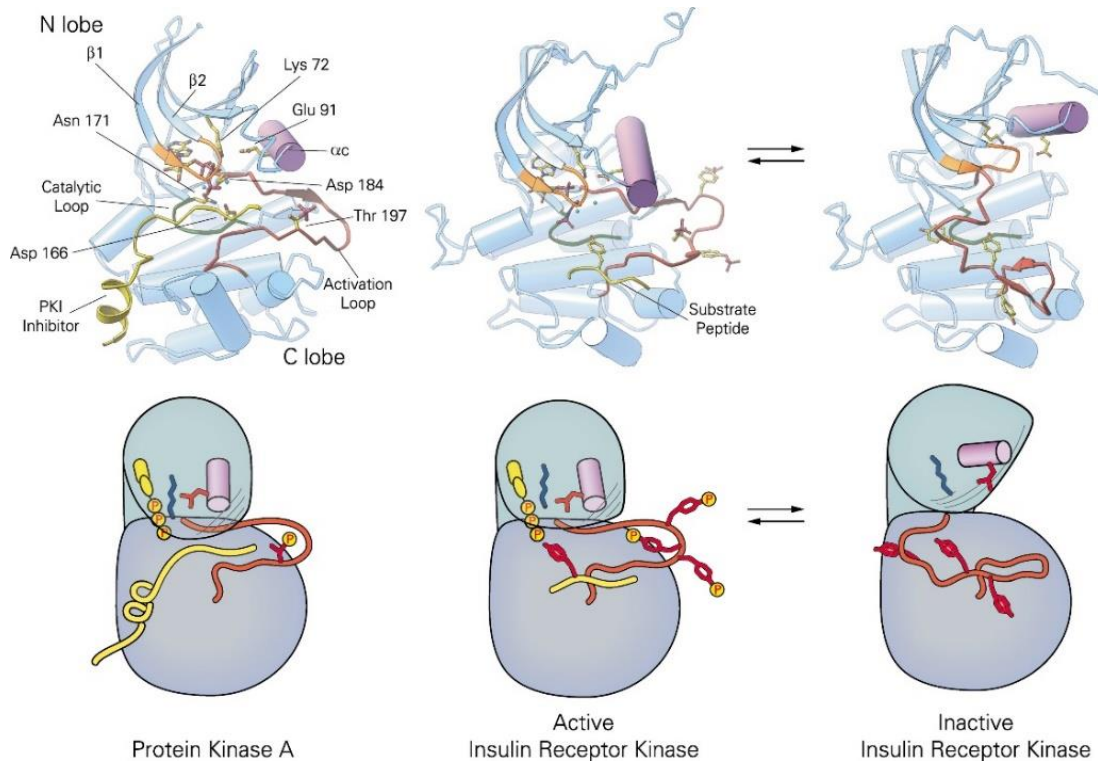


**Figure 1.3.** Upper panel: ribbon representation of the crystal structure of PKA and IRK. Here the functional structures and residues of TKD are highlighted: A-loop: red,  $\alpha$ C-helix: purple, P loop: orange, catalytic loop: green, a Protein Kinase inhibitor (PKI), in yellow. On the right, the switch between inactive and active IRK: in inactive state the conformation of the A-loop blocks the binding of nucleotides. Below: Representation of conformational changes of TKD in response to RTKs activation with particular emphasis on the disposition of the  $\alpha$ C-helix (purple cylinder) and A-loop (in orange); the blue segment represents the catalytic Lys of the salt bridge. Image taken from [37].

### 1.1.3 Mechanisms of activation and autoinhibition of RTKs

Generally activation of RTKs occurs after ligand binding at the ECD of the protein, leading to receptor homodimerization and subsequent juxtaposition of cytoplasmic TKDs of each monomer [2]. In most cases this juxtaposition enhances auto-phosphorylation in *trans* of Tyr located in the A-loop or in the JM region, releasing the cis-autoinhibition configuration and inducing the conformational changes necessary to stabilize the active state of the kinase [2], [38]. The phosphorylation cascade events promote the phosphorylation of Tyr residues that recruit down-stream signaling proteins, typically through Src homology-2 (SH2) or phosphotyrosine-binding (PTB) domains, which specifically bind phosphotyrosines thanks to their specific sequence contexts (Fig. 1.4) [21], [39].

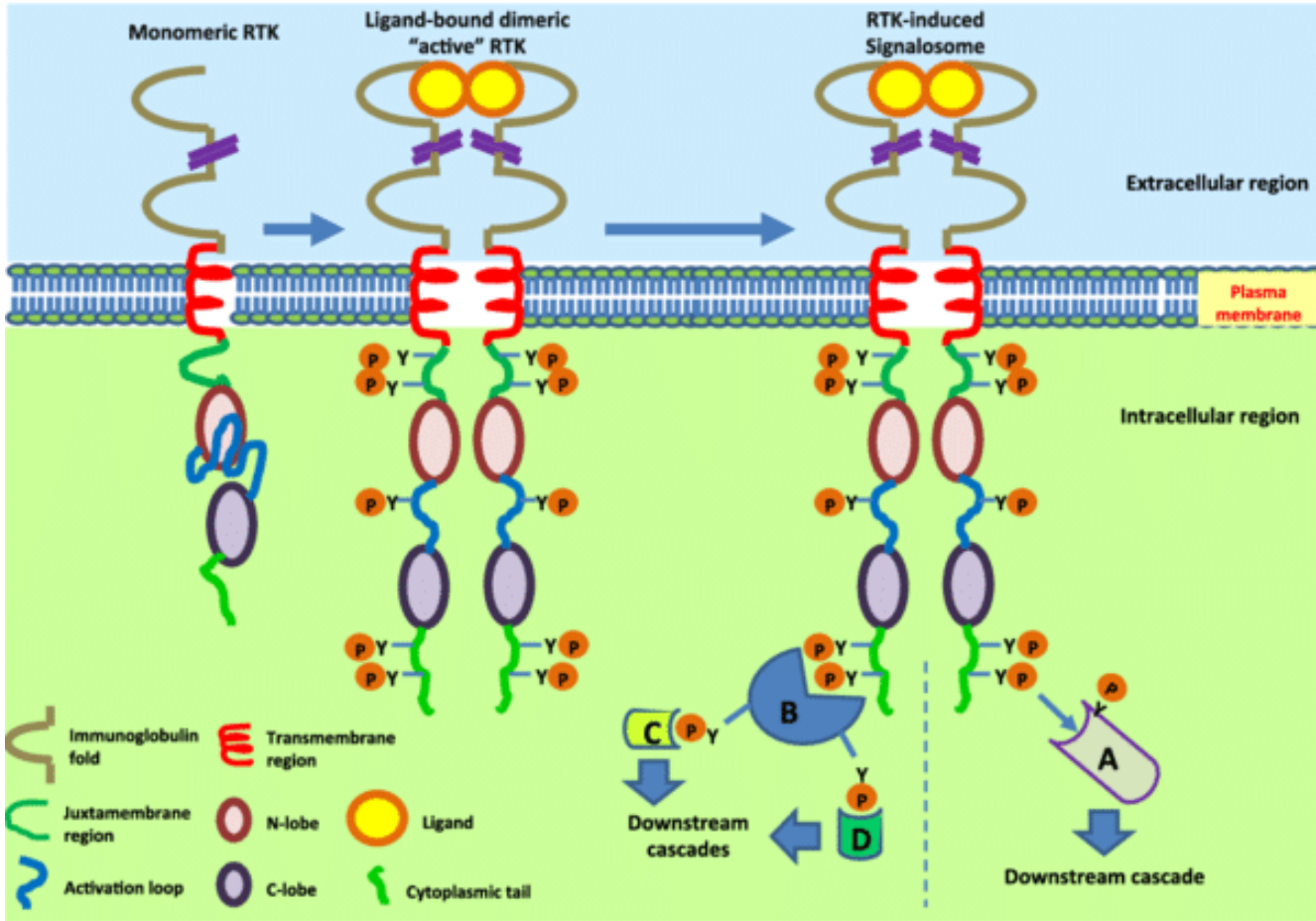


**Figure 1.4. Mechanism of RTKs activation after ligand binding.** RTKs reside at plasma membrane mainly as monomers; after ligand binding RTK dimerization promotes the juxtaposition of the ICD of the two monomers necessary for the trans-phosphorylation of Tyr (Y) (phosphate groups are indicated with orange circles) in the A-loop; this process induces the trans-phosphorylation of Tyr positioned in the kinase insert, JM and C-tail regions, that serves as a docking site for adaptor proteins (B) or phosphorylate signaling molecules (A) responsible of the recruitment of intracellular effectors. Image taken from [40].

However, the dimerization process can occur with different mechanisms (Fig. 1.5):

- i) ligand-mediated dimerization: crystal structure analysis on the ECD of several RTKs demonstrated that the binding of a bivalent ligand with two monomers of receptors induces the formation of a dimeric complex as observed for TrkA [41], Flt1, vascular endothelial growth factor (VEGFR) receptor [42], Tie2 [25] and Ephrin receptors [26], without direct contact between the extracellular regions of the two receptors (Fig. 1.5 A).
- ii) Ligand-mediated and receptor-mediated dimerization: in other cases, as for KIT receptor, its ligand (stem cell factor, SCF) binds only one monomer of receptor at the first three or five Ig-like domains of the ECD [43], and this is sufficient to induce the cross-linking of two receptor molecules. Indeed, this event promotes a reorientation of D4-D5 domains closest to the plasma membrane, that enhances the interaction across interfaces of KIT dimer, necessary for receptor activation [44] (Fig. 1.5 B).

iii) For Fibroblast growth factor receptor, FGFR, the activation requires not only the binding of a bivalent ligand, but also the involvement of an accessory molecules, as heparin [45] (Fig. 1.5 C).

iv) Receptor-mediated dimerization: for EGFR, the activation is completely receptor-mediated, without any physical interaction between two activating ligands; here the bivalent ligand binds only a single monomer of EGFR, promoting substantial conformational changes in its ECD, which becomes able to unlock the mechanism of receptor auto-inhibition [46] (Fig. 1.5 D).

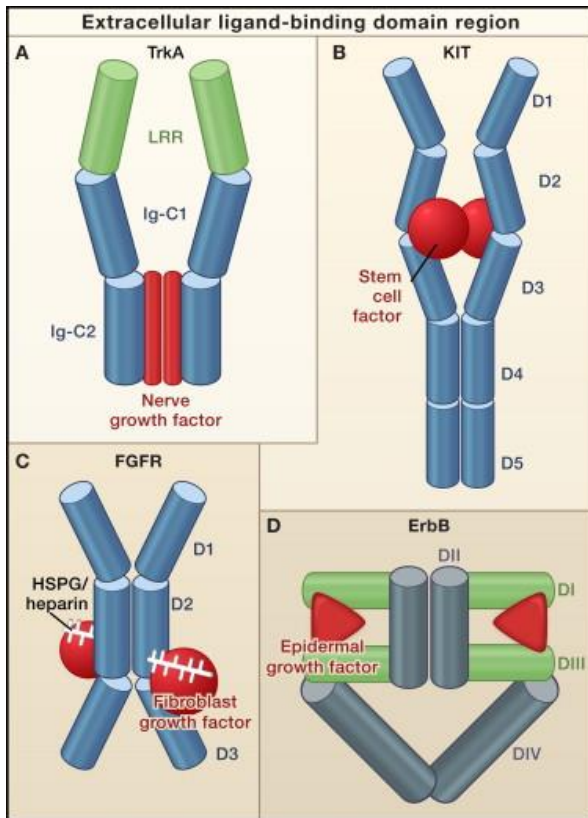


**Figure 1.5. Different dimerization process of RTKs.** **A)** A NGF dimer (red) crosslinks two TrkA molecules without direct contact between the two receptors. **B)** A SCF dimer (red) crosslinks two KIT molecules and two Ig-like domains (D4 and D5), reoriented upon receptor activation, interact across the dimer interface. **C)** Two FGFR molecules come into contact through the Ig-like domain D2, where it binds also the heparin or heparin sulfate proteoglycans; in addition, each FGF molecule (red) contacts Ig-like domains D2 and D3 in both FGFR molecules. **D)** Dimerization of EGFR receptors is completely mediated by the receptor. Through its binding simultaneously to two sites (DI and DIII) within the same receptor molecule, the ligand drives conformational changes in the receptor, which expose a previously occluded dimerization site in domain II, which allows the dimerization with the other receptor molecule. Image adapted from [2].

Despite the great improvements in knowledge of RTKs gained during the last years, the mechanisms by which changes in the ECD following ligand-binding could be responsible of conformational rearrangements in the ICD, leading to receptor activation, represent a field still widely debated.

The general mechanism of activation is shared among different members of RTKs family and depends on the specific modification of key regulatory elements located inside the TKD (see Paragraph 1.1.2), necessary for the phosphotransfer of a  $\gamma$ -phosphate from ATP onto the hydroxyl group of a Tyr residue, necessary for the receptor catalysis [2], [36]. In most cases the auto-phosphorylation process occurs in trans and the sites are phosphorylated with a specific order; the first phase of auto-phosphorylation is necessary for the enhancement of the catalytic activity after receptor activation, while during the second phase occurs the phosphorylation of Tyr residues that recruit downstream intracellular effectors. Recently it was discovered also a third phase of activation, consisting in trans-phosphorylation events that maximize the ability of kinase to phosphorylate its targets. Although the activation process is conserved among RTKs, they display an array of different mechanisms of cis-auto-inhibition, necessary to avoid aberrant

receptor activation in absence of stimuli; in these cases the TKD is maintained in an inactive or auto-inhibited conformation until it is activated by extracellular ligand-induced oligomerization [23], [38]. It was reported that a lot of TKD activating cancer-related mutations cause the disruption of these auto-inhibitory mechanisms and, at least for KIT and EGFR, lead to receptor hyper-activation [2], [47]. This makes clear that understanding the regulation of RTKs auto-inhibitory system represents an important field in cancer-research. Several intramolecular interactions are involved in the maintenance of the cis-autoinhibition mechanisms (Fig. 1.6):

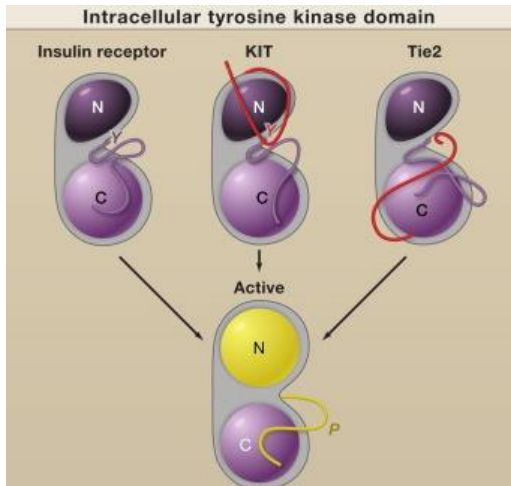


**Figure 1.6. Schematic representation of autoinhibition mechanisms of RTK.** The C-lobe is in light purple, the N-lobe in dark purple in inactive state or yellow in active states and the A-loop in purple or yellow in the inactive and active states, respectively. *Insulin receptor-like*: the A-loop interacts directly with the active site and blocks access to ATP and protein substrates. Phosphorylation of Tyr residues disrupts these autoinhibitory interactions and allows the kinase to switch to the active state. *KIT receptor-like*: the JM region (red) interacts with elements within the active site (including the  $\alpha$ C helix and the A-loop) to stabilize an inactive conformation. Phosphorylation of key Tyr in the JM region destabilizes these interactions and allows the TKD to assume an active conformation. *Tie-2 receptor like*: the C-term tail (red) interacts with the active site of the TKD to stabilize an inactive conformation. Image adapted from [2].

- i) A-loop inhibition: Insulin receptor is characterized by a cis-auto-inhibition mechanism regulated by the A-loop; a specific relocation of the Tyr Y1162 inside the TKD stabilizes the configuration of A-loop that blocks the active site. Only after ligand binding, the Y1162 residue is trans-phosphorylated, allowing the switch to the active state, while the  $\alpha$ -helix in the N-lobe changes its orientation, enhancing ATP binding [37]. In the case of FGFR, different Tyr residues, located inside the A-loop, are involved in the auto-inhibitory mechanism though specific interactions that cis-auto-inhibit the TKD, interfering with the protein-substrate binding but not with the ATP-binding [48]. Also in this case, the auto-inhibition mechanism is released after receptor dimerization, thanks to the reorientation of the A-loop and the  $\alpha$ C-helix.
- ii) JM inhibition: MuSK, Flt3, Eph family and KIT receptors auto-inhibition is managed at JM level [49]–[51]. Tyr residues located in the JM region interact with the A-loop in the TKD, ensuring the maintaining of an auto-inhibited conformation. The trans-phosphorylation of Tyr following receptors dimerization destroys the cis-auto-inhibition mechanism, promoting receptor activation.
- iii) C-terminal tail inhibition: Tie-2 activation is regulated by a cis-auto-inhibition mechanism occurring at the C-terminal tail. Here, Tyr residues acting as auto-phosphorylation sites block the access of the

substrate at the active site [52]; the phosphorylation of residues in the C-tail promotes the receptor activation.

For some RTKs, as Trk receptors, the mechanism of auto-inhibition is still not accepted, considering that it seems to be different also between TrkA and TrkB, despite they share 88% identity in the TKD [53]. The work of Miranda et al. has suggested the existence of an exclusive auto-inhibition mechanism for TrkA receptor. They demonstrated that after introduction of activating mutations in conserved residues, TrkA showed different responses with respect to both Met and Kit receptors [54].

### 1.1.4 The family of pseudokinases

Pseudokinases are a subfamily of RTKs characterized by the lack of amino acids that are fundamental for allocating the ATP and metal ions necessary to start the catalysis [34]. Despite their impairment or absence of kinase activity, some pseudokinases have a role as signal transducers both in physiological and in pathological conditions [55]–[57]. The mechanism underpinning this alternative activation is still debated, but two different hypothesis are accepted: pseudokinases could have a residual kinase activity sufficient to catalyze the phosphotransfer, or alternatively they can work as scaffolding proteins for downstream signalling, participating in the formation of multi-protein complexes [58], [59]. Manning et al. investigated human RTKs using a combination of EST (Expressed Sequence Tag) and cDNA data, Genewise homology modeling and Genscan ab initio gene prediction: they confirmed that five are characterized by inactive ICD (ErbB3, PTK7/CCK4, EphB6, EphA10 and SuRTK106), and showed that other three (Ror1, Ror2 and Ryk) result to be inactive, despite being previously predicted to be active [56]. One of the most studied examples of pseudokinases is HER3, a member of the EGFR family, which, despite being inactive, is able to stimulate the autophosphorylation and activation of HER2 receptor in response to neuregulin [60], [61]. Furthermore, in the ephrin family EphB6 and EphA10 are predicted to be pseudokinases: in particular EphB6, although its lack of kinase activity, is able to enhance the activation of another kinase protein, ZAP-70, after ephrin binding [62].

The most common mutations displayed by pseudokinases are located in different key conserved motifs of the TKD [34] (Fig. 1.7):

- i) Glycine-rich loop (see Paragraph 1.1.2): mutations at the first two glycine residues is reported to alter the ATP binding site; these mutations are found in PTK7/CCK4, Ror1, Ror2, Ryk and SuRTK106.
- ii) VAIK (Val-Ala-Ile-Lys) motif: in the active conformation of RTKs there is a conserved salt bridge between a Lys positioned in  $\beta$ 3 strand and a Glu residue in  $\alpha$ C helix; the Lys coordinates also the  $\alpha$ - and  $\beta$ - phosphates of the bound  $Mg^{2+}$ -ATP to allow the correct phosphotransfer. Mutations in  $\beta$ 3 Lys are reported for ErbB3, EphB6, EphA10 and SuRTK106.

- iii) HRD motif (see Paragraph 1.1.2): the Asp residue, responsible for the correct orientation of the hydroxyl group of the residue to be phosphorylated, is substituted with an Asn in the HRD of HER3, while it is replaced with serine or glycine respectively in the case of Ephb6 and EphA10.
- iv)  $\beta$ 7-Asn: this is a fundamental residue for the correct orientation of the HRD domain, and is mutated to Ser and His in EphB6 and EphA10, respectively.
- v) DRG motif (see Paragraph 1.1.2): the aspartate of this motif, that has the important role to coordinate divalent cations, is lost in PTK7/CCK4, EphB6, EphA10 and SuRTK 106 receptors.

There are also some cases in which the lack of some of these domains saves the catalytic activity of the protein, as for WNK proteins: 4 isoforms of WNK lack the lysine residue of the VAIK domain but despite this they are found catalytically active thanks to the presence of another Lys residue that substitutes the missing one [58], [63].

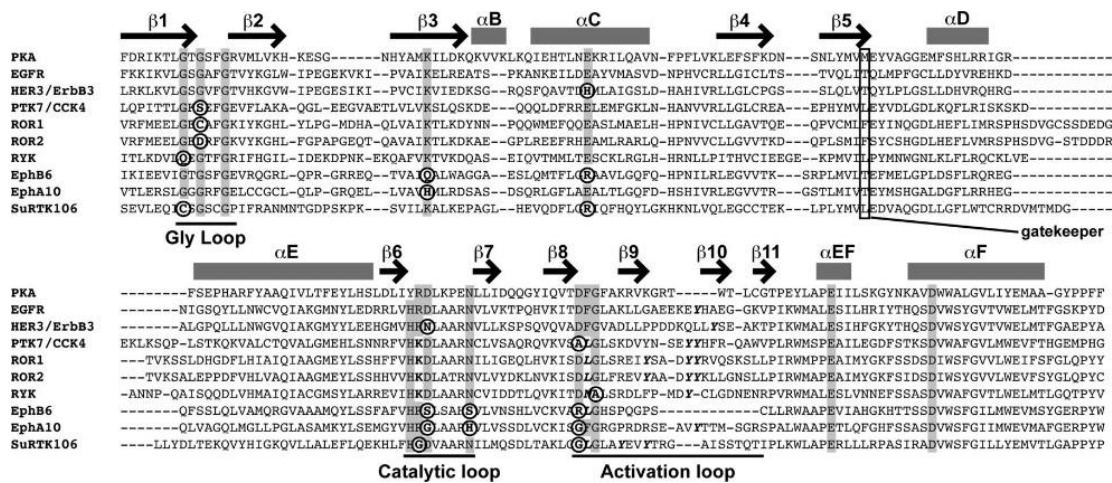


**Figure 1.7.** Alignment of sequence of the TKD of 8 pseudokinases below the sequence of PKA, used as reference for active RTKs. Secondary elements are reported on the sequence alignment, conserved residues are shaded in gray and mutated residues in pseudokinases are circled in black. Image taken from [34].

## 1.2 TRKA RECEPTOR AND THE NEUROTROPHIN SIGNALING NETWORK

In 1950 Rita Levi-Montalcini discovered that transplanting a mouse sarcoma into a chicken embryo promoted the secretion into the blood of a factor, lately named NGF, responsible for the sensory and sympathetic nerve growth [64]. This observation opened the way to the complex and charming world of neurotrophins (NTs). Years of research have allowed us to know that these growth factors are master regulators of neuronal development, survival and plasticity in the nervous system (Fig 1.8) [65]–[68]. In mammals, the NTs family is composed by four members: NGF, brain-derived neurotrophic factor (BDNF), neurotrophin-3 (NT-3), and neurotrophin-4 (NT-4). NTs exert their action mainly through the binding to two classes of receptors exposed at the neuronal cell surface:

the Trk family and the P75<sup>NTR</sup> receptors. More into details P75<sup>NTR</sup>, belonging to the tumor necrosis factor family, can be recognized and activated by all components of the neurotrophin family [69]. On the contrary, NTs display a precise binding specificity for the three components of the Trk family, leading to different cellular outputs: TrkA binds with high affinity to NGF and with low one to NT-3, and regulates survival, cell growth and differentiation at PNS level; TrkB binds BDNF, NT-3 and NT-4 and regulates survival, plasticity and apoptosis at CNS and finally the NT-3 binding to TrkC is responsible for survival and growth of sensory neurons.

My thesis is focused on the TrkA receptor, one of the most important player in development, survival, differentiation and neuronal plasticity of the mammalian PNS [70, 71] and of the cholinergic system in the CNS [72]. TrkA protein is widely expressed on the cell surface of sympathetic, trigeminal and dorsal root ganglia and in cholinergic neurons of the basal forebrain and striatum [73], [74], where it exerts its functions through the binding to the NGF produced by target tissues. A correct level of NGF is indeed fundamental for the maintenance of the homeostasis of the nervous system: increased NGF-mediated activity or alteration of signaling by NGF/TrkA complexes can be associated to inflammatory and neuropathic pain disorders [75] and to neurodegeneration [76], [77]. Approaches such as NGF gene and protein therapies, or administration of small molecules acting as TrkA agonists, are actually on trial for the treatment of neurodegenerative disorders such as Alzheimer's disease; on the contrary the administration of drugs that inhibit the action of NGF/TrkA complexes are on trial for the treatment of pain disease. Only one of these approaches, however, is currently FDA approved [78].

However, despite TrkA receptor is mainly known as the high affinity receptor for NGF [71], it was firstly discovered in 1982 as an oncogene expressed in colon cancer [79]. In the last years, both TrkA and NGF have been found expressed in several malignant tumors. Indeed the activation of ERK, SRC and AKT pathways, all mediated by TrkA, regulates tumor cell proliferation and spreading in breast cancer [80]; an analogue involvement of TrkA-related pathways are also found in gastric [81] and pancreatic cancers [82]. Despite this, the potential role of TrkA mutations in promoting tumorigenesis and cancer has not yet been established [83]. TrkA receptor, as TrkB and TrkC, are lately considered important therapeutic targets in cancer treatment; accordingly, several clinical trials based on TrkA kinase activity inhibitors are currently in development [83].

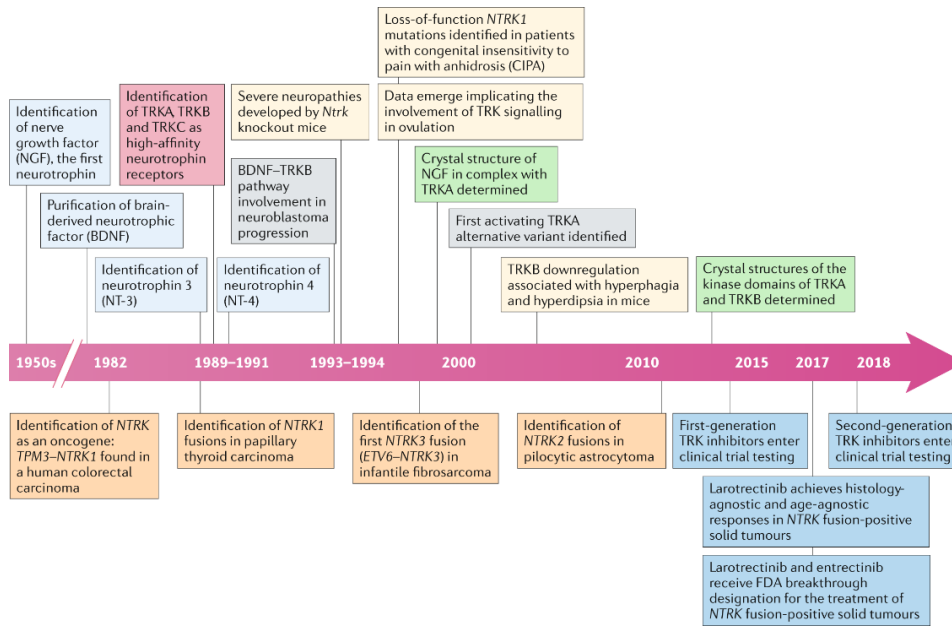


**Figure 1.8.** Timeline of the discoveries related to the biology and therapeutic targeting of Trk signaling. Boxes above the timeline arrows represent the milestone discoveries relevant to normal Trk pathway biology, while boxes below are NTRK (Neurotrophic Tropomyosin-Related- or Tyrosine Receptor- Kinase) fusions found in cancer. NTRK are the genes encoding for human Trk proteins (NTRK1, 2, 3 for TrkA, B, C, respectively). Image taken by [83].

### 1.2.1 TrkA structure and signaling

In human, the gene encoding for the TrkA protein is Neurotrophic Tyrosine Kinase receptor 1, *nrk1*, located on the chromosome 1 q21-q22 [84]. The length of the gene is 23 Kb, divided into 17 exons and 16 introns; the gene presents an high homology of sequence with the *Rattus Norvegicus* and *Mus Musculus* species (86% identity in the entire protein sequence, 94.6 % identity in the TKD; see also Table 1.1). Three isoforms of TrkA protein have been identified [85]: isoform I is the most abundant form, expressed mostly in non-neuronal tissues, consisting in 790 aa and activated by both NGF and NT-3; isoform II is expressed in neuronal tissues, composed by 796 aa and activated only by NGF and finally isoform III, resulting from the splicing of exons 6, 7 and 9, is mainly present in pluripotent neuronal stem and neuronal crest progenitors and constitutively active in a ligand independent manner [86]. As aforementioned, TrkA isoform II generates a protein of 796 amino acid, with a weight of 87497 Da. The mature protein goes from amino acid 33 to amino acid 796 because the first 32 amino acid constitute the signal peptide (SP), necessary for the correct translocation of the protein in the ER; here the SP is cleaved, the protein is N-glycosylated and finally translocated at the plasma membrane. This glycosylation process can produce two alternative forms of TrkA with molecular weight of 110 KDa and 140 KDa [87]; only the latter is finally translocated at plasma membrane.

<b>Human TrkA isoform I sequence numbering</b>	<b>Rat TrkA sequence numbering</b>	<b>Mouse TrkA sequence numbering</b>
<b>K544</b>	K547	K547
<b>Y496</b>	Y499	Y499
<b>Y676</b>	Y679	Y679
<b>Y680</b>	Y683	Y683
<b>Y681</b>	Y684	Y684
<b>Y757</b>	Y760	Y760
<b>Y791</b>	Y794	Y794
<b>R643</b>	R649	R649

**Table 1.1. List of corresponding TrkA residues mentioned in the human, rat and mouse sequences.** For our studies we used mainly constructs of the rat TrkA sequence. However, some of the experiments and the molecular dynamics simulations used the human TrkA sequence. When needed, we shall use *hTrkA* to specify the human sequence. The two sequences (rat and human) share a very high homology.

As the majority of RTKs, TrkA receptor is organized in ECD, TMD and ICD.

The ECD constitutes the N-term of the protein, has a length of 391 amino acid and is organized in two IgL-like domains, IgL-1 and IgL-2, two CRD (CRD1 and CRD2); between CRDs there is a repetition of three 24 residues leucine-rich motifs (LRR 1-3). TrkA receptor interacts with its ligands mainly through the IgL-2 domain, but other regions are also reported to be involved in NGF binding: Arevalo et al. demonstrated that the mutation of a Cys residue in the IgL-1 domain is able to abolish NGF binding [88].

The TMD is composed by a single hydrophobic transmembrane  $\alpha$ -helix composed by 16 residues that structurally connects the ECD with the ICD of the receptor; this region plays important roles in receptor internalization and recycling [89] and in the dynamic equilibrium between pre-formed inactive dimers and NGF-induced dimer form [90].

TrkA ICD, composed by 357 aa residues, is divided like the other RTKs into JM, TKD and C-tail, with precise functional roles explained in the following; in particular this region contains 11 Tyr residues, six of which can be phosphorylated [91].

The JM region plays important roles in neurite outgrowth and differentiation [92]. Here, the Y496 residue ensures the activation of phosphoinoside-3-kinase (PI3K) signaling pathway, which starts with the conversion of Phosphatidylinositol 4,5-bisphosphate (PIP2) in Phosphatidylinositol 4,5-triphosphate (PIP3) at membrane level, and ended with the activation of Akt. Y496 is fundamental also to amplify the signaling pathway mediated by

Shc-binding proteins: when Shc binds the phosphorylated Y496 residue with its PTB domain, its SH2 domain is free to interact with other intracellular effectors, leading to signaling amplification. More into details, when phosphorylated, the Y496 residue can bind the adaptor proteins GAB1 (*GRB2-Associated Binding Protein-1*) and SHC (*SH2 Containing Protein*), enhancing their association with GBR2-SOS (*Growth Factor Receptor-Bound Protein-2-SOS*), responsible of the GDP-GTP switch on Ras protein. The activated Ras binds Raf, which phosphorylates and activates MEK (MAP/ERK kinase), inducing the activation of MAPKs-ERK1/2 (*Mitogen-Activated Proteins-Extracellular signal-regulated Kinase*), with the final effect of activating transcription factors CREB and c-Fos, responsible of neurite growth regulation.

The structural organization of TrkA TKD resumes the same previously reported for all RTKs (see Paragraph 1.1.2), where the presence of conserved motifs ensures ATP binding, catalytic function and substrate recognition. There are three Tyr in the A-loop that are fundamental for the phospho-transfer reaction; these residues are always phosphorylated in the same order: Y680, Y676, Y681; the same was reported for IGF-1 receptor, where the corresponding Tyr involved are Y1162, Y1158 and Y1163 [93]. The Y757 residue is also an important regulatory element involved in neuronal survival, neurite outgrowth and differentiation, through the activation of PI3K pathway.

Finally, the C-term tail is characterized by the presence of Tyr Y791, fundamental for neurite outgrowth and differentiation. Phosphorylated Y791 is the binding site for PLC- $\gamma$ ; PLC- $\gamma$  signaling starts from the conversion of PIP2 to diacylglycerol (DAG) and inositol triphosphate (IP3), promoting the release of Ca<sup>2+</sup>. The C-tail also contains the PPXY motif, where a proline residue (P791 in rat sequence corresponding to P788 in human sequence) is located, fundamental for TrkA ubiquitination mediated by the ubiquitin ligases E3 Nedd 4-2 [94].

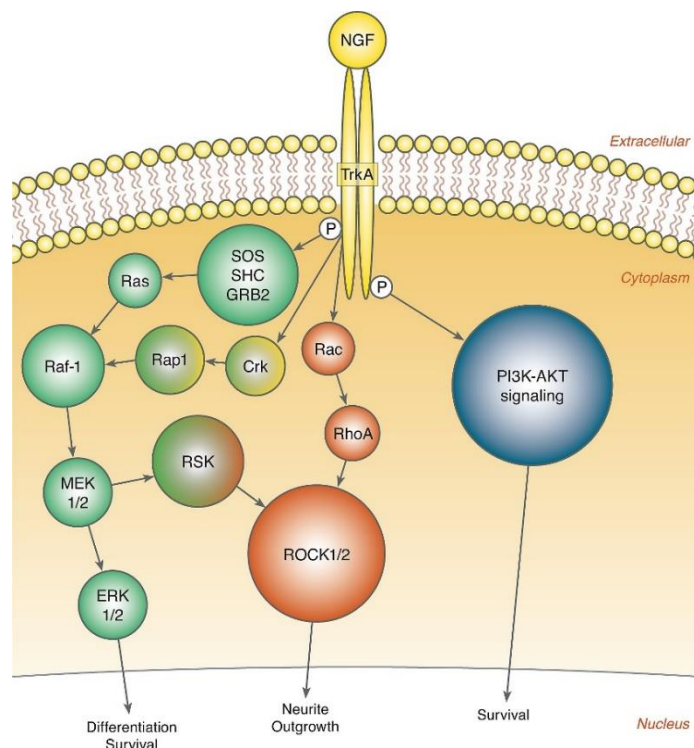


**Figure 1.9. Signal-transduction pathways induced by the binding of NGF to TrkA receptor.** After NGF-binding, the ICD leads to TrkA auto-phosphorylation and activation of signaling cascades. Proteins that interact directly with the ICD are SHC, SOS, SH2B and IAPs, some of which are shown here. Ligand binding can also trigger the RAS signaling pathway, leading to survival and differentiation, and an alternative survival-signaling pathway through PI3K. Image taken from [95].

## 1.2.2 TrkA mechanism of activation

The mechanism of activation of TrkA receptor is poorly understood with respect to other components of RTKs family [96]. As mentioned in paragraph 1.2.3, the study of the crystal structure of TrkA complexed with NGF [41] corroborated, during last years, the theory that TrkA activation is ligand mediated, with NGF promoting TrkA dimerization and trans-phosphorylation in the TKD [70], [97]. Lately several works demonstrated that TrkA, expressed in different cell lines and in absence of ligand stimulation, was present as pre-formed inactive dimers in equilibrium with the monomeric population [98], [99]. This equilibrium between different oligomeric states can be explained by the rotational model of Maruyama, who proposed the existence of a mechanism of conformational switch between inactive and active TrkA dimeric states, occurring at TM and JM domains [91]; moreover the same mechanism was found also in EGFR/HER, VEGFRs and FGFRs [96], [100]. It was recently discovered the existence of two different motifs,  $L_{424}XXF_{427}A_{428}XXF_{431}$  and  $S_{419}XXXG_{423}$ , located on two opposite sites of TrkA TMD and probably responsible for the co-existence of active and inactive dimers (Fig 1.10), [90]. This work reported that in case of receptor overexpression and in absence of ligand, TrkA can be organized in

pre-formed inactive dimers thanks to the  $L_{424}XXF_{427}A_{428}XXF_{431}$  motif. Instead, administration of NGF has the effect to stabilize the active dimer conformation, allowing kinase domain activation [90]. More into details, NGF binding places the JM region in a specific configuration that promotes the rotation of the transmembrane helix from one to the other interface of the TMD [90]. In this way NGF binding induces the release of the auto-inhibition mechanism occurring at the ICD, ensuring the correct allocation of ATP, the cis-auto phosphorylation of Tyr residues of the A-loop and the trans-phosphorylation of additional Tyr residues acting as docking sites for intracellular adapter proteins, as PLC- $\gamma$  and Shc.

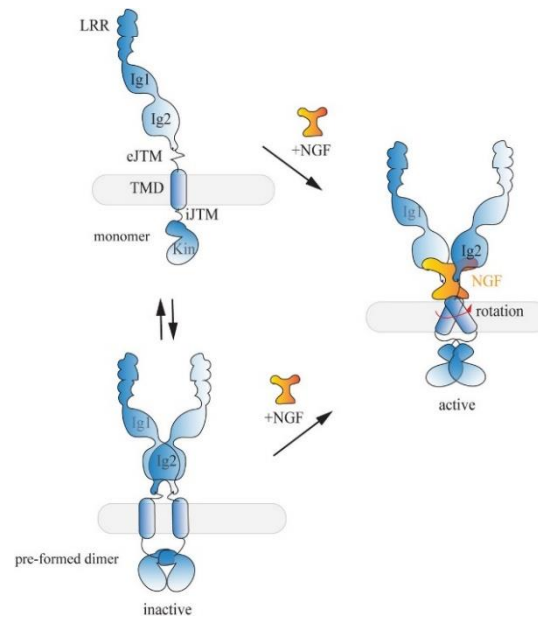


**Figure 1.10. Model proposed for TrkA activation.** In absence of NGF, TrkA is present at the plasma membrane in equilibrium between inactive monomer (upper panel) and pre-formed inactive dimer (lower panel). In both cases the dimeric ligand NGF binds TrkA induces the rotation of the TMD of the dimer enhancing the releasing of the auto-inhibition mechanisms and the receptor activation. Image taken from [90].

### 1.2.3 TrkA trafficking

The membrane and subcellular trafficking of TrkA receptor is pivotal for the activation of the canonical RTKs signaling pathways, responsible for the neuronal growth and survival (Fig. 1.11). Following NGF binding and activation of PI3K, Ras/ERK and PLC- $\gamma$  signaling pathways, NGF/TrkA complexes are internalized via clathrin coated pits [101], [102] or with a Pincher mediated endocytosis pathway [103] that generates multivesicular bodies (MVBs) containing multiple vesicles with complexes of NGF-TrkA. It was reported that the membrane pool of TrkA receptors starts to decrease after 5 minutes of NGF stimulation, while only after 15 minutes the receptor reached the maximum level of its phosphorylation [104]. NGF/TrkA complexes are internalized in early endosomes with different destinations [105]: receptors can be in recycling endosomes to be recycled to the cell

surface, sorted into late endosomes to be degraded in lysosomes [106]–[108], or transported retrogradely or anterogradely towards the soma or the neurite tip in signaling or recycling endosomes, respectively [101], [104], [109], [110]. Retrograde transport was a mechanism discovered by Campenot, who demonstrated for the first time that NGF administered at the axon tip of neurons is sufficient for the survival of neuronal cell bodies [111]. The theory of the signaling endosomes (Fig. 1.11, lower panel) claims that vesicles of TrkA-NGF are transported by dynein motor proteins retrogradely towards the soma, in complexes with signaling effectors as PI3K, MAPK and PLC- $\gamma$ . When at the cell body, the signaling endosomes enhance the activation of CREB, promoting neuronal survival. However, also another model of signal transduction between axon tip and cell body was proposed, named “wave propagation model”: here the binding of NGF to TrkA generates a cascades of phosphorylation events that move retrogradely within the plasma membrane. MacInnis et al. demonstrated that after treatments at sympathetic axon tips with NGF-coupled beads which prevents NGF-TrkA complexes internalization, the survival signal at the cell body persisted, suggesting that the phosphorylated receptors alone are able to transduce the survival signaling [112]. On the other hand, TrkA anterograde trafficking was reported to be necessary for the signaling of receptors: once produced at the cell body, most Trk receptors are indeed carried towards the axonal tip, where after their exposure at plasma membrane, they are bound and activated by NTs [113].

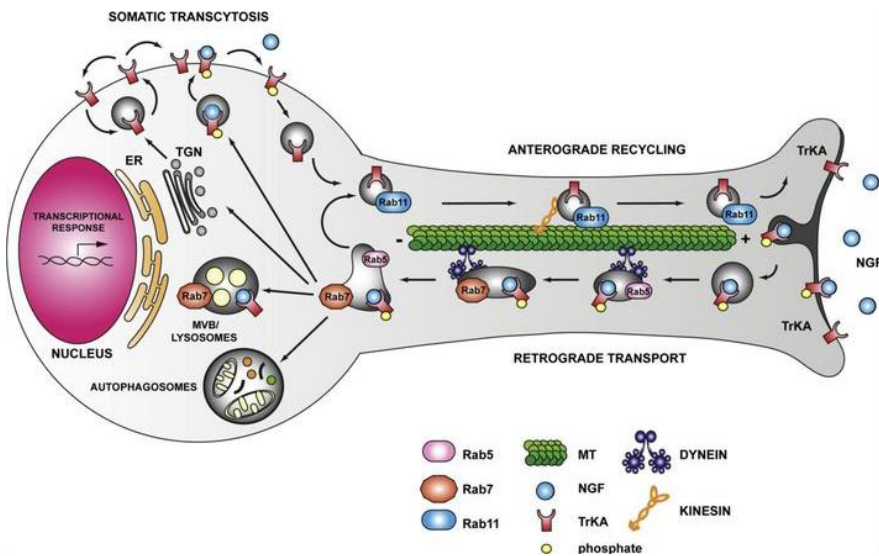


**Figure 1.11. RTK membrane trafficking in neuronal axons.** Schematic representation of signaling endosomes of TrkA and NGF; after NGF binding the activated TrkA receptors can be internalized at the axon tip and retrogradely transported to the cell soma via dynein-motor complexes in signaling endosomes (in gray). When at the cell soma, signaling endosomes are sorted and the receptors can enter a pathway of degradation, recycling to the plasma membrane, transcytosis or autophagic pathway. Image taken from [115].

## 1.2.4 TrkA ubiquitination

Ubiquitination is a post-translational modification consisting in the attachment of a 76 amino acid long polypeptide, called ubiquitin (Ub), to the target protein. Historically, the ubiquitination process was related to misfolded proteins destined to proteasomal degradation [116], but in the last years several works demonstrated an alternative role for ubiquitination in protein sorting and signaling [117], [118].

The ubiquitination process occurs through three sequential enzymatic steps: the first ATP-dependent step comprises the activation of Ub by an E1 Ub-activating enzyme. Then the activated Ub molecule is transferred to the cysteinyl group of the E2 Ub-conjugating enzyme, which forms a complex with the E3 Ub-ligase, and the last finally transfers the ubiquitin to Lys (K) residues of the target protein. The E3 family are divided in two different groups, one consisting of a homologous to the HECT domain and the other containing *RING* or RING-like domain [119]. Different types of ubiquitination correspond to a different final destiny for the target protein [120]: mono-ubiquitination occurs when one Ub molecule is attached to the protein of interest, targeting it to endocytic pathway and membrane trafficking. Multi-monoubiquitination, which consists into the attachment of several Ub molecules to different Lys residues of the target protein, causes endocytosis of receptor. Finally, in the poly-ubiquitination process, one or more ubiquitin-chains are attached to the protein, determining its endocytosis and proteasomal degradation. More into details, the most frequent Lys-48 poly-ubiquitination chains is related to the degradation mediated by the 26S proteasome, while Lys-63 chains is usually associated to non-proteolytic degradation, as in the case of HectH9, Mdm2, tumor necrosis factor receptor-associated factor 6 (TRAF6), cellular inhibitor of apoptosis protein 1/2 (c-IAP1/2) and ring finger protein 8 (RNF8) [121]–[123].

Ubiquitination of TrkA receptor has an important role in regulating its degradation, trafficking and function, instead deregulations of the ubiquitination machinery are usually related to cancer [124], [125]. It was reported that TrkA is ubiquitinated by four different E3 ubiquitin ligases, namely TRAF-6 E3 RING Ub-ligase [126], Nedd 4-2 E3 HECT Ub-ligase [94], [127], TRAF-4 E3 RING Ub-ligase [128], and Cbl [129]. TRAF-6 poly-ubiquitinates TrkA at the lysine K485, located in the JM region [126], [130]; it interacts with p75<sup>NTR</sup>, promoting K63-linked poly-ubiquitination, which regulates the internalization and signaling of TrkA [126], suggesting an important involvement of P75<sup>NTR</sup> in TrkA ubiquitination. The involvement of P75<sup>NTR</sup> in the TrkA subcellular trafficking is today controversial; Kuruvilla *et al.* demonstrated that TrkA receptor is able to internalize after NGF stimulation without the presence of P75<sup>NTR</sup> [131]. Another work reported that P75<sup>NTR</sup> regulates negatively the ubiquitination of TrkA

receptors, causing a delay of its internalization in PC12 cells and protecting it from degradation [132]. Furthermore, the study of Gheeta et al. reported that TRAF6, after binding with P75<sup>NTR</sup>, needs the adaptor protein p62 to poly-ubiquitinate TrkA receptors, enhancing its shuttling towards the proteasome [133]. The Cbl ubiquitin ligases (c-Cbl and Cbl-b) were instead reported to be negative regulators for TrkA, involved in ligand dependent ubiquitination of the receptor and targeting it to lysosomes for degradation [134],[129]. Nedd 4-2 is the unique Ub-ligase that binds TrkA but not TrkB and TrkC receptors, because it recognizes a PPXY motif present only in the TrkA sequence. Nedd 4-2 is responsible for the NGF dependent multi-mono-ubiquitination of TrkA [94], [135], responsible for degradation and NGF-mediated signaling [127]. The first evidence of the specificity of Nedd 4-2 for TrkA receptors happened with the discovery that overexpression of Nedd 4-2 induced neuronal apoptosis only in NGF-dependent DRG neurons, but not in BDNF-dependent DRG neurons [94]. Arevalo *et al.* demonstrated the importance of this specific motif, by generating a mouse model with a mutation in the first Pro residue of the PPXY sequence (*hTrkA-P782S*). After NGF stimulation, the mouse model with TrkA-P782S showed impaired ubiquitination and defects in both trafficking and degradation [127]. Moreover TrkA-P782S models showed an increased number of sensory neurons, and also increased TrkA signaling [127]. The same mouse model was used also to demonstrate that the lack of ubiquitination was related to an enhanced thermal sensitivity and inflammatory pain [136]. Finally, TRAF4 promotes TrkA ubiquitination through Lys-27 and Lys-29 ubiquitin linkages, leading to the hyper-activation of kinase activity and inducing the alteration of its phosphorylation status [128].

### 1.2.5 The involvement of TrkA receptor in HSAN IV disease

Pain is a protective mechanism adopted by multicellular organisms to prevent the contact with noxious stimuli [137]. Few years ago it was discovered that alterations of the signaling mediated by NGF/TrkA complexes were responsible for a deficit of sensory neurons specialized to detect pain sensation [138]. It was already known that the NGF pathway ensured the survival of both sympathetic ganglion neurons and nociceptive sensory neurons in DRG, and of ascending neurons in the basal forebrain [71], [139]. Indeed, initially it was proposed that the absence of NGF during the fetal period was the only cause for the loss of growth fibers, finally responsible for the insensibility to feel pain. However, the real turning point was the discovery that mice without nociceptive DRG neurons had lost the orthologous gene of human TrkA, promoting TrkA as a candidate for the onset of the Hereditary Sensory and Autonomic Neuropathies (HSANs) type IV (OMIM# 256800). Subsequently, genetic analysis in four patients affected by HSAN IV confirmed mutations in the coding gene for TrkA [140]. Currently, it is well known that the TrkA pathway is fundamental for innervating skin with sensory axons and for the survival of pain receptors [141]; indeed, HSAN IV (also called CIPA, Congenital Insensitivity to Pain and Anhidrosis) is

caused by the lack of nociceptive and sympathetic nerves and characterized by loss of feeling especially in hands and feet. In particular, HSAN IV is a rare genetic disorder inherited in an autosomal recessive manner, which usually affects female and male children in equal number. It is characterized by insensitivity to feel pain, due to the absence of afferent neurons essential for the detection of noxious and thermal stimuli in multicellular organism [137], and by anhidrosis, caused by the altered innervation of eccrine sweat gland. Because of the loss of thermal and noxious sensitivity, children affected by this disease have usually unintentional self-mutilation, repeated fractures, and joint damages; furthermore, the inability to sweat (anhidrosis) causes recurrent episodes of fever, usually related to hyperpyrexia conditions. It was reported that patients affected by HSAN IV have usually developmental delays and learning disabilities. From a molecular point of view, HSAN IV disease is characterized by more than 105 [142] mutations inserted in the TrkA coding sequence: in most cases patients show nonsense and missense mutations and less frequently small insertions or deletions [143]. The comparison among missense mutations associated with HSAN IV showed that all are closer to the TKD and thus fundamental for the protein kinase activity [54], [144]. The group of Mardy et al. identified nine frameshift, seven nonsense, seven splice and 14 missense mutations in HSAN IV families coming from different countries; they found in one Ecuadorian and three Japanese families three mutations inside the region coding for TrkA ICD: R548fs, G571R and IVS15+3A-C [139]. 11 HSAN IV mutations were identified in families with different ethnic groups (Fig. 1.12): six missense mutations (Arg85Ser, Leu231Pro, His598Tyr, Gly607Val, Arg643Trp, Gly708Ser), two frameshift (Asn67fs, Gln308fs), one nonsense mutation (Gln9X) and finally two variants of splicing (IVS4-1G-C, IVS7+1G-A). From the comparison among 100 normal chromosomes only Leu231Pro, Arg643Trp, Gly708Ser resulted really exclusive and so responsible for HSAN IV disease. In particular, Arg643Trp and Gly704Ser, which play a fundamental role in enzymatic activity, are located in the TKD and conserved among different RTKs [87]; His598Tyr placed in the ICD is instead conserved in all members of the Trk family. Arg85Ser (in the Leu-rich domain) and Gly607Val (in the ICD) are not conserved. However, the frameshift mutations, Asn67fs and Gln308fs, which are located in the ECD, generate truncated forms of the TrkA protein.

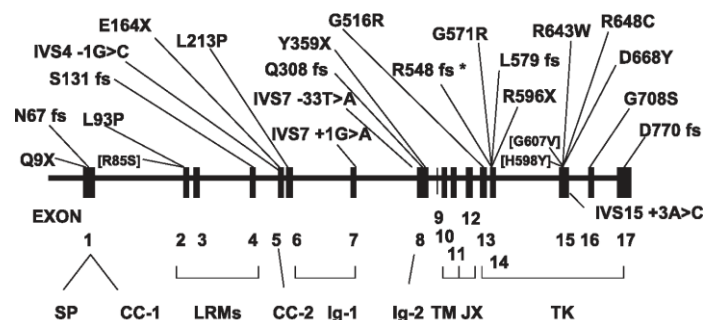


**Figure 1.12.** Location of mutations in the human TrkA sequence associated to CIPA. The human TrkA gene is divided into 17 exons and 16 introns. The entire sequence was estimate to span at least 23 kb, coding for a protein of 790 or 796 aa. The asterisk denotes the common Japanese founder mutation (R548fs); three mutations in brackets are probably polymorphisms in a particular ethnic background. Image taken by [14].

More recently, the group of Shaikh have characterized the membrane expression, glycosylation, auto-phosphorylation, Y496 phosphorylation, PLC- $\gamma$  and neurite outgrowth of seven novel missense mutations found in patients affected by HSAN IV [143]. From the results, the mutation p.G517E showed similar glycosylation, membrane localization, auto-phosphorylation and Y496 phosphorylation of TrkA-wt, while the PLC- $\gamma$  signaling and the neurite outgrowth are impaired. This mutation (p.G517E) does not impair kinase activity, highlighting that the evaluation of Y496 phosphorylation was not sufficient to assess the pathogenicity of HSAN mutations. On the other hand, p.G522E mutation, generating a glycosylated and membrane-translocated receptor, is not phosphorylated upon NGF stimulation, causing an impairment of the PLC- $\gamma$  pathway and of neurite outgrowth. All the mutations p.L657P, p.I699T and p.R771C display less glycosylation and reduced membrane expression of the 140 kDa protein than the TrkA-wt. Furthermore, structural modeling demonstrated that these mutations, located in TKD, cause a rearrangement of the 3-dimensional protein structure, probably responsible for the abolishment of kinase activity [143]. Finally, p.C763S shows reduced auto-phosphorylation and Y496 phosphorylation, while C752S is considered a polymorphism because no defects in glycosylation, membrane expression, phosphorylation or neurite outgrowth are found. With an exome sequencing study, Altassan *et al.* discovered three missense and two non-sense novel HSAN IV mutations [144]: in particular p.Arg110Asp and p.Ser142Ter localized in the ECD, p.Lys476Ser in the JMD while p.Arg643Gln and p.Leu694Pro located in the TKD of the protein [144]. With a computational approach they analyzed the predicted effect that some of these mutations had on the TrkA structure; in particular they found that p.Arg110Asp induces the loss of two hydrogen bonds, while p.Leu694Pro and Arg643Gln only loose one, causing possible structural rearrangements that can compromise the protein function. In particular, in the case of Arg643Gln mutation (which is the human residue corresponding to the R649 we analyze in Chapter 3, see table 1.1), the substitution of an Arg with a Gln causes the loss of the positive charge and alters the local stability of the protein, because of the small size of the substituted residue [144]; the consequent lack of the hydrogen bond in this position disturbs the TKD, abolishing its function [144].

The group of Franco *et al.* has instead characterized the subcellular localization, kinetics of degradation, misfolding and cellular toxicity in primary neurons of three novel mutations found in children affected by HSAN IV disease: L213P and C300stop positioned in the ECD and  $\Delta$ 736 in the TKD of TrkA receptor [146]. They found that C300stop is rapidly disposed to autophagy,  $\Delta$ 736 is probably degraded by the proteasome system while L213P is a long-lived protein with a poor trend to protein degradation [146]. In particular, the latter mutation induces misfolding, retention in ER and delayed degradation, together with a marked increase of the number of autophagosomal vesicles, responsible for the induction of swollen regions in neurons and sensitization of PC12nr5 cells to cell death.

### 1.3 VEGFR2 RECEPTOR STRUCTURE AND MECHANISM OF ACTIVATION

Vascular endothelial growth factor receptor (VEGFR) type 2 is a member of the VEGFR family, which, through the binding to VEGF-A, -C and-D, plays pivotal roles in blood vessels formation and angiogenesis in both physiological and pathological conditions.

The crystal structure of the TKD of VEGFR2 shows high homology of sequence and conformation with FGFR-1 and Insulin receptor [147]. VEGFR2 has an ECD composed by 750 residues, organized in seven Immunoglobulin-like domains. At the level of the fifth Ig-L domain, there is a disulfide bridge responsible for the connection between the N-term of the protein and the rest of the receptor. The ECD is connected with a single 20 aa TM  $\alpha$ -helix with the ICD, organized in JM region, TKD and C-terminal tail [148]. In detail, the TKD is divided in two subdomains, the proximal and the distal kinase domain, separated by a KID sequence of 70 aa residues. The distal kinase domain contains the catalytic loop with the aspartic acid residue (Asp 1028) necessary for phosphotransfer reaction and the A-loop, containing tyrosine residues directly involved in the receptor kinase activity.

The VEGFR-2 activation requires a correct re-orientation of receptor monomers, after the ligand binding, to phosphorylate Tyr residues involved in the activation of the angiogenic pathway [149]; these events cause also rearrangements in the TM domain and interactions between IgL domains 4 and 7 in the ECD of the receptor [150]–[152].

Also in this case, phosphorylation of specific Tyr residues starts the catalytic activity responsible for the activation of proliferation, migration and survival of cells pathways:

- i) Y1054 and Y1059 are two fundamental residues located in the AL, which, when phosphorylated, stabilize the AL and enhance ATP and substrate binding, increasing in this way the catalytic activity of the receptor.
- ii) Y951 is one of the residues involved in the migration process, fundamental for the step of blood vessels formation, positioned in KID. Y951 binds TSA<sub>d</sub>, an intracellular effector that regulates cell migration and actin re-organization [153]. After ligand binding, Src leads to the phosphorylation of Y1175, which induces the activation of the Tyr in focal adhesion kinase (FAK), responsible of spreading and migration of the endothelial cells.

- iii) Y1175 and Y1214 are other important residues positioned in the C-term. In particular Y1175 is involved in the binding of PLC- $\gamma$ , regulating cell proliferation; after PLC- $\gamma$  binding there is an increase of intracellular Ca<sup>2+</sup> and the production of DAG, which stimulates protein kinase A (PKA), promoting the activation of mitogen-activated protein kinases (MAPK) [154].

## 1.4 EXPERIMENTAL STRATEGIES TO DETECT RTKS KINASE ACTIVITY: FROM BIOCHEMICAL TO ADVANCED IMAGING APPROACHES

Taking together the information provided above, it is clear that the mechanisms of activation have differentiated and reached a big grade of complexity among the different RTKs. Understanding each single activation mode is crucially important, in order to achieve specific and efficient therapeutic activation or inhibition of their activity. To this purpose, several biochemical and biophysical approaches have been developed during these years to detect and monitor protein kinase activity. Their main features are reported in Table 1.2.

Technique	Advantages	Disadvantages	Ref
<p><b>Radioactive scintillation</b> Exploits the transfer of radiolabeled (<math>\gamma</math>-<sup>32</sup>P) phosphate from ATP to target peptide/protein in order to visualize and quantify phosphorylation events</p>	<ul style="list-style-type: none"> <li>No need of pTyr antibodies</li> <li>Reduced interference of light-absorbing compounds because the detection is performed at one emission <math>\lambda</math></li> <li>Sensitivity</li> </ul>	<ul style="list-style-type: none"> <li>Radioactive reagents are expensive</li> <li>Risk of danger due to the exposition to radioactive reagents</li> <li>short half-life of <sup>32</sup>P-labeled ATP</li> </ul>	[155]
<p><b>FRET based methods</b> (Fig. 1.13)</p>	<ul style="list-style-type: none"> <li>Kinase activity can be tracked in space and time</li> <li>Adopted for measure in living cells</li> </ul>	<ul style="list-style-type: none"> <li>Interference from autofluorescent compounds or scattered light from precipitated compounds</li> <li>Increased background from off-peak excitation in excess of acceptor, or from bleed-through of the donor emission into <math>\lambda</math> used to measure the acceptor signal</li> </ul>	[156] [157]

<p><b>IP and WB</b></p> <p>The phosphorylation is detected thanks to specific p-Tyr Ab; in some cases a first step of IP is necessary to isolate the protein of interest from total cell lysate</p>	<ul style="list-style-type: none"> <li>• Good sensitivity of the signal</li> <li>• Reduces the dangers due to the use of radioactive moieties.</li> </ul>	<ul style="list-style-type: none"> <li>• Prone to subjective results</li> <li>• High cost and technical demand</li> <li>• Semi-quantitative method</li> </ul>	
<p><b>ELISA</b></p> <p>The protein of interest is isolated from cell lysate through the binding to an antibody-coated plate. For the detection of the signal, another antibody specific for the phosphorylation site is added to the plate.</p>	<ul style="list-style-type: none"> <li>• Quantitative thanks to the use of a calibrated standard</li> <li>• High specificity for the use of two Ab in sandwich configuration</li> <li>• High sensitivity for small volume with low abundance proteins</li> <li>• Scalable to testing large number of samples</li> </ul>	<ul style="list-style-type: none"> <li>• Measure of enzyme activity can be affected by plasma constituents</li> <li>• Kit for ELISA procedures are not cheap</li> <li>• Possibility to identify false positive/negative especially with mutated antigen</li> </ul>	
<p><b>Intracellular flow cytometry</b></p> <p>Exploits a laser to excite the fluorochrome conjugated to the antibody used for the detection of the phosphorylated protein in permeabilized cells</p>	<ul style="list-style-type: none"> <li>• Detection of multiple proteins simultaneously with single cell investigation</li> <li>• Rapid and easy to perform</li> </ul> <p>Low data acquisition time</p>	<ul style="list-style-type: none"> <li>• Single cells are required for analysis</li> <li>• Cell samples must be quickly fixed to maintain phospho-epitopes</li> <li>• high expression level of proteins of interest necessary to detect the signal</li> </ul>	[158]
<p><b>Fluorescence anisotropy</b> (Fig. 1.13)</p>	<ul style="list-style-type: none"> <li>• Reduces the dangers due to the use of radioactivity.</li> <li>• Homogeneity of the sample</li> </ul>	<ul style="list-style-type: none"> <li>• Only peptides can be used as substrates</li> <li>• Peptide substrate can have a different kinetics from the native protein</li> <li>• Large amount of phospho-specific Ab are required</li> </ul>	[156]
<p><b>Mass spectrometry</b></p> <p>Isolation of phospho-proteins from a protein mixture and sequencing at the same time the phospho-residues of the target protein</p>	<ul style="list-style-type: none"> <li>• Large-scale phospho-protein analysis in complex protein mixtures</li> <li>• Good sensitivity and resolution</li> </ul>	<ul style="list-style-type: none"> <li>• Difficult identification of phosphorylation sites of a protein for: <ul style="list-style-type: none"> <li>- increased hydrophilicity and reduced retention of phospho-peptides on reversed-phase liquid chromatography</li> <li>- phosphopeptides have relatively low ion abundance</li> <li>- lower detection of phosphorylated species with respect to the un-phosphorylated ones</li> </ul> </li> </ul>	[159]

<p><b>SMI measurements</b></p>	<ul style="list-style-type: none"> <li>• Measure of the RTK activation process in living cells by analyzing membrane dynamics and oligomerization state</li> <li>• Optimal spatial and temporal resolution</li> <li>• High sensitivity</li> </ul>	<ul style="list-style-type: none"> <li>• Long time of data processing</li> <li>• Undirect information on activation process</li> <li>• Phosphorylation is inferred from the change in membrane dynamics</li> </ul>	<p>[160], [161]</p>
--------------------------------	---	--	---------------------

**Table 1.2. Table of techniques used to detect phosphorylation of kinase proteins.** Name of techniques, advantages, disadvantages; references are listed in the table. Ab: antibody.

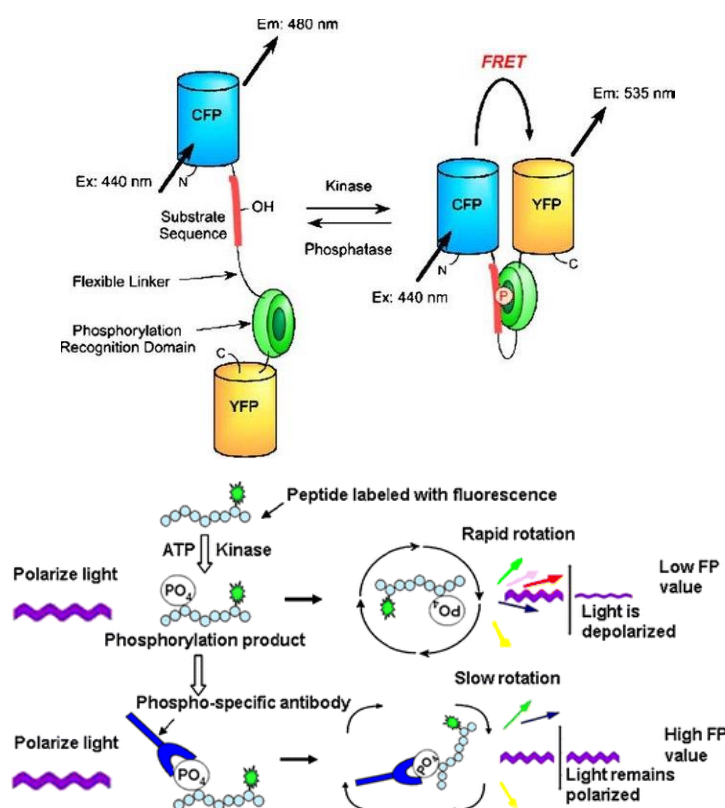


**Figure 1.13.** Upper panel: Fluorescence Resonance Energy Transfer (FRET)-based kinase assay: cyan fluorescent protein (CFP) is the donor fluorophore for FRET, linked to a substrate sequence, connected with a flexible linker with a Phosphorylation Recognition Domain (PBD), linked to the acceptor fluorophore, the Yellow Fluorescent Protein (YFP). After phosphorylation by a kinase, the substrate sequence binds to the PBD, closing up the two fluorophores and increasing the FRET signal. Bottom panel: Fluorescence-Polarization-based kinase assay. Linearly polarized light excites fluoromolecules in solutions, and they emit light more polarized in the same direction of polarization if the molecule does not move in the excited state; if the molecule changes its orientation while in its excited state, the polarization diminishes. The discrimination is based on the fact that large molecules rotate more slowly than small molecules; their change in polarization is measured monitoring the amount of fluorescence emitted with vertical and horizontal polarization, following excitation with vertical polarization. In particular, in the case of interest a fluorescently-labeled peptide in solution binds a specific antibody after phosphorylation operated by a kinase, inducing a reduction of the molecule rotation and an increase of the polarization signal. Images adapted from [156], [157].

As is clear from Table 1.2, the use of different approaches to detect and study kinase activity can help to reach a more comprehensive understanding of these molecular events. For the advantages offered by fluorescence single-molecule approaches, and for the important role these experimental approaches have had during the course of this thesis, I shall describe them in more details in the following section.

### 1.4.1 Single-molecule imaging and tracking of membrane receptors

SMI and Single Particle Tracking (SPT) allows studying the stoichiometry and the movements of single receptor molecules diffusing within the membrane. Moreover from the analysis of these two biophysical characteristics it is possible to extrapolate information about the activation state of a receptor [162], with the advantage of monitoring it in living cells and in real time. The general workflow of this kind of experiments is summarized by the following points, and described more in details in the following sections:

- i) membrane receptors are coupled to bright and photostable organic dyes; density of labelled receptors must be low enough to distinguish single labelled molecules (paragraph 1.4.1.1);
- ii) labelled molecules are imaged with a suitable microscope setup; these measures can be performed in fixed or living cells, depending on the purpose of the experiment (paragraph 1.4.1.2);
- iii) the fluorescence intensity of each detected spot can be analyzed to deliver a direct measure of how many molecules compose it (paragraph 1.4.1.3); this technique is more easy and robust in fixed cells;
- iv) in case of living cells, each detected spot can be tracked over time so that individual trajectories can be reconstructed and analyzed to extract several quantitative parameters about receptor membrane diffusivity (paragraph 1.4.1.4).

During the last years, several works adopting SMI approaches allowed to define a direct cause-effect relationship between RTKs activation and immobilization/oligomerization at cell surface: studies on TrkA-wt membrane mobility measured by TIRF microscopy combined with SPT were predictive of TrkA function, with membrane receptor immobilization and clustering being a signature of the activating ligand [161]. Similar results of ligand-dependent effect are reported also for EGFR [163], FLS2 receptor-like kinase [164] and insulin receptor kinase [165]. The study of dynamic processes at cellular and molecular level have been made possible thanks also to the development of super-resolution fluorescence imaging techniques that offer the possibility to monitor dynamics in the order of sub-ms time scale. Single molecule imaging and tracking can be considered one of them,

since it is possible to localize fluorescent molecules below the diffraction limit of the microscope, reaching a localization uncertainty around tens of nanometers or slightly less.

### 1.4.1.1 Membrane density and chemical labelling of membrane receptors

One of the fundamental point to verify when you want to perform a SMI/SPT experiment is the low density of labelled molecules [166], condition that allows to track single labelled molecules. Since it is important to label all the receptors exposed at cell surface, the possibility to control the protein expression is very useful, and an efficient method in this case is the use of lentiviral inducible expression vectors [167]; in particular we used a TET-ON lentiviral system that allows regulating quantitatively the expression of the receptors depending on the concentration of the promoter inducer doxycycline [168], [169]. Another fundamental aspect to consider when you want to perform SMI and SPT experiments is the choice of the suitable fluorescent labels to detect the probe of interest. Chemical tags as SNAP-, Halo- and ACP-tags functionalized with organic dyes represent a good system to label proteins in living cells, ensuring a 1:1 stoichiometry [170], and it is recommended when imaging and counting single molecules are required. With respect to fluorescent proteins (FPs), the organic dyes have higher brightness and photostability (the photon outputs before bleaching is  $10^6$  to  $10^8$  for organic dyes versus  $\sim 4 \times 10^5$  for the best FPs [171]), fundamental features for long time of acquisition with a high signal-to-noise ratio. In particular, acyl and peptidyl carrier protein (ACP and PCP) derived chemical tags were applied extensively by our group to the labelling of NTs and their receptors [160], [162], [168], [172], [173] (see also Appendix A). Concerning membrane proteins, these short peptides, once inserted at their ECD, have low steric footprint on its structure and function, and do not interfere with the protein translocation at plasma membrane. Previously our group demonstrated specifically that the fusion of ACP-tag at the N-term of the TrkA protein preserves both its functions and signaling abilities [160]. The high specificity of tag recognition by phosphopantetheinyl transferase enzymes (PPTases) allows easy, covalent labelling with any molecule conjugated to Coenzyme A (CoA) substrate, as biotin or organic dyes [174] (Fig. 1.14); briefly, the synthases transfers the phosphopantetheinic (Ppant) arm of the CoA to the target tag exposed by the protein (Fig. 1.14). Furthermore, the evidence that both CoA and PPTases are not permeable to plasma membrane makes this technique ideal for the investigation of membrane proteins after performing the labelling reaction in the cell medium prior to imaging (see Appendix B).

When receptors needs to be tracked for a long time of acquisition, it is advisable to label them with Quantum dots (Qdots), nanoparticles characterized by high brightness and photo-stability, that ensure to avoid bleaching phenomena (see details in paragraph 4.11); we used biotin-CoA as substrate of PPTases for the reaction (Fig. 1.14), and this allowed to bind streptavidinated QDots.

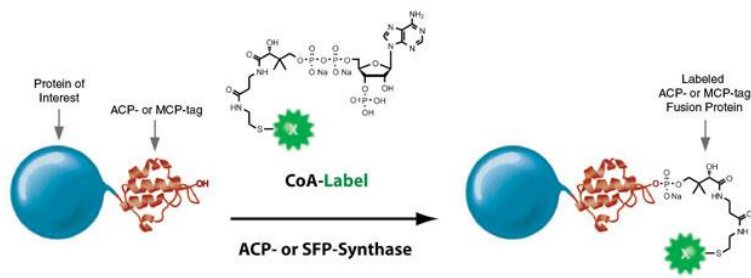


**Figure 1.14.** ACP-labelling reaction: Scheme of the PPTase-based labelling of ACP-tagged receptors by CoA-conjugates. ACP tag exhibits a hydroxyl group of a serine residue recognized by the PPTase. The labelling molecule (green balloon) can be a fluorophore, biotin etc. Image taken from <https://www.addgene.org/depositor-collections/neb-cell-imaging-tags/>.

### 1.4.1.2 TIRF microscopy acquisition

To monitor the motion of single-pass transmembrane molecules exposed at the cell surface, a temporal resolution of about tens of milliseconds in a field of view containing a large part of plasma membrane is necessary; this is possible by coupling a wide-field microscopy with a fast electron-multiplying charge coupled device (EM-CCD) camera.

A good example of a wide-field technique applied for SPT measurements is the total internal reflection fluorescence microscopy (TIRFm), which allows exciting fluorescent molecules in a range around 100 nm close to a glass/water interface. The system exploits a collimated laser beam incident on the glass-water interface above a critical angle, ensuring that the light is internally reflected totally. This is possible when the light travels from a medium with a higher refractive index (e.g. glass) to a medium with a lower refractive index (e.g. water or an aqueous medium). In this way, the incident light induces the generation of an evanescent wave inside the sample volume, with an energy density that decreases exponentially with the distance from the glass-water interface; in this way, fluorophores are excited only in a region immediately adjacent to the interface. This specific characteristic of TIRFm allows visualizing only the labelled particles exposed on the bottom plasma membrane, reducing the background signal from molecules too far from the glass/water interface (Fig. 1.15).

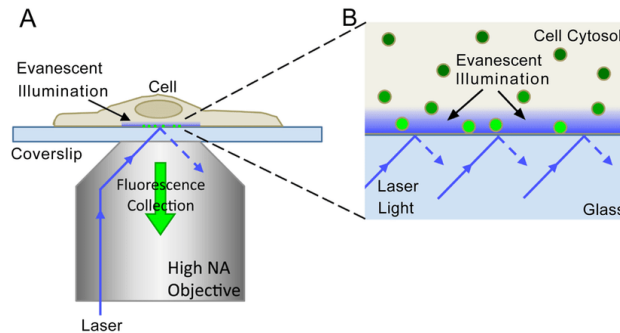


**Figure 1.15. A)** In TIRFm through objective, the collimated beam of a laser is directed through a high Numerical Aperture (NA) objective to the glass coverslip such that it is incident on interface at an angle greater than the critical angle, resulting in total internal reflection. This generates an evanescent wave that illuminates a short depth ( $\sim 100$  nm) into the cell. The fluorescence excited by this evanescent illumination is collected through the same objective. **B)** Magnification of the evanescent wave at the interface cell/coverslip: the energy emitted from the evanescent wave decays exponentially with depth, reducing the background of particles located far from the interface. Image taken from [175].

### 1.4.1.3 Stepwise photobleaching method

The analysis of the intensity within trajectories in living cells (see next section) does not always give clear information about the stoichiometry of proteins, *e.g.* because of photobleaching events during the acquisition, because oligomerization events are too transient to be captured, and in general by the noisier signal arising from a moving fluorophore. To overcome these limitations, the analysis of stepwise photobleaching represents an efficient method to evaluate the oligomerization state of membrane proteins, such as RTKs. The approach is based on the assumption that if inside a diffraction-limited spot (Fig. 1.16 A, yellow squares) there is a protein complex, it is possible to extrapolate information about its stoichiometry by counting the number of photobleaching events following a long-enough excitation [176]. This is possible because the stoichiometry of the fluorolabelling reaction is 1:1 fluorophore:receptor, organic fluorophores are sensitive to photobleaching and their intensity profile is quantized (each single molecule excited by the same light has the same brightness). From the distribution of photobleaching steps, it is possible to obtain the stoichiometry of a protein complex: one photobleaching step corresponds to a monomer, two photobleaching steps to a dimer and so on (Fig. 1.16 B). Recently, the use of this technique allowed solving an enigma investigated for more than 30 years in the NTs community with very controversial results: the stoichiometry of the P75<sup>NTR</sup> receptor [169]. Our group measured the intensity step-photobleaching profile of P75<sup>NTR</sup> molecules labelled with Abberior 635P and analyzed both the number of photobleaching steps and the mean intensity of the spot before bleaching ( $I_{pre}$ ) (Fig. 1.16). From the comparison among the distributions of photobleaching steps of P75<sup>NTR</sup>-wt and two control constructs constituted by a constitutive monomer (mutP75<sup>NTR</sup>) and dimer (dimP75<sup>NTR</sup>) of p75<sup>NTR</sup>, we demonstrated for the first time the

mostly monomeric nature of P75<sup>NTR</sup> at low surface density (Fig. 1.16 C), overcoming the limits in stoichiometry quantification intrinsic in biochemical approaches [169] (Fig. 1.16 C).

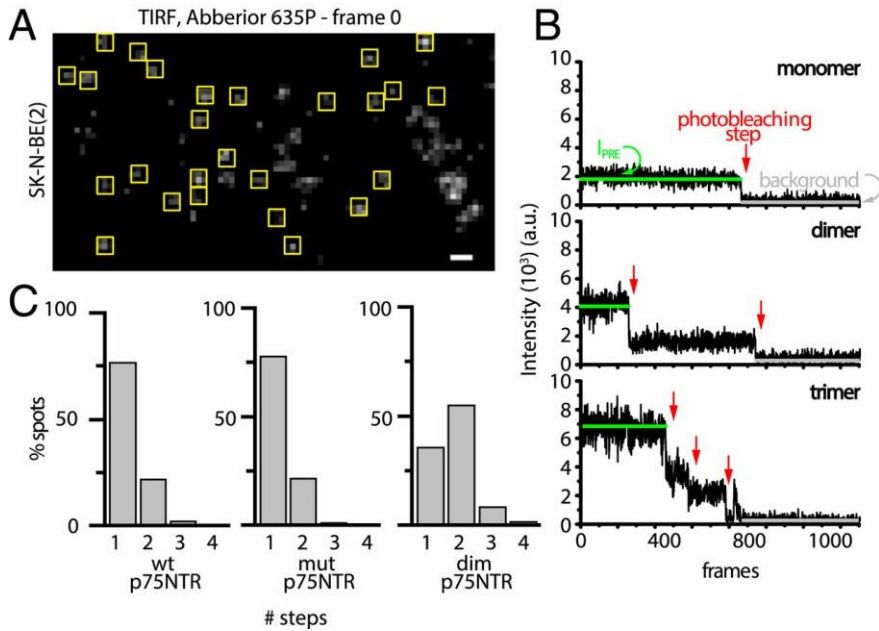


**Figure 1.16.** **A**) Representative TIRF image of fluorescent receptor spots on the surface of fixed SHSY5Y cells (yellow squares highlight the analyzed spots); scale bar: 1  $\mu\text{m}$ . **B**) Typical Intensity traces of a monomer, a dimer and a trimer showing the parameters considered in the calculation: the green line represents the mean intensity before the first photobleaching step ( $I_{pre}$ ), red arrows point to single photobleaching steps, while the grey line indicates background intensity. a.u., arbitrary units. **C**) Percentage of photobleaching steps counted per trace for wtP75<sup>NTR</sup>, mutP75<sup>NTR</sup> and dimP75<sup>NTR</sup>. Image taken from [169].

### 1.4.1.4 Single Particle tracking

After SMI acquisitions of living cell samples, several time series of moving fluorolabelled spots in the imaged area with a frame time in the order of ms or hundreds of  $\mu\text{s}$  are typically obtained. Here, the first step of SPT analysis (Fig. 1.17) consists in the detection and localization of the precise positions of these moving spots in each frame of the acquired movie, obtained by identifying the center of the diffraction-limited spot of the fluorescent probe. We can obtain this information calculating the intensity-based centroid of the spot or by fitting the diffraction-limited Airy disk with an appropriate peaked function (as a Gaussian one), thus reaching a sub-pixel, nanometric localization precision [177].

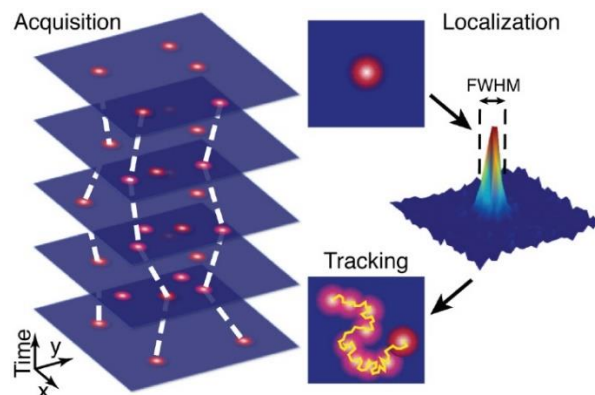


**Figure 1.17.** Scheme of SPT analysis: during the acquisition step, a series of images with labelled moving spots (red spots) are taken; typical movies contains 100 to 1000 images recorded with an high speed camera. Then the detection and localization step identifies spots in each frame, whose position is obtained by the center of the diffraction-limited spot of the fluorescent probe. After repeating the localization step on a time-series of images, the positions are linked to generate trajectories of the moving particle (see the white dashed lines on the acquisition images where individual particles are linked as a function of time). Images taken from [178].

The trajectories (sequences of particle positions and/or of fluorescence intensities of the spots as a function of the frame number) were obtained connecting the position of the detected spots considered to correspond to the same particle in different frames of a movie. Typically, this step is performed with tracking software tools, as Imaris Bitplane software; from each  $xy$ -trajectory, it is possible to extract quantitative parameters, such as the anomalous coefficient  $\gamma$  or the diffusion coefficient  $D$ , useful to classify the receptor diffusion model.

Many methods for extracting the above-mentioned parameters require the analysis of the Mean Square Displacement (MSD) for each trajectory [179], [160]. The shape of the MSD against lag time can characterize the type of motion of particles, if it can be conveniently fitted with alternative Brownian, directed or confined models [160] (Fig. 1.18); using an anomalous diffusion fit (a power-law with exponent  $\alpha$ , eventually shifted) allows instead a more continuous classification of (sub/super) diffusive dynamics [162] (Fig. 1.19). More in details, particles that move with Brownian motion (Fig. 1.18, left panel) have an MSD that increases linearly with time, while particles characterized by a confined motion (Fig. 1.18, right panel) have the MSD that rapidly reaches a plateau. The drifted particles are characterized by a superlinear MSD, with a parabolic behavior if the drift velocity is constant (and a strictly positive initial slop if the drift is superimposed to a Brownian motion, see Fig. 1.18, middle panel).

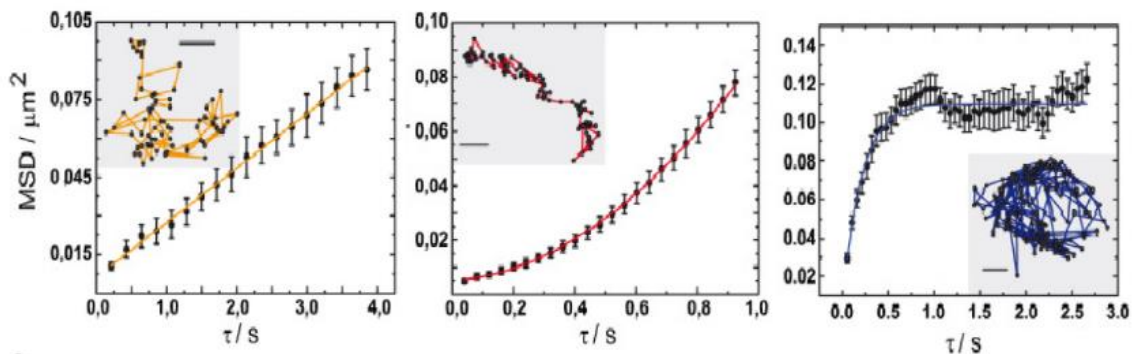


**Figure 1.18.** MSD plot versus lag time ( $\tau$ ) for trajectories representing three types of motion (shown in the insets; bar:  $0,16 \mu\text{m}$ , corresponding to 1 pixel in the images). Left panel: Brownian (yellow curve); middle panel: drifted (red curve), right panel: confined (blue curve). Images adapted from [160].

The MSD analysis works appropriately when the mode of motion of a particle is constant during time; in this case the trajectory is defined “self-similar” or unimodal [160]. However, more frequently long trajectories of moving

particles are characterized by multimodal dynamics, due to the alternation of free diffusion and phenomena of transient molecular crowding or interactions within membrane (nano-) domains, such as actin-rich regions, caveolae, lipid raft or others. In order to classify automatically a trajectory as unimodal instead of multimodal, we checked the linear proportionality in the Moment Scaling Spectrum (MSS); from this analysis we derived also the coefficient of anomalous diffusion  $\gamma$ . The  $\gamma$  coefficient has values very close to the  $\alpha$  one, at least for unimodal trajectories like that one, it characterizes the motion of particles [180]: if  $\gamma$  is close to 0.5, particles move with a Brownian motion; for values greater than 0.5 we are in presence of superdiffusive dynamics (typical of directed motion), while values lower than 0.5 characterize subdiffusive dynamics, typical of confined motion (Fig. 1.19).

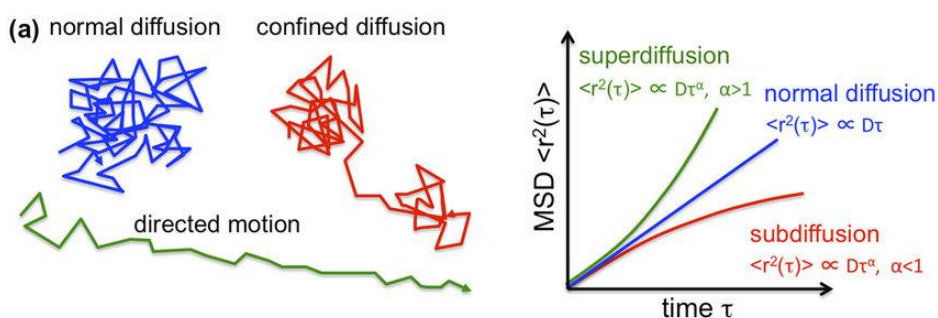


**Figure 1.19.** Different types of diffusion (normal or Brownian, confined and directed or drifted) corresponding to different shapes of the MSD in function of the lag time. In particular for  $\alpha=1$ ,  $\alpha < 1$  and  $\alpha > 1$  trajectories are classified respectively as normal (i.e. Brownian), subdiffusive and superdiffusive. The angular coefficient in the linear fit of the moment scaling spectrum (MSS) have values very close to  $\alpha/2$ , especially for unimodal trajectories.

After the partition between unimodal and multimodal trajectories, the latter were analyzed and divided in sub-trajectories applying the Transient Arrest of Diffusion (TAD) algorithm [161], based on the detection of non-random transient confinement zones [181]: the TAD algorithm separates segments of trajectories corresponding to confined regions from those characterized by diffusive and drifted motion. Finally, from the analysis of MSD and MSS of the pool of (sub) trajectories obtained from the whole analysis, it is possible to extrapolate the typical quantitative parameters of trajectories [161].

The application of SPT on membrane proteins represents a powerful tool to understand biological mechanisms underpinning their function in the membrane. During these years, the combined approach of SMI and SPT analysis solved different questions about the mechanism of activation and oligomerization state of RTKs. The work of Chung et al., for example, demonstrated that EGFR was present in two different states of oligomerization, one monomeric (in unbound state) freely to diffuse on cell surface and another dimeric correlated with the receptor activation state [163]. For the analysis of the trajectories, they extracted from them quantities related to the derivative of the square of the displacement as a function of time (cumulative square displacement, CSD).

Analysis of trajectories allowed to unveil several unresolved features of the activation processes of neurotrophin receptors TrkA and p75<sup>NTR</sup> signaling network [154], [166], [171], [172]. Thanks to the SPT approach it was possible to find a functional relation between TrkA lateral mobility and its activation in response to ligand binding [161]. In particular, from the analysis of trajectories TrkA results characterized by a bimodal distribution of D coefficient with ~70% of molecules moving at the highest D value (Fig. 1.20, left panel); however, NGF stimulation induces a reduction of the fast population in favor of the slow/immobile fraction, in agreement with a shift of the monomer-dimer equilibrium towards the dimeric form [162], [182], as obtained from the analysis of the fluorescence intensity of the spots [162]. The distribution of D and  $\gamma$  values obtained for each trajectory, normalized for the relative trajectory length, was plotted on a bi-dimensional map of probability [161] (Fig. 1.20, right panels). In this plot, we defined eight different areas (numbered from 1 to 8, as in [161]) associated to particular dynamic modes of membrane TrkA receptor, corresponding to different biological processes; the relative weight of trajectories identified for each areas was quantified and plotted in stack column-histograms [161].

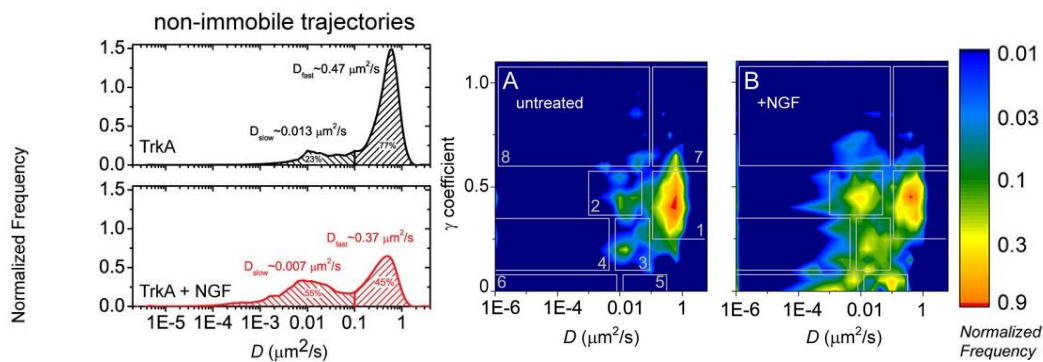


**Figure 1.20.** Left: distribution of the diffusion coefficient (D) of labeled ACP-TrkA receptors for non-immobile trajectories in presence (red curve) or absence (black curve) of NGF stimulation. The area under the curve is normalized to the fraction of spots in non-immobile trajectories. Right: maps of probability for the D- $\gamma$  distribution of ACP-TrkA trajectories in absence (panel A) and presence of NGF stimulation (panel B); dynamic areas (from 1 to 8) are superimposed on each plot. On the right, the logarithmic color scale for the frequency of the D- $\gamma$  distribution, normalized to 1 at the peak.

# 2. MOLECULAR INSIGHT ON THE ALTERED MEMBRANE TRAFFICKING OF TRKA KINASE DEAD MUTANTS

---

## 2.1 BACKGROUND AND RATIONALE OF THE WORK

Auto-inhibitory mechanisms in RTKs (see Paragraph 1.1.3), based *e.g.* on the position of  $\alpha$ C helix, or on the conformation of the A-loop, exist to prevent TKD activation in the unbound state [2]. These are released upon ligand binding, which results in efficient activation of the kinase activity. The catalyzed phosphotransfer reaction from ATP onto the hydroxyl group of Tyr represents an important PTM, evolutionarily conserved from prokaryotes to humans. Accordingly, the TKD of RTKs is highly conserved. A growing number of mutations in RTKs, associated to several disorders [34], are reported to occur in key regulatory elements of their TKD (see Paragraph 1.1.2). Typically, kinase hyperactivating mutations are found in cancer and kinase inactivating mutations in developmental and genetic disorders [178, 179]. Furthermore, mutations of the residues coordinating ATP or performing catalytic activity are found in a subfamily of RTKs named pseudokinases [34], [58]. Although lacking kinase activity, these proteins have signaling abilities and play important physiological and pathological roles (see Paragraph 1.1.4). However, the molecular basis underlying the functions of kinase-inactivating or pseudokinase mutations has been poorly investigated.

I addressed the contribution that specific mutations have in the structure and function of the TKD of TrkA receptor (described in Paragraph 1.3), and how this in turn impacts its membrane dynamics, intracellular trafficking and PTMs. TrkA plays fundamental roles in the development of the nervous system [180, 181], and mutations of TrkA sequence are reported both in cancer [188] and in HSAN IV genetic disease [189]. In particular, I focus my attention on the mutation of lysine 544 (human numbering) in the  $\beta$ 3 sheet of the TKD N lobe, which is crucial to allocate ATP and thus to kinase activity; noteworthy, this mutation resembles those displayed by pseudokinases [34]. ATP binding to Lys 544 is an upstream event during TrkA TKD activation [21, 91], which drive phosphorylation of Tyr of the AL (Y676, Y680, Y681 [190], [191]), and of scaffolding Tyr (Y496, Y757, Y791 [192]–[194]). Furthermore, Lys 544 was reported to be important for TrkA ubiquitination [94], [128]. I provide evidence that the mutation of this Lys to Asn slows down membrane dynamics in a manner that paradoxically resembles that of NGF-activated TrkA-wt ([162] and paragraph 1.4.1.4). However, the two membrane immobilization modes have distinct structural and functional determinants, which are here characterized. Our observations may

possibly be extended to other RTKs, thus providing interesting cues to the study of their genetic or somatic mutations.

This chapter presents experimental data contained in the manuscript “*Molecular insight on the altered membrane trafficking of TrkA kinase dead mutants*” with authors **R. Amodeo\***, R. Nifosì, C. Giacomelli, C. Ravelli, L. La Rosa, A. Callegari, M.L. Trincavelli, S. Mitola, S. Luin, L. Marchetti. *BBA Molecular Cell Research*, 2020. Most experiments and data analysis were performed by Rosy Amodeo, with help from other coauthors. Crucial contributions came from Riccardo Nifosì (CNR-IN, Pisa, Italy), who performed Molecular Dynamics Simulation, and the group of Prof. Stefania Mitola (Department of Molecular and Translational Medicine, University of Brescia), providing S6-VEGFR2 constructs and relative biochemical investigations.

## 2.2 EVALUATION OF MEMBRANE MOBILITY AND SURFACE EXPOSURE OF DEAD-KINASE RECEPTORS

In paragraph 1.4.1.4 we described that SPT measurements made on *rat* and *human* TrkA (here referred to TrkA and *hTrkA*, respectively; see Table 1.1 in paragraph 1.3.1) membrane motion [161], [183], [195] unveiled that NGF elicits a strong immobilization and clustering of the receptor at cell surface [162]. In order to unequivocally validate the relationship between membrane immobilization and receptor activation, we engineered an ACP-tagged TrkA in which Lys547 (see Table 1.1) placed in the ATP-binding pocket was point-mutated to Asn (Fig. 2.1 A). Because the above-mentioned substitution occurs in a conserved residue of the TKD (see Paragraph 1.1.2 and Fig. 2.1 A), it is commonly adopted as TrkA kinase-inactive variant (Table 2.1), despite its ability to bind NGF is completely preserved (Fig. 2.1 B).

Both TrkA-wt and -K547N were transfected in SHSY5Y cells, their membrane pool labelled with Qdots and imaged by TIRF with single-molecule resolution (see paragraph 1.4.1.1 and 1.4.1.2). Visual inspection of the moving spots and relative trajectories (Fig. 2.1 C) suggested that TrkA-K547N moves slower, exploring smaller regions of the membrane, compared to TrkA-wt. Quantitative analysis of the diffusion coefficient (*D*) of mobile trajectories confirms that, similarly to TrkA-wt, TrkA-K547N displays a bimodal distribution of *D* values. However, in this case the faster population is slowed down (peaked at 0.2  $\mu\text{m}^2/\text{s}$  versus 0.3  $\mu\text{m}^2/\text{s}$ ) and significantly decreased by about 43% (Fig. 2.1 D), matching with an increase of slower, confined and immobile receptors, characterized by a lower *D* (peaked at 0.005  $\mu\text{m}^2/\text{s}$  versus 0.013  $\mu\text{m}^2/\text{s}$ , Fig. 2.1 D).

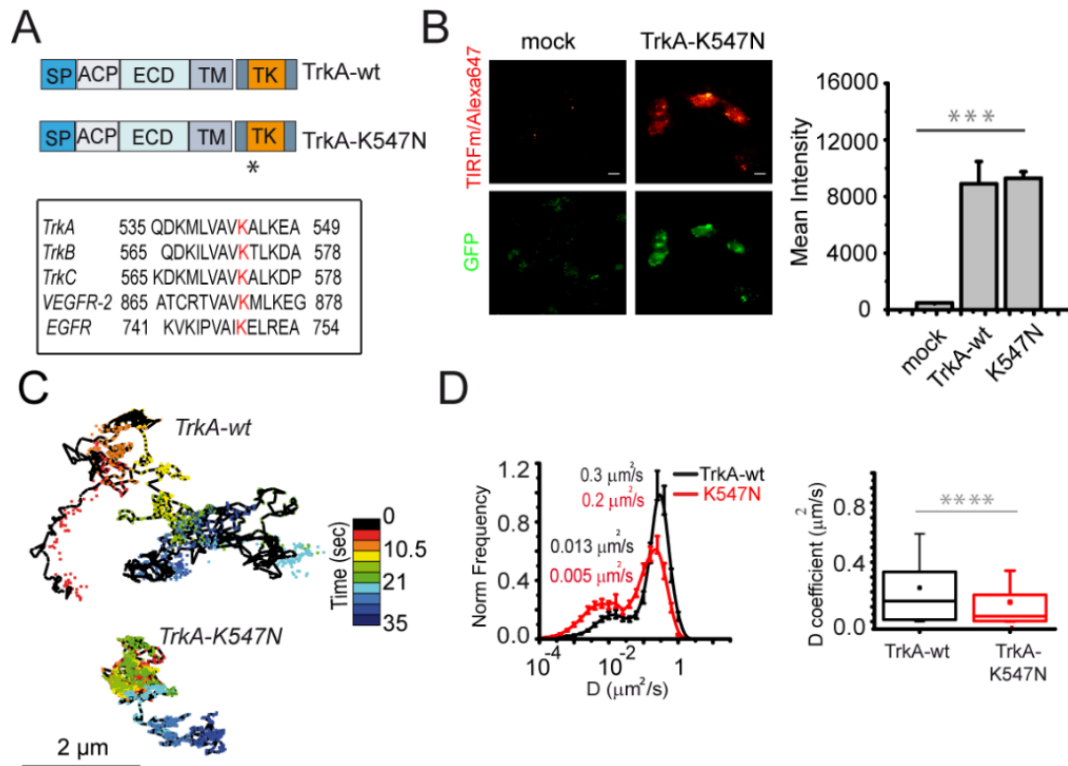


**Figure 2.1.** **A)** Scheme of TrkA-wt and TrkA-K547N (SP: signal peptide, ACP: acyl carrier protein tag, ECD: extracellular domain, TM: transmembrane domain, TK: Tyrosine Kinase domain, inside the intracellular domain); the asterisk highlights where the mutation is located. Below: sequence alignment of a portion of TKD for human TrkA, TrkB, TrkC, VEGFR2 and EGFR proteins; the conserved Lys residue positioned in  $\beta 3$  sheet is showed in red in all kinases. **B)** Left: representative TIRF images of SHSY5Y cells not-transfected (mock, left) and expressing TrkA-K547N along with GFP (right), after incubation with Alexa647-labelled NGF; scale bar: 10  $\mu\text{m}$ . Right: the corresponding quantification of Alexa647-NGF mean intensity  $\pm$ sem, imaged at the surface of plasma membrane of SHSY5Y expressing TrkA-wt and TrkA-K547N, compared to the same signal in non-transfected cells ( $n = 20$  cells pooled from two independent cover slips). \*\*\* $p < 0.001$  according to one-way ANOVA with Bonferroni's Multiple Comparison test. **C)** Typical trajectories obtained for moving Qdot particles corresponding to TrkA-wt (top) and -K547N (bottom). **D)** Distribution of diffusion coefficient ( $D$ ) and estimated uncertainty obtained from mobile TrkA-wt (black curve,  $n = 1989$ ) and -K547N (red curve,  $n = 1558$ ) trajectories. Right: Box-plot for the corresponding  $D$  values retrieved from trajectories (at least 6 frames long) of TrkA-wt (black,  $n = 1116$ ) versus TrkA-K547N (red,  $n = 2640$ ) in SHSY5Y cells in resting conditions. Trajectories are pooled from three independent measures. Boxes: 25<sup>th</sup>-75<sup>th</sup> percentiles; whiskers: 10<sup>th</sup>-90<sup>th</sup> percentile; line: median; square: mean. \*\*\*\* $P < 0.0001$ , according to Mann-Whitney test.

TrkA cDNA sequence	Mutation	References
human	K544A	[196]
	K544R	[128]
	K544N	[197]
rat	K547A	[198][199]
	K547N	[200]
	K547N	[201]
	K547R	[202]
	D671A	[203]

**Table 2.1. Different kinase-null mutants of TrkA receptor reported in the literature.** Numeration of amino acids corresponds to isoform I of human and rat cDNA sequences deposited in UniProtKB database (<https://www.uniprot.org/uniprot/P04629>). Human K544 corresponds to rat K547.

Furthermore, we adopted here a classification for receptor modes of motion in “immobile”, “confined” and “diffusive” categories (Fig. 2.2), based on the D- $\gamma$  maps of TrkA membrane dynamics published by our group (see Paragraph 1.4.1.4, Fig. 1.20). The diffusive population is characterized by D values between 0.1 and 1  $\mu\text{m}^2/\text{s}$  and  $\gamma$  value greater than 0.25, the immobile one by D value below 0.01  $\mu\text{m}^2/\text{s}$  and  $\gamma$  value up to 0.1, and the “confined” fraction includes the slower and/or confined trajectories (approximately, with D below 0.1  $\mu\text{m}^2/\text{s}$  and  $\gamma$  value above 0.1, with D between 0.01 and 0.1  $\mu\text{m}^2/\text{s}$ , or with D between 0.1 and 0.3  $\mu\text{m}^2/\text{s}$  and  $\gamma$  value up to 0.1) [159, 190].

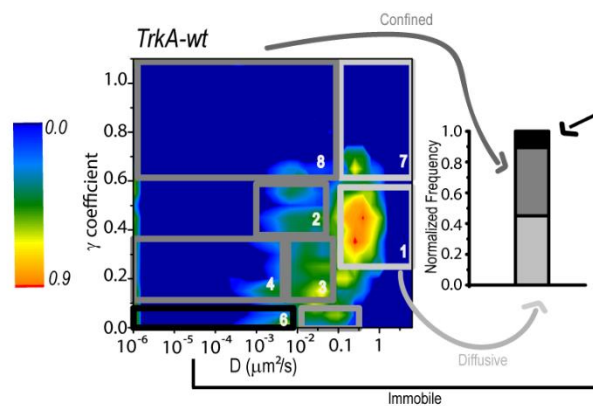


**Figure 2.2.** Left: map of probability for the D- $\gamma$  distribution of TrkA-wt ( $n=13$  cells, 1989 trajectories) in non-stimulated cells. On the left, logarithmic-scale color code for the frequency of the total D- $\gamma$  distributions, normalized to 1 at the peak. D- $\gamma$  regions highlighted by the light-gray, gray and black boxes superimposed on each plot correspond to trajectories respectively classified as diffusive, confined and immobile in this work. On the right, histograms of normalized frequency obtained from the sum of diffusive (light grey), confined (grey) and immobile (black) regions, as indicated by the arrows of corresponding color.

We used this new kind of classification and plot for evaluating whether NGF binding changes the dynamics of TrkA-K547N (Fig. 2.3 A), similarly to what observed previously for the wt counterpart [162]. For this reason, we analyzed by SPT the effect of 15 minutes NGF stimulation in the two cases. From the analysis of the D distributions, we verified that NGF-stimulated TrkA-wt displays a significant slowdown and reduction of the fast-diffusing population (Figs. 2.3 A, B lower panel, C) and a 34% increase of the immobile mode of motion (Fig. 2.3 A,D and [162]). When analyzing the same for TrkA-K547N, we again found a significant slowdown and reduction of fast-diffusing trajectories, but this was not as prominent as in the TrkA-wt case (Fig.2.3 A and B upper panel). In addition, immobilization is less represented for TrkA-K547N than for TrkA-wt in the presence of NGF (Fig.2.3 A). We also calculated the distribution of confinement length (L) for non-mobile trajectories [162] of TrkA-K547N (Fig.2.3 D), observing no significant changes upon NGF stimulation, as instead we observed for the wt counterpart

(Fig.2.3 D). These data indicate that NGF has an effect on TrkA-K547N membrane dynamics, but weaker than on the TrkA-wt one and with different features.

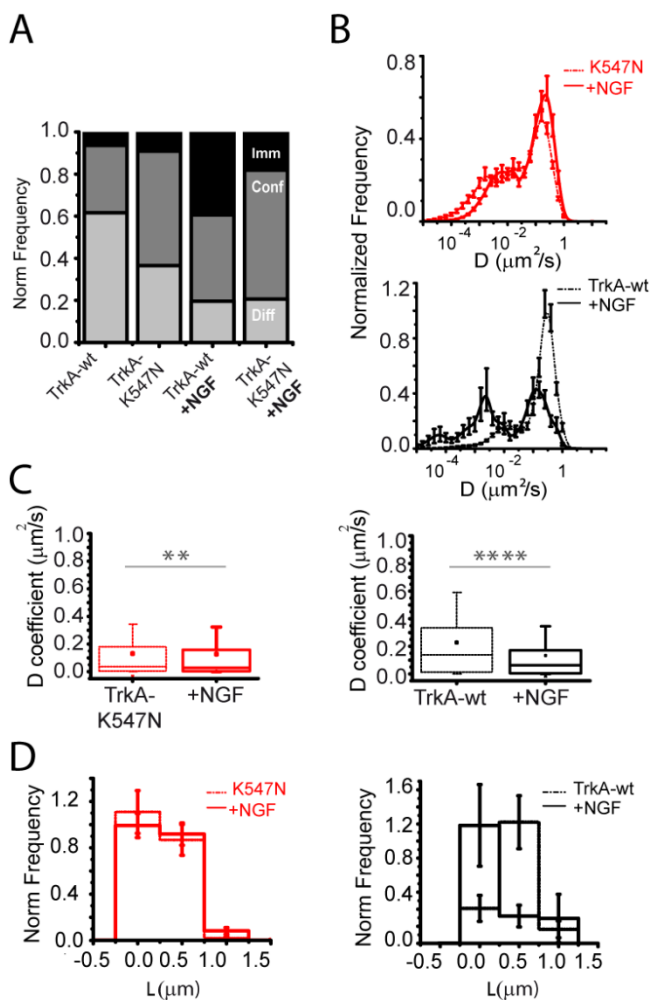


**Figure 2.3** **A)** Stack-column histogram plot of receptors undergoing diffusive (light-grey), confined (grey) or immobile (black) modes of motion for TrkA-wt in resting condition (n=3133 trajectories) and after NGF administration (n=513 trajectories), TrkA-K547N in resting condition (n=3625 trajectories) and after NGF administration (n=2909 trajectories). The total analyzed population was normalized to 1. **B)** Upper panel: distribution of D coefficient of mobile trajectories for TrkA-K547N after NGF administration (red solid curve, n=2909 trajectories); the D distribution of TrkA-K547N in resting conditions (red dotted line, same as in Fig. 2.1D) is reported as a reference. Bottom panel: distribution of D coefficient of mobile trajectories for TrkA-wt after NGF administration (black solid curve, n=529 trajectories); the D distribution of TrkA-wt in resting conditions (dotted line, same as in Fig. 2.1D) is reported as a reference. **C)** Left: Box-plot for D values retrieved from trajectories (at least 6 frames long) of TrkA-K547N before (red dotted line, n=2640) and after NGF stimulation (red solid line, n=2909). Trajectories are pooled from three independent experiments. Right: box-plot for D values retrieved from trajectories (at least 6 frames long) of TrkA-wt before (black dotted line, n=1116) and after NGF stimulation (black solid line, n=529). Trajectories are pooled from three independent experiments. Boxes: 25<sup>th</sup>-75<sup>th</sup> percentiles; whiskers: 10<sup>th</sup>-90<sup>th</sup> percentile; line: median; square: mean. \*\*\*\*P<0.0001, \*\*P<0.01, according to Mann-Whitney test. **D)** Distributions of confinement length (L) with estimated uncertainties for non-mobile trajectories of Qdot-labelled TrkA-K547N in the presence (red solid curves; n<sub>TrkA-K547N</sub>=616) or absence (red dotted curves; n<sub>TrkA-K547N</sub>=572) of 125 ng/ml NGF. p=0.38 (TrkA-K547N) according to  $\chi^2$  test. Right: distributions of confinement length (L) with estimated error for non-mobile trajectories of Qdot-labelled

TrkA-wt in the presence (black solid curves; n<sub>TrkA-wt</sub>=101 trajectories) or absence (black dotted curves; n<sub>TrkA-wt</sub>=290 trajectories) of 125 ng/ml NGF. p=4.9×10<sup>-4</sup> (TrkA-wt) according to  $\chi^2$  test.

Interestingly, another important feature we found is that the slower TrkA-K547N membrane dynamics displayed in resting conditions correlates with a 3-fold higher density of receptor molecules labelled and detected on the cell surface; densitometric analysis of western blot from whole cell lysates suggests that this is not due to an increase of the total protein level (Fig. 2.4 A,B).

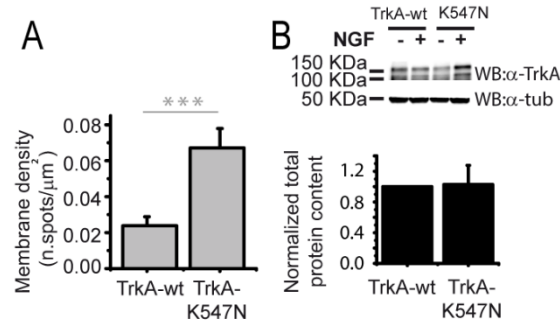


**Figure 2.4. A)** Quantification of density of labeled receptors per cell area obtained from three experimental replicates (n=22 cells for TrkA-wt, n=34 cells for TrkA-K547N). \*\*\* $p < 0.001$  according to two-tailed Mann-Whitney test. **B)** Upper: representative WB showing TrkA- levels in the absence (-) or presence (+) of 10 minutes stimulation with 125 ng/ml NGF, in SHSY5Y cells transfected with TrkA-wt and TrkA-K547N. Cell lysates were immunoprecipitated (IP) with anti-Trk (C-14) antibody and blotted with anti-TrkA antibody and subsequently stripped and re-blotted with anti-tubulin antibody. Below: densitometric analysis of total TrkA-wt and TrkA-K547N bands obtained averaging four independent blots from unstimulated SHSY5Y cells; the densitometric content of TrkA-K547N was normalized to that of TrkA-wt; error bars are standard errors.

Thus, this specific point mutation at lysine 547 alters both receptor lateral mobility and exposure at the cell surface, even in the absence of NGF stimulation.

Therefore, we investigated if NGF has an effect also in clearing this membrane accumulation, similarly to the internalization occurring for activated, signaling-competent NGF-TrkA complexes [101], [103], [206]. To this purpose, we set up a single-molecule internalization assay in which the density of membrane receptors of the two constructs was monitored by TIRFm at eight time points within 60 minutes after NGF addition to the cell medium (Fig. 2.5), and also without NGF addition as control. As we expected, the membrane pool of TrkA-wt decreases already at 5 min after NGF stimulation, most likely due to internalization of NGF-activated receptors (see paragraph 1.2.3); this decrease becomes significant at 30 min and clearance of ~60% of the moving receptors from the cell membrane is accomplished after 40 minutes. On the contrary, TrkA-K547N maintains a constant level of receptors exposed at the cell membrane up to 15 minutes after NGF stimulation, and reaches a significant ~36% decrease only after 50 minutes. This could be likely ascribed to a slower internalization route undergone by this mutant receptor upon NGF binding, considering that in absence of stimulus the membrane pool of receptors did not display significant differences during 1 hour of acquisition (Fig. 2.5 C). These results suggest that TrkA-K547N remains more time at the plasma membrane despite NGF stimulation, indicating an impairment of internalization for this mutant, at least within the same time window at which most of the internalization occurs for NGF-activated TrkA-wt. This data indicates that: i) the correct timing of internalization depends on the integrity of receptor kinase activity; ii) TrkA internalization occurring after the ligand binding is not exclusively mediated by receptor activation, as also ligand-bound inactive receptors are internalized to an extent higher than constitutive recycling (Fig. 2.5 C).

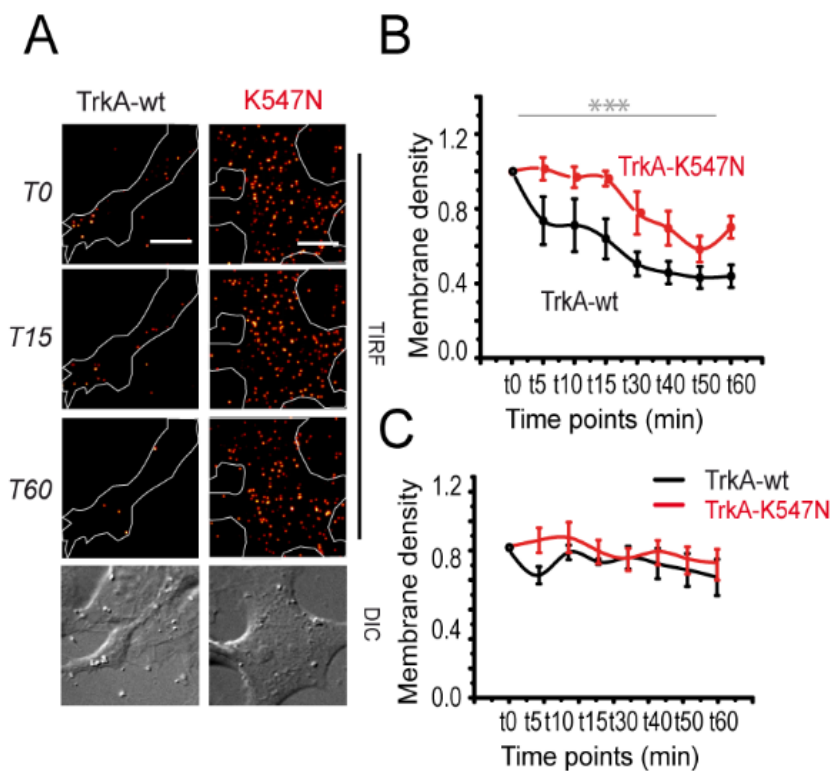


**Figure 2.5.** **A)** TIRF images of Qdot-labelled single receptor spots during a time-course lasting 60 minutes after stimulation with 125 ng/ml NGF. Every image corresponds to a time point for the same cell: t0 (time of NGF administration), t15, t60 minutes. Below: corresponding DIC image of the cell followed during the time-course. Scale bar: 10  $\mu$ m. **B)** Corresponding membrane spot density quantification for TrkA-wt and TrkA-K547N at the different time points is reported as mean $\pm$ sem from cells acquired at each time point, normalized for the spot density measured at time 0 of the corresponding cell. \*\*\* $p_{\text{construct}} < 0.001$  and  $p_{\text{time}} < 0.001$ , according to two-way ANOVA. All data are pools of 15-20 different cells collected in three independent replicas. **C)** Surface density quantification for TrkA-wt and TrkA-K547N spots at the different time points in the absence of NGF stimulation. Each value is plotted as mean $\pm$ sem of the data from the same cells (n=5) acquired at different times, normalized by the spot density measured at time 0 for the corresponding cell. Differences at different times point for each construct are not significant according to two-way ANOVA.

### 2.3 A STRUCTURAL REARRANGEMENT IS RESPONSIBLE FOR TRKA-K547N MEMBRANE IMMOBILIZATION

Mutation of Lys547 in TrkA sequence impairs phosphorylation of Tyr residues that regulates kinase activity, recruitment of intracellular effectors [207] and also receptor ubiquitination [94]. As impairment of any of these functions may potentially lead to the observed altered membrane dynamics (Fig. 2.1 D, Fig. 2.3 A), we produced three additional ACP-tagged TrkA mutants to dissect their individual contributions to TrkA mobility. Namely, we generated: i) the Y499F/Y760F/Y794F mutant (recruitment mutant, RM in Fig. 2.6A); ii) the Y679F/Y683F/Y684F mutant (kinase mutant, KM in Fig. 2.6A); and iii) the TrkA-P791S mutant (ubiquitination mutant, Fig. 2.6A). The last one is modified in the binding site for the E3 Ubiquitin-ligase Nedd 4-2 [94] (see paragraph 1.3.4). First we biochemically validated *rTrkA*-K547N, RM, KM and *rTrkA*-P791S in comparison to *rTrkA*-wt for both phosphorylation and ubiquitination (see data in Paragraph 2.5), then we checked that all generated TrkA mutants are able to bind NGF (Fig. 2.6A, right panel), to a similar extent to TrkA-wt (see Fig. 2.1.B).

We then transfected RM, KM and TrkA-P791S in SHSY5Y cells, and the ACP tag of exposed receptors was biotinylated and labelled with Qdots for monitoring their membrane dynamics in resting condition. Quantification of the obtained trajectories led us to the conclusion that none of the compromised functions is responsible for TrkA-K547N altered dynamics. Indeed, the quantification of the modes of motion displayed by RM, KM, TrkA-P791S was almost superimposable to the one of TrkA-wt (Fig. 2.6 B). We compared also the density of labelled receptors at the cell surface of TrkA-wt, -K547N with RM, -KM and -P791S, finding that only TrkA-RM displayed a higher density of receptors with respect to the -wt, probably due to its double impairment of phosphorylation and ubiquitination activity; indeed, Y794, one of the residues mutated in RM, is located inside the PPXY binding sequence for Nedd 4-2 [94], [127] (Fig.2.6 C).

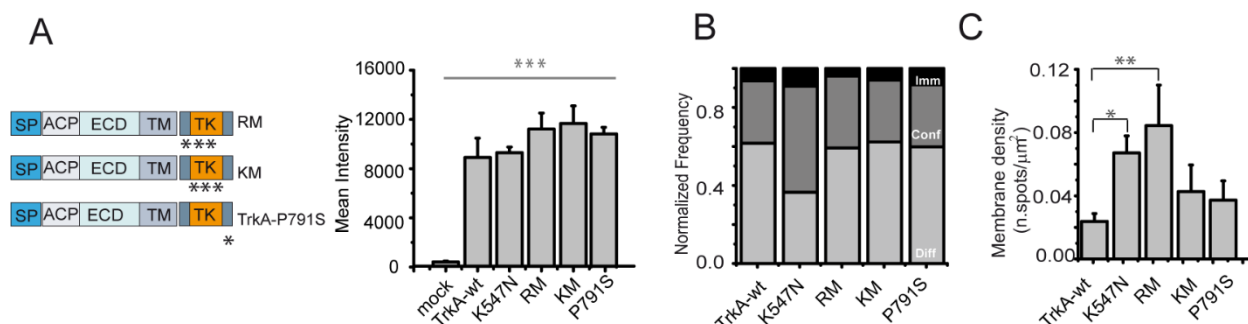


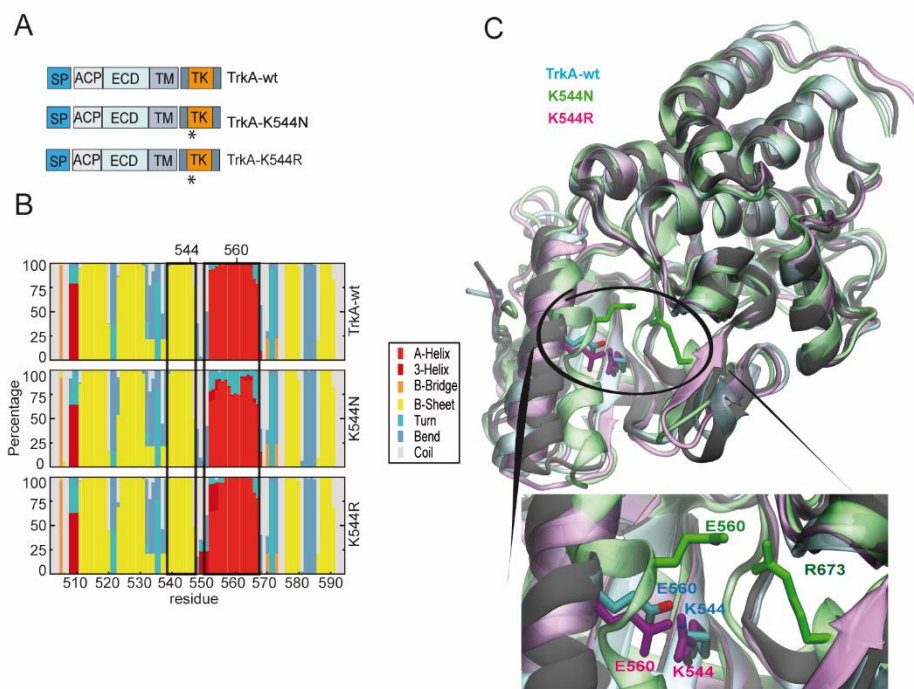
**Figure 2.6. A)** Scheme of RM, KM and ubiquitination mutant (TrkA-P791S); asterisks highlight the positions of the single mutations in the intracellular region (Y to F in RM and KM). Right: quantification of mean intensity±sem after incubation with Alexa647-labelled NGF, imaged at the surface of plasma membrane of SHSY5Y expressing TrkA-wt or its mutants, compared to the same signal in non-transfected cells. We measured a range of 16 to 25 cells pooled from two independent cover slips. \*\*\*p<0.001 according to one-way ANOVA with Bonferroni’s Multiple Comparison test. **B)** Stack-column histogram plot for diffusive (light grey), confined (grey), immobile (black) receptors obtained for TrkA mutants. The total population was normalized to 1 (RM: n=6638, KM: n=7777 and TrkA-P791S: n=1841 trajectories; TrkA-wt and TrkA-K547N of Fig. 2.3 A are reported here as a reference). All data are pools from a range of 13 to 19 different cells collected in three independent replicas. **C)** Quantification of density of labeled receptors per cell area (n=16 cells for RM, n=13 cells for KM, n=17 cells for P791S). TrkA-wt and TrkA-K547N of Fig. 1D are reported here as a reference. \*\*p<0.01, \*p<0.05 according to one-way ANOVA with Bonferroni’s Multiple Comparison test.

The results reported above allowed us to exclude that the impairment of one of the functions abolished in these mutants be responsible for the altered membrane density and dynamics displayed by TrkA-K547N.

Instead, as described in Paragraph 1.2.2, it is known that the mutated Lys we studied has a key structural role in the definition of a salt bridge that links strand β3, containing the Lys, to the αC helix, containing the Glu (563 in rat TrkA and 560 in *hTrkA*), within the N lobe of TKD [34], [41]. We thus hypothesized that the K→N mutation, which induce the substitution of a positive-charged residue (K) with a neutral one (N), leads to the break of the salt bridge and thus to structural rearrangement of the TrkA TKD; this, independently of the functional impairment, may account for the observed entrapment on the membrane. This prompted us to perform molecular dynamics simulations of the *hTrkA* kinase domain (PDB: 4f0i) in the wt configuration or after insertion

of K544N mutation. To corroborate our hypothesis we also simulated the behavior of another mutation, the *hTrkA*-K544R, in which the substitution of the Lys with another positive-charged residue, the Arg, possibly maintains the aforementioned salt bridge, while still compromising phosphorylation.

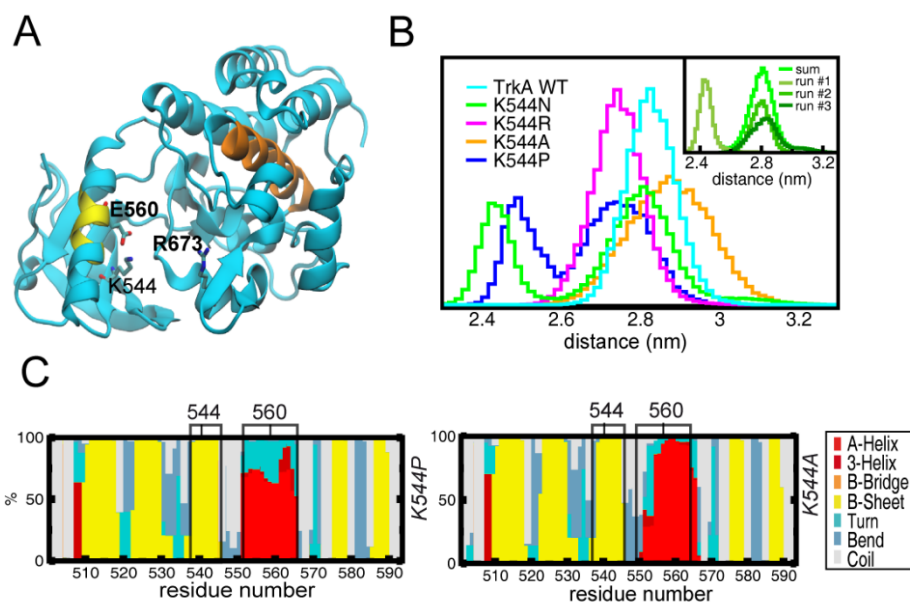
We focused on possible structural alterations induced by the K→N mutation. Surprisingly, the MD simulations, while predicting a limited impact on strand  $\beta 3$  (where the Lys residue is positioned), highlight a higher destabilization in the  $\alpha C$  helix (where the Glu that the Lys binds is located) (Fig.2.7 B,C). This leads to distinct sub-populations characterized by different positioning of the  $\alpha C$  helix with respect to strand  $\beta 3$  and C lobe, including one triggered by the formation of a new salt bridge between Glu560 in the  $\alpha C$  helix and Arg673, located between  $\beta 8$  and  $\beta 9$  (Figs. 2.7 C and 2.8).



**Figure 2.7 A) Structural changes of the TKD of human TrkA-K544N.** **A)** Scheme of human TrkA-wt, K544N and K544R mutants (K547N and K547R mutants respectively in the rat sequence); asterisks highlight the positions of the single mutations Y→F in the intracellular region. **B)** Molecular dynamics (MD) analysis of secondary structure elements encompassing residues 501 to 593 in *hTrkA*-wt (top), *hTrkA*-K544N (middle) and *hTrkA*-K544R (bottom). The regions corresponding to the  $\alpha C$  helix and the  $\beta 3$  sheet are highlighted by black rectangles. **C)** Selected snapshots from MD simulations of TrkA-wt TKD (cyan), and its K544N (green) and K544R (magenta) mutants, superimposed on the *human* TrkA-wt TKD crystal structure (PDB: 4f0i, gray).

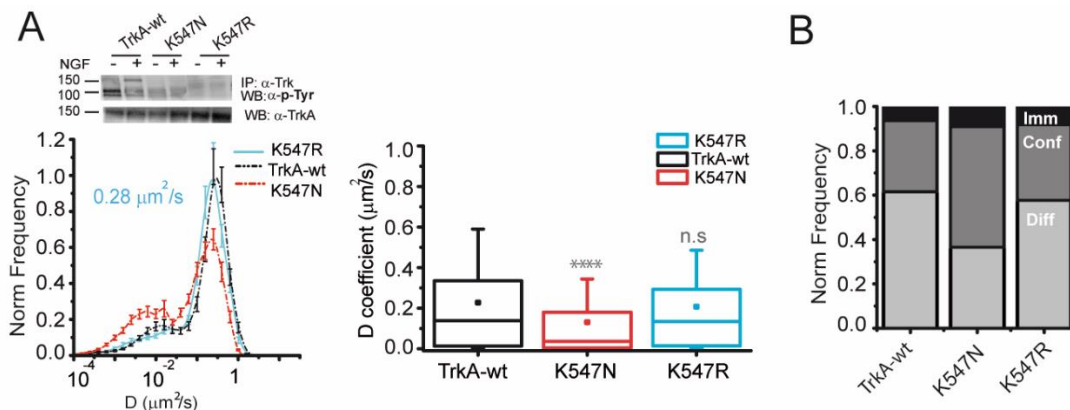
This effect is strictly dependent on the lack of Lys544-Glu560 salt bridge: indeed, substitution of Lys544 with salt-bridge preserving Arg (Fig. 2.8 A-B) maintains the stability of the  $\alpha C$  helix in the MD simulations (Fig. 2.7 C and

Fig. 2.8 B). Conversely, two different but both salt-bridge abolishing amino acids like Ala or Pro are predicted to destabilize the  $\alpha$ C helix (Fig. 2.8 C).



**Figure 2.8. A)** Crystal structure of *hTrkA* (4f0i, in cyan) and **B)** histogram plots of the distance between the region of the  $\alpha$ C helix containing Glu560/883 (a.a. 558-562 in *hTrkA*) and  $\alpha$ F helix in the C-lobe (a.a. 707-722 in *hTrkA*) during the combined MD simulations for the wt proteins and the indicated mutants: *hTrkA*-wt (cyan), *hTrkA*-K544N (green), *hTrkA*-K544R (magenta), *hTrkA*-K544A (orange) and *hTrkA*-K544P (blue) in panel. The inset in panel **B** shows the separate histograms for each of the three MD simulations performed for *hTrkA*-K544N in different shades of green, together with their sum (in light green). **C)** Secondary-structure stacked histograms of the N-lobe in the *hTrkA*-K544A and *hTrkA*-K544P mutants, derived from the MD simulations, reported for a comparison with Fig. 2.7 B.

To validate if the conservation of the salt bridge by *hTrkA*-K544R (in the simulations) matched to a membrane dynamics comparable to that of the *TrkA*-wt, we expressed and Qdot-labelled the new mutant ACP-tagged *TrkA*-K547R in SHSY5Y cells and found that, although this mutant is not phosphorylated, its membrane dynamics is more similar to that of *TrkA*-wt than to that of *TrkA*-K547N (Fig. 2.9 A,B).



**Figure 2.9. A)** Top left: WB showing Tyr phosphorylation in the absence (-) or presence (+) of 10 minutes stimulation with 125 ng/ml NGF, in SHSY5Y cells transfected with TrkA-wt, TrkA-K547N and TrkA-K547R constructs. Cell lysates were immunoprecipitated (IP) with anti-Trk (C-14) antibody, and subsequently blotted with anti p-Tyr antibody, stripped and re-blotted with anti-TrkA antibody. Bottom left: distribution of diffusion coefficient (D) for mobile TrkA-K547R (dark cyan curve, n=936) trajectories, compared with the same graph for TrkA-wt and -K547N. Right: Box-plot for D values retrieved from trajectories (at least 6 frames long) of TrkA-wt (red, n=1116) TrkA-K547N (green, n=2640) or TrkA-K547R (blue, n=1313) in SHSY5Y cells in resting conditions. Trajectories are pooled from three independent experiments. Boxes: 25<sup>th</sup>-75<sup>th</sup> percentiles; whiskers: 10<sup>th</sup>-90<sup>th</sup> percentile; line: median; square: mean. \*\*\*\*P<0.0001, n.s.: non-significant at the 0.05 level, according to Kruskal-Wallis test, with Dunn's means comparison. **B)** Stack-column histogram plot of diffusive (Light grey), confined (grey), immobile (black) receptors obtained for TrkA-K547R (1745 trajectories), TrkA-wt and TrkA-K547N (same data as Fig. 2.3 A).

To understand if the considered salt-bridge a conserved mechanism to maintain the fold of the ATP-binding pocket also in other RTKs, we performed MD simulations of the corresponding kinase inactive mutations K866N and K866R induced in the human sequence of VEGFR2 receptor (Fig. 2.10 A, B), obtaining similar results. Accordingly, the *m*VEGFR2-K866N mutation (corresponding to K868N in *human* VEGFR2), but not *m*VEGFR2-K866R, displayed reduced membrane mobility and increased membrane pool respect to VEGFR2-wt (Fig.2.10 C, D), when transfected in SHSY5Y and GM7373 cells. Given the high degree of conservation of this Lys residue in the ATP-binding pocket (Fig. 2.1 A, Paragraph 1.1.2 and [34]), our data hint at the existence of a general mechanism regulated by this specific residue.

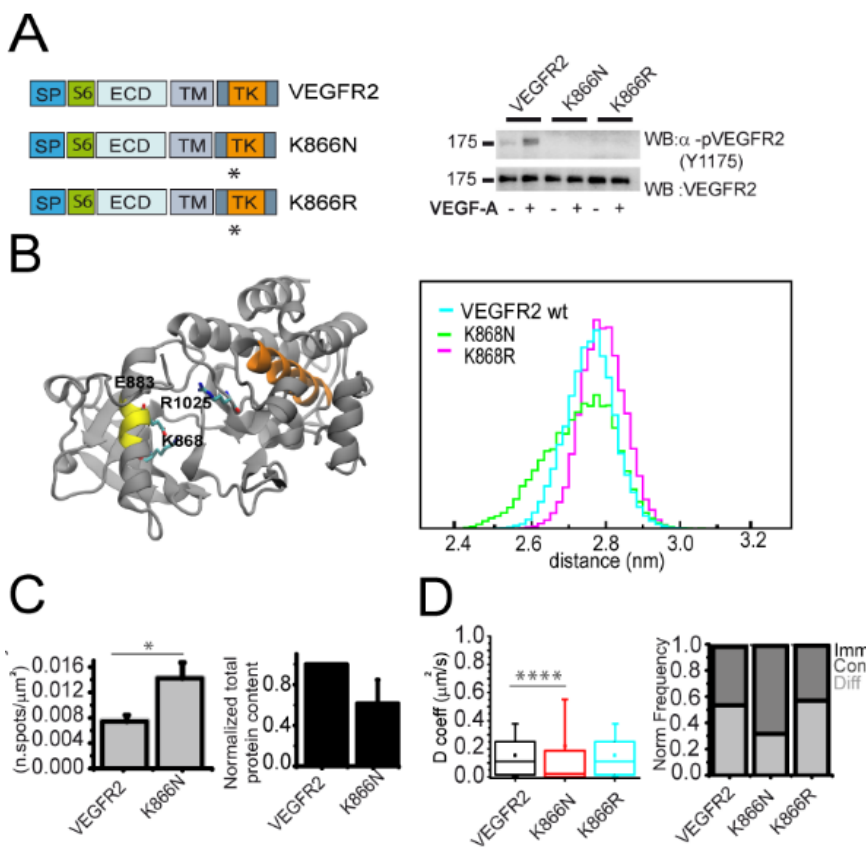


**Figure 2.10. A)** Scheme of VEGFR2-wt, K866N and K866R mutants; asterisks highlight the positions of the single mutations in the intracellular region. Right: western blot from cell extracts of GM7373-WT and GM7373-K866N shows phosphorylated VEGFR2 (p-VEGFR2; pTyr 1175) in the presence or absence of 5 minutes stimulation with 30 ng/ml of VEGF-A. Total VEGFR2 was reblotted as control. **B)** Crystal structure of *h*VEGFR2 (6gqq, in gray) highlighting in yellow the region of the  $\alpha$ C helix containing Glu883 and in orange the  $\alpha$ F helix. The image also shows the amino acids involved in the native salt-bridge (Lys866-Glu883 in VEGFR2) and the Arg residue (Arg1025 in VEGFR2) involved in the formation of the new salt-bridge during the MD simulations of K868N. Right: histogram plots of the distance between the region of the  $\alpha$ C helix containing Glu883 (a.a. 881-885 in VEGFR2) and  $\alpha$ F helix in the C-lobe (a.a. 1084-1099 in VEGFR2) during the MD simulations for the wt proteins and the indicated mutants: VEGFR2-wt (cyan), VEGFR2-K544N (green), VEGFR2-K544R (magenta). The distance is calculated between the centers of mass of the  $\alpha$ -carbons in each region. **C)** Membrane receptor density, quantified as number of Qdot-labelled moving spots visualized at TIRF per cell membrane area, for VEGFR2-wt (n=10 cells) and VEGFR2-K866N (n=12 cells) receptors. \*P<0.05 according to two-tailed Mann-Whitney

test. Right: densitometric analysis of total VEGFR2-wt and VEGFR2-K866N content obtained averaging two blots; the densitometric content of VEGFR2-K866N was normalized to that of the VEGFR2-wt. **D**) Box-plot for D values retrieved from trajectories (at least 6 frames long) of *m*VEGFR2-wt (red, n=291), *m*VEGFR2-K866N (red, n=384) and *m*VEGFR2-K866R (cyano, n=512) in SHSY5Y cells in resting conditions. Trajectories are pooled from three independent experiments. Boxes: 25<sup>th</sup>-75<sup>th</sup> percentiles; whiskers: 10<sup>th</sup>-90<sup>th</sup> percentile; line: median; square: mean. \*\*\*\*P<0.0001, according to Kruskal-Wallis test with Dunn's means comparison. Right: Fraction of receptors undergoing diffusive (light-grey), confined (grey), immobile (black) motion modes for VEGFR2-wt (n=10 cells, 355 trajectories), VEGFR2-K866N (n=12 cells, 597 trajectories) and VEGFR2-K547R (n=10 cells, 512 trajectories) in GM7373 cells in resting conditions. The total number of receptor spots (corresponding to n≥900 trajectories) was normalized to 1.

Here we demonstrated that at least in the simulations of two cases of RTKs, the substitution of the Lys in  $\beta$ 3-sheet with an Asn yields specific structural rearrangements, which could cause the consequent decrease in the measured diffusion. One possible explanation was that this modification could enhance an aggregation of the TKDs, which may then favor the formation of receptor homo-clusters. Indeed, TrkA crystal structure already showed the possibility to form dimers and probably oligomers in the crystal unit [208]. To test this hypothesis, we analyzed the intensity step-photobleaching profile in the membrane of fixed cells for Abberior635P-labelled *h*TrkA-wt, *h*TrkA-K544N and *h*TrkA-K544R (red boxes of Fig. 2.11 A; see paragraph 1.4.1.3). For each spot, we quantified the number of photobleaching steps as a direct measure of the number of molecules in an isolated spot [169]. The results highlight no significant changes in the monomer, dimer and oligomer populations amongst the three cases (Fig. 2.11 B), thus ruling out the possibility of increased homo-aggregation as the molecular cause for the observed TrkA-K547N membrane dynamics. We performed this analysis also after NGF administration, and observed for TrkA-wt a reduction of ~33.8 % of the monomeric fraction, corresponding to an increase by ~63% of dimeric and ~71.4% of oligomeric populations. On the contrary, both *h*TrkA-K544N and *-h*K544R did not display significant changes in their monomer-dimer-oligomer distribution after NGF stimulation with respect to the untreated conditions (Fig. 2.11 C). Since we previously demonstrated that TrkA-K547N binds NGF with similar extents of TrkA-wt (see Fig. 2.1B), the results plotted in Fig.11 C suggests that the binding of NGF to the extracellular portion of the receptor is not the only condition for its functional dimerization/oligomerization (see also Paragraph 1.2.2). Rather, as we did not observe changes in the two kinase inactive receptors, but a massive decrease in the frequency of monomers in TrkA-wt, we can speculate that the integrity of the TKD of TrkA monomers, together with the NGF binding, is fundamental to shift the balance from monomers to functional dimers/oligomers. Anyway, from these observations, we can state that at least two types of immobilization modes can be distinguished for TrkA at the cell surface. The first one is that displayed by TrkA-wt upon NGF binding (Fig. 2.3 A,C), which correlates with increased surface oligomerization; the other one is the one displayed by TrkA-K547N, which does not depend on an increased propensity of the mutated receptor to self-aggregate, nor on NGF binding (Fig. 2.3 A,B). A hypothesis could be that the structural rearrangement predicted for TrkA-K547N simulations could account for new hetero-interactions leading to the observed confinement and

immobilization at the cell surface detected by SPT. This hypothesis motivated the experiments reported in the following paragraph.

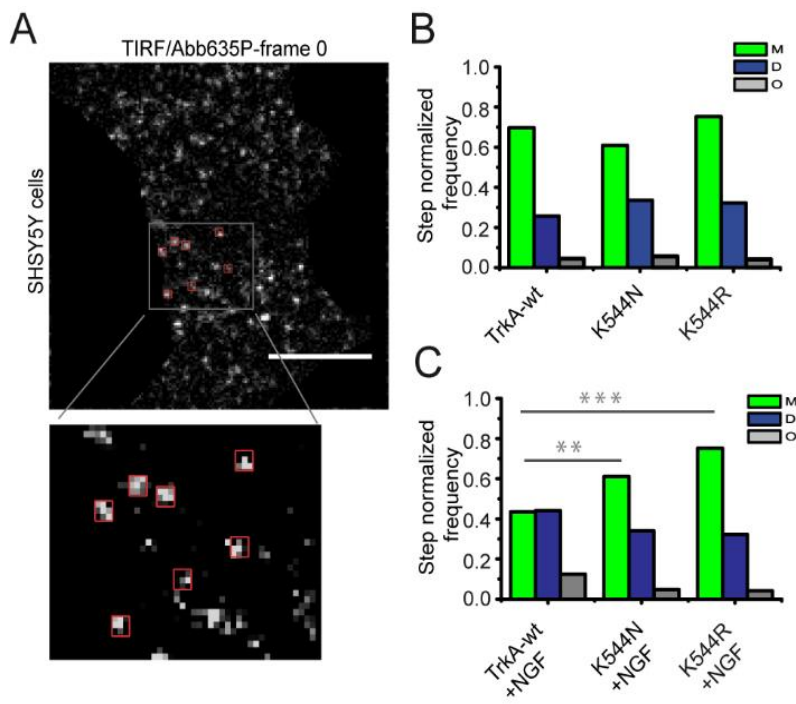


**Figure 2.11.** **A)** Representative TIRF image of Abberior635P-labelled *hTrkA* spots on the surface of fixed SHSY5Y cells: red squares in the inset are the 3×3 pixels ROI highlighting the analyzed spots in the first frame of the background-subtracted TIRF movie. **B)** Photobleaching steps per track counted for *hTrkA*-wt (n=245 spots), *hTrkA-K544N* (n=286 spots) and *hTrkA-K544R* (n=355 spots); differences are not significant according to  $\chi^2$  test. **C)** Photobleaching steps per track counted after 15 minutes of NGF stimulation for *hTrkA*-wt (n=177 spots), *hTrkA-K544N* (n=188 spots) and *hTrkA-K544R* (n=124 spots). \*\* p<0.01, \*\*\*p<0.001 according to  $\chi^2$  test among *hTrkA*-wt and *hTrkA-K544N* or *hTrkA-K544R*; \*\*\*\*p<0.0001 according to  $\chi^2$  test among *hTrkA*-wt before (B) and after (C) NGF stimulation; all the other comparisons are not significantly different. All data are pools from 10 cells collected in two independent replicas. All data are pools from 10 cells collected in three (B) and two (C) independent replicas.

## 2.4 TRKA-K547N MEMBRANE MOBILITY DEPENDS ON THE INTEGRITY OF CORTICAL ACTIN

It is well known that the lateral diffusivity of membrane proteins and lipids is modulated by the presence of specialized physical barriers [209] like actin fences [210]. These fibers, lying in close contact with the inner leaflet of the plasma membrane, can constrain transmembrane proteins within transient confinement regions called corrals [211], which confine in space and time the diffusivity of transmembrane receptors [11], [212]. We investigated if the altered membrane mobility of TrkA-K547N could be due to new interactions with any of these structures. For this purpose, we treated cells with drugs affecting the polymerization state of actin, either by disrupting (cytochalasin D, latrunculin B) or by stabilizing (jasplakinolide) actin fibers integrity, as tested by phalloidin staining of the cells after the treatment (Fig. 2.12).

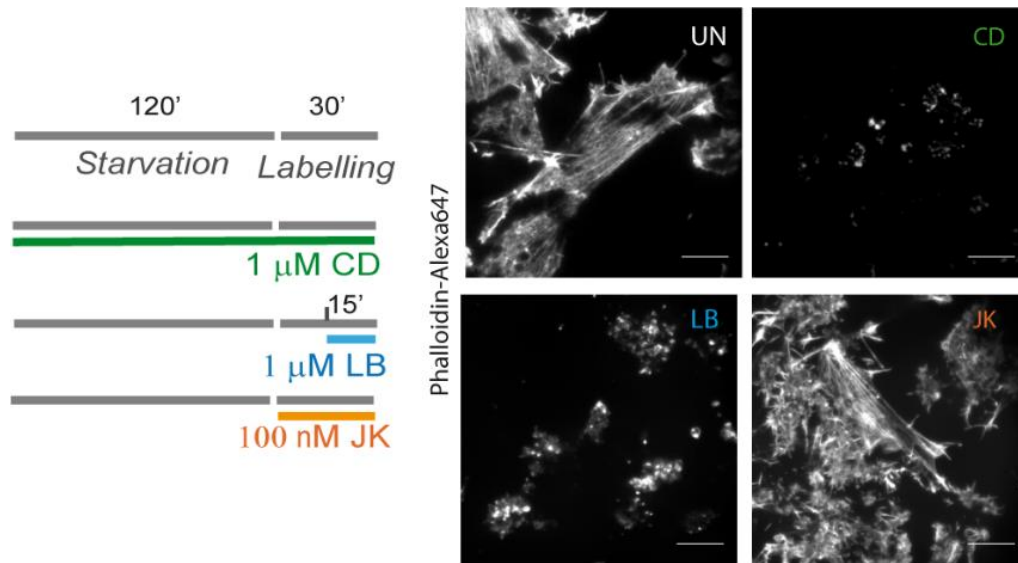


**Figure 2.12.** Left: Timeline of the experiments on TrkA-K547N and TrkA-wt in the presence of drugs affecting actin polymerization. CD: Cytochalasin D; LB: Latrunculin B; JK: Jasplakinolide; right: typical TIRF images of SHSY5Y cells labelled with Alexa647-phalloidin after the treatments (UN: untreated). Scale bar: 10  $\mu\text{m}$ .

SPT measurements in these conditions (see Appendix B for details) demonstrated that the TrkA-K547N confined and immobile modes of motion were substantially impaired by actin depolymerization (Fig. 2.13 B), and so was the accumulation of surface TrkA-K547N receptors (Fig. 2.13 A,C,D). On the contrary, these turned out to slightly increase when we stabilized the polymerized form of actin fibers (Fig. 2.13 A,C). The same treatments tested on TrkA-wt showed an opposite trend in the modes of motion after actin depolymerization (Fig. 2.13 D), and no significant effect on the density of surface receptors (Fig. 2.13 E). These data suggest that TrkA-K547N, but not TrkA-wt, is either stably entrapped within membrane regions maintained by the actin meshwork, or directly interacts with it, justifying the specific slow membrane dynamics and the surface accumulation displayed by this mutant.

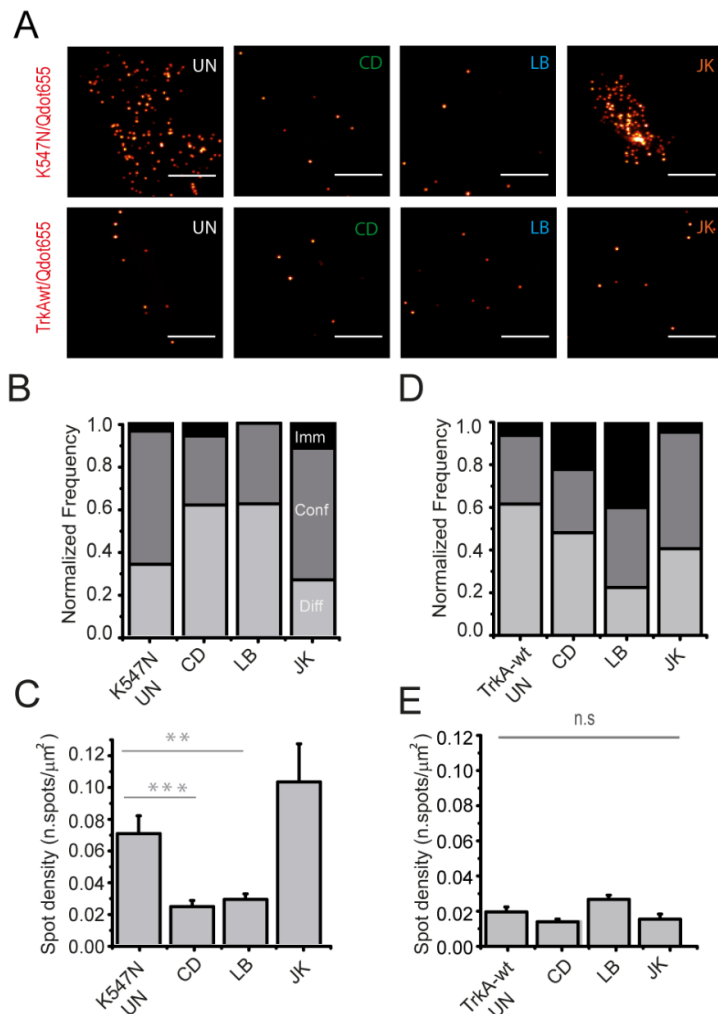


**Figure 2.13. Actin cytoskeleton mediates membrane immobilization and accumulation of TrkA-K547N.** **A)** Representative TIRF images of TrkA-K547N (top) and TrkA-wt (bottom) transfected SHSY5Y cells after Qdot labeling, in untreated and CD-, LB- and JK- treated conditions. Scale bar=10  $\mu$ m. **B)** Stack-column histogram plot for the distribution of diffusive (light grey), confined (grey) and immobile (black) TrkA-K547N receptors in untreated conditions and after CD, LB, JK treatments (CD, n=904; LB, n=366; JK, n=1606 trajectories). **C)** TrkA-K547N surface density in untreated conditions and after CD, LB, JK treatments (untreated, n=22; CD, 15; LB, 17; JK, 23 cells). \*\*\*p<0.001, \*\*p <0.01 according to Kruskal-Wallis test followed by Dunn's Multiple Comparison test. **D)** Stack-column histogram plot for the distribution of diffusive (light grey), confined (grey) and immobile (black) TrkA-wt receptors in resting conditions and in the presence of CD, LB, JK drugs (CD: n=169; LB: n= 169; JK: n=100 trajectories). **E)** TrkA-wt surface density in untreated conditions and after CD, LB, JK treatments (untreated, n=10 cells; CD, 7 cells; LB, 8 cells; JK, 6 cells). Differences are not significant according to Kruskal-Wallis test. Data in B) and C), and in D) and E), derive from the same experiments.

## 2.5 ROLE OF TRKA POST-TRANSLATIONAL MODIFICATIONS ON NGF-INDUCED MEMBRANE-RELATED DYNAMICS AND FUNCTIONS

From the data reported in Fig. 2.3, we concluded that both TrkA-wt and TrkA-K547N change membrane mobility upon NGF stimulation, albeit with very different responses in the two cases. We thus aimed at understanding if the TrkA-K547N functional or structural features (as described in Fig. 2.6) are responsible for this change. Biochemical analysis of *r*TrkA-K547N, RM, KM and *r*TrkA-P791S in comparison to *r*TrkA-wt revealed that NGF-induced phosphorylation and ubiquitination could be fully dissected by using these mutants. Accordingly, we first tested all these constructs for phosphorylation and ubiquitination in the absence and presence of a 10 minutes NGF stimulation (Fig. 2.14 A-C). As expected, only TrkA-wt and TrkA-P791S showed a significant

phosphorylation signal (Fig. 2.14 B). Conversely, the two kinase-inactive mutants (TrkA-K547N and KM), as well as RM, were not significantly phosphorylated in response to NGF (Fig. 2.14 A). Also, we observed a significant NGF-dependent increase of ubiquitination for TrkA-wt but not for RM and TrkA-P791S, in line with their mutations (Y794F and P791S, respectively) being positioned in the PPXY binding motif for Nedd 4-2 ubiquitin ligase [127]. Surprisingly, we found a significant ubiquitination signal also for TrkA-K547N but not for KM, although both are kinase-inactive mutants (Fig. 2.14 A) in SHSY5Y cells. It was previously reported that Lys 547 mutation to Arg leads to impairment of TrkA ubiquitination in HEK293 cells in the absence of NGF [94]. However, we found that in this cell line ubiquitination is sensitive to the residue which substitutes Lys 547. In detail, the K547R mutation abolishes TrkA ubiquitination as previously reported [94], but this is regardless of NGF addition (Fig. 2.14 B). Indeed, in this cell line TrkA-wt is almost equally ubiquitinated in resting and NGF-stimulated conditions, which may be due to a higher expression level of the constructs than in SHSY5Y cells, leading to ligand-independent auto-activation. In any case, TrkA-K547N mutant displays a higher ubiquitination signal than TrkA-K547R in this cell model, confirming the unique properties of this kinase-inactive mutant (Fig. 2.14 B). Overall, analysis of the ubiquitination pattern of different TrkA constructs highlighted that TrkA kinase activity is not a necessary requisite for NGF-dependent ubiquitination by Nedd 4-2, at least as far as the TrkA-K547N case is concerned. Moreover, despite a comparable ubiquitination signal between TrkA-K547N and -wt, they displayed different kinetics of internalization after NGF stimulation (as shown in Fig.2.5 A,B): TrkA-wt, correctly phosphorylated and ubiquitinated after ligand stimulation, is rapidly internalized; contrariwise, the absence of kinase activity of TrkA-K547N delays this process, indicating that a synergic cooperation between the two PMTs may be necessary to ensure the correct timing of receptor internalization.

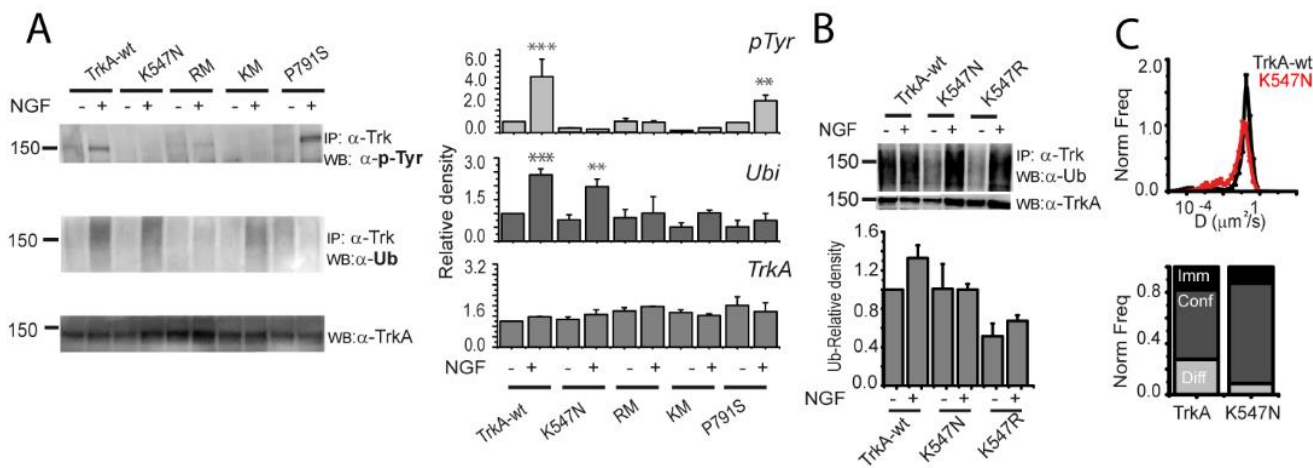


**Figure 2.14. Impact of post-translational modifications on NGF-induced TrkA membrane dynamics.** **A)** WB showing Tyr phosphorylation (p-Tyr, top) and ubiquitination (Ub, middle) levels of Trk in SHSY5Y cells transfected with TrkA-wt, TrkA-K547N, RM, KM and TrkA-P791S in the presence (+) or absence (-) of 10 minutes stimulation with 125 ng/ml NGF, after immunoprecipitation (IP) with anti-Trk antibody. The relative density of the bands is reported on the right of each blot, as mean±sem of 2-5 independent replicas; each band density was

normalized to the total TrkA content obtained after membrane stripping, and divided for TrkA-wt value (p-Tyr Blot: n=3 for all constructs; Ub blot: n=5, TrkA-wt; n=4, rTrkA-K547N; n=2, RM; n=3, KM, TrkA-P791S n=2). \*\*\*p<0.001, \*\*p<0.01, according to one-way Anova with Bonferroni's multiple comparison test. Bottom: WB showing total TrkA levels for the same samples as above. The relative density of the bands is reported on the right of the blot, as mean±sem of 3 independent replicas; the band density was normalized to the total protein content of each lane and divided for TrkA-wt value. Data are not significantly different according to one-way Anova with Bonferroni's multiple comparison test. **B)** WB showing total ubiquitination levels in the absence (-) or presence (+) of 10 minutes stimulation with 125 ng/ml NGF, in HEK293T cells transfected with TrkA-wt, TrkA-K547N and TrkA-K547R constructs. Cell lysates were immunoprecipitated (IP) with anti-Trk (C-14) antibody, and subsequently blotted with P4D1 antibody recognizing both mono- and poly- ubiquitin, stripped and re-blotted with anti-TrkA antibody. Below: relative density of the bands is reported as mean±sem of 2 independent replicas; each band density was normalized to the total TrkA content obtained after membrane stripping, and divided for the TrkA-wt value. **C)** Above : distribution of diffusion coefficient (D) for mobile TrkA-wt (black curve, n=11 cells, 924 trajectories) and TrkA-K547N (red curve, n=15 cells, 2407 trajectories) trajectories in HEK293 cells. Below: stack-column histogram plot for the fraction of diffusive (light-grey), confined (grey), immobile (black) receptors obtained in the same experiments.

We then evaluated the NGF effect on the membrane mobility of mutants that cannot be phosphorylated but are ubiquitinated (TrkA-K547N), cannot be phosphorylated nor ubiquitinated (RM, KM) and cannot be ubiquitinated but are phosphorylated (TrkA-P791S). In addition, TrkA-K547N was the only mutant in the group displaying the breakage of the Lys-Glu salt bridge correlated to its slow membrane dynamics (Fig. 2.6).

From analysis of the distributions of D coefficients of RM, KM, TrkA-P791S mutants before and after the NGF treatments, it appears clear that neither of these mutants shows the same dynamic response to NGF of TrkA-wt (Fig 2.15 A,B,C), rather, they all share the lack of NGF-induced immobilization of TrkA-K547N (Fig 2.3 D,B). The small shift in the fast diffusion peaks observed especially for RM and TrkA-P791S is compatible with NGF inducing their dimerization [169]. To assess if this hypothesis is true, single-step photobleaching analysis could be performed in the future, as already shown in Fig. 2.11. Similarly, it will be interesting to study why this small shift is not visible for KM (Fig 2.15 B) mutant after NGF administration. From the SPT analysis for RM, KM and TrkA-P791S we calculated the variation of the modes of motion of all constructs after NGF stimulation. Interestingly, we found that all TrkA mutants investigated display weaker NGF-induced immobilization than TrkA-wt (Fig. 15 D), meaning that this effect conceivably requires both unaltered phosphorylation and ubiquitination to occur. Interestingly, the weaker NGF-induced immobilization displayed by all these mutants could likely mean that the robust and signaling-related immobilization of the wt receptor conceivably requires both unaltered phosphorylation and ubiquitination to occur (Fig 2.15 D). While the role of phosphorylation could be expected in light of previous works on the EGFR receptor [163], the behavior of TrkA-P791S suggests an unprecedented fundamental role also for the ubiquitination process in the regulation of TrkA lateral mobility. It is established that the typical slowdown displayed by TrkA-wt, which is correctly phosphorylated and ubiquitinated in response to NGF, can be ascribed to the steps preceding receptor internalization, as for example the recruitment of receptors in clathrin-coated vesicle precursors or caveolae [162]. Accordingly, it is possible to speculate that the weaker NGF-induced immobilization of TrkA-P791S could be due to lower access of this mutant to regions destined for the internalization, due to the lack of ubiquitination. Furthermore, this data highlights also that

membrane immobilization is not a prerequisite for TrkA activation; indeed TrkA-P791S, which is correctly phosphorylated, does not slowdown in response to NGF.

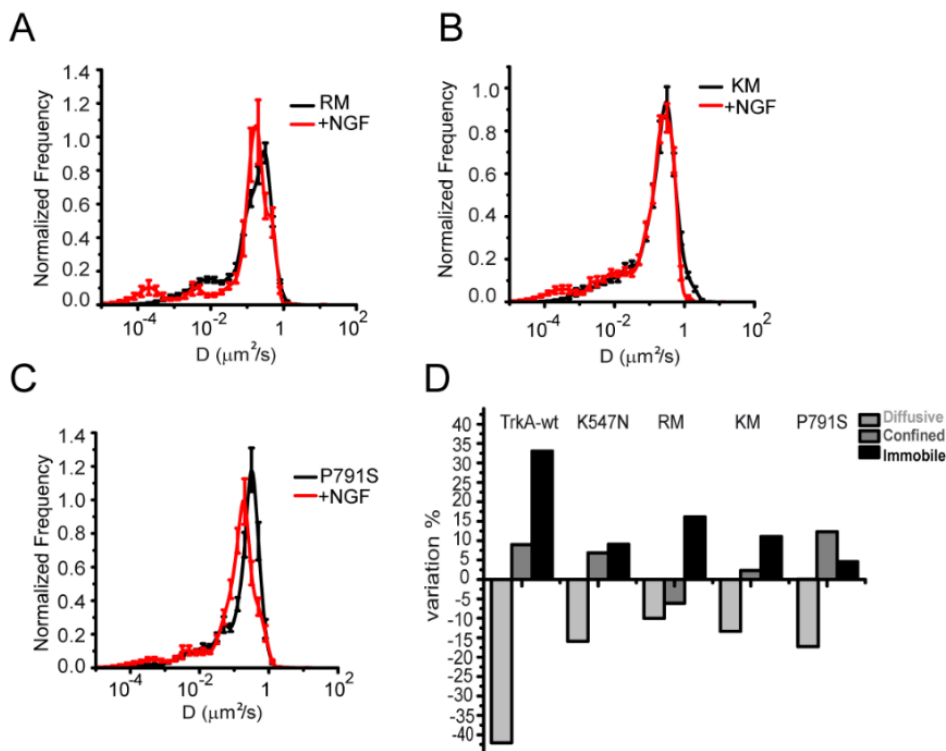


**Figure 2.15.** **A)** Distribution of diffusion coefficient (D) for mobile TrkA-RM before (black curve, n= 16 cells, 2263 trajectories) and after NGF administration (red curve, n= 10 cells, 315 trajectories) in SHSY5Y cells. **B)** Distribution of diffusion coefficient (D) for mobile TrkA-KM before (black curve, n= 13 cells, 1261 trajectories) and after NGF administration (red curve, n= 12 cells, 521 trajectories) in SHSY5Y cells. **C)** Distribution of diffusion coefficient (D) for mobile TrkA-P791S before (black curve, n= 17 cells, 935 trajectories) and after NGF administration (red curve, n=12 cells, 803 trajectories) in SHSY5Y cells. **D)** Column plot of the variation (in percentage of the total) of diffusive (light-grey), confined (grey), immobile (black) receptor populations upon NGF stimulation for TrkA-wt (n=513), TrkA-K547N (n=2909), RM (n=531), KM (n=1848) and TrkA-P791S (n=1526

trajectories); the number of trajectories analyzed in resting conditions for each mutant are reported in Fig. 2.6 B. All trajectories are pools of a range of 10-21 cells from three independent replicas.

As a matter of fact, ubiquitination of TrkA mediated by Nedd 4-2 is indeed reported to regulate several NGF-TrkA functions such as differentiation and nociception both *in vitro* and *in vivo* [94], [135], [206]. Recently a deubiquitinating enzyme, USP63, was discovered, which de-ubiquitinates indirectly the receptor, competing with Nedd 4-2 for the binding of TrkA. USP36 depletion increases TrkA-Nedd4-2 complex formation, while USP36 expression disrupts this complex, inducing an enhancement or impairment of Nedd4-2-dependent TrkA ubiquitination, respectively [213]. It was demonstrated that in absence of USP36, the expression of TrkA membrane pool increases enhancing NGF-mediated TrkA activation and so PC12 cell differentiation [213].

These data prompted us to evaluate the differentiation induced by transient transfection with TrkA-P791S (compared to -wt in PC12 nnr-5 and PC12 Crispr- Cas9 edited for TrkA knockout (Fig. 2.16 B)). Here we evaluated the rate of cell differentiation in 48 hours measuring two morphological parameters: i) the ratio of differentiated cells on GFP-positive cells (*i.e.* TrkA expressing cells), estimated as cells with a neurite with a length greater than the diameter of the cell body and ii) the average length of neurites found in differentiated PC12 cells (Fig. 2.16).

In agreement to what affirmed by Anta *et al.* [213], we found that the absence of ubiquitination, displayed by TrkA-P791S, does not cause an increased ability to induce differentiation after 48 hours of NGF treatment; rather, we observed a slightly decrease in percentage of differentiation and average length of neurite measured (Fig. 2.16).

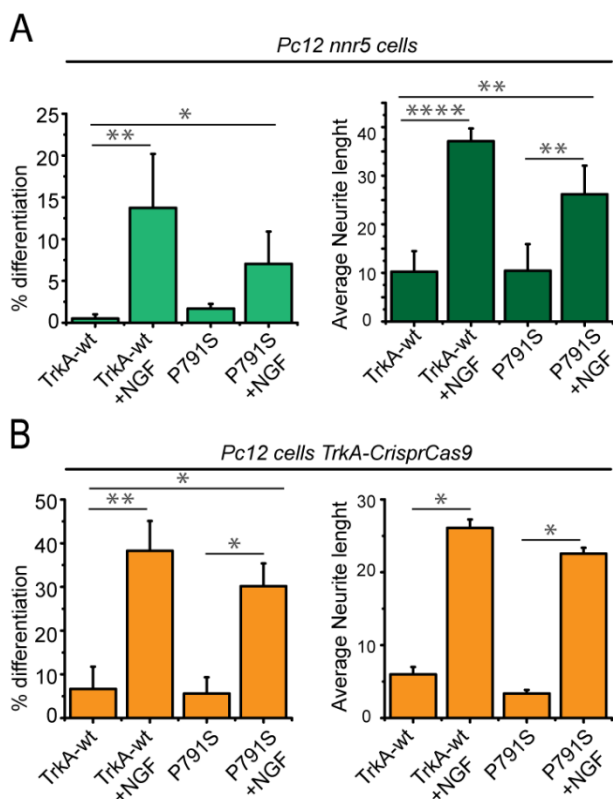


**Figure 2.16. A)** Left: percentage of differentiation quantified from PC12-nnr5 cells transfected with TrkA-wt and -P791S in absence or after 48 hours of stimulation with 125 ng/ml NGF; % of differentiation is obtained counting the number of cells with at least a neurite longer than the cell body diameter and dividing it for the total TrkA-positive cells. \*\* $p < 0.01$ , \* $p < 0.05$  according to one-way ANOVA with Bonferroni Multiple Comparison test. Right: average length of neurite measured in differentiated cells; data obtained from the analysis of ten fields from two independent experimental replicates (n TrkA-wt= 742 cells, n TrkA-wt<sub>NGF</sub>= 803 cells, n P791S= 962 cells, n P791S<sub>NGF</sub>= 837 cells. \*\*\*\* $p < 0.0001$ , \*\* $p < 0.01$  according to one-way ANOVA with Bonferroni Multiple Comparison test. **B)** Left: percentage of differentiation quantified from PC12-Crispr-Cas9 cells, edited for TrkA knockout (reported in the figure as “PC12 cell TrkA-Crispr Cas9”) transfected with TrkA-wt and -P791S in absence or after 48 hours of stimulation with 125 ng/ml NGF; % of differentiation is obtained as mentioned above. \*\* $p < 0.01$ , \* $p < 0.05$  according to one-way ANOVA with Bonferroni Multiple Comparison test. Right: average length of neurite measured in differentiated cells; \* $p < 0.05$  according to one-way ANOVA with Bonferroni Multiple Comparison test. Data obtained from ten analyzed fields from one experimental replicate (n TrkA-wt= 702 cells, n TrkA-wt<sub>NGF</sub>= 1021 cells, n P791S= 472 cells, n P791S<sub>NGF</sub>= 551 cells).

## 2.6 CONCLUDING REMARKS

Thanks to the use of a combined approach of SPT and biochemical techniques, in this work I was able to unveil that selected mutations in the TKD and NGF stimulation can lead to two similar, but substantially different TrkA membrane immobilization modes. On one hand, K544N mutation in sheet  $\beta 3$  of *hTrkA* TKD, responsible for the impairment of ATP allocation necessary to TKD activation and downstream phosphorylation processes [214], endows the receptor with increased confined and immobile membrane fractions, independently of NGF binding, and with an enrichment of surface pool. The importance of these observations is strengthened by evidence that another RTK, VEGFR2, shares similar features upon mutation of the corresponding Lys to Asn. MD simulations indicate that, in *hTrkA*-K544N, the  $\alpha C$  helix of the N lobe becomes less stable as a consequence of the loss of a salt bridge with  $\beta 3$  sheet, adopting different arrangements with respect to the C lobe (Fig. 2.6 C,B; Fig. 2.7 A,B).

On the contrary, *rTrkA*-K547R<sup>1</sup>, a kinase-inactive mutant that maintains the salt bridge, does not display the same repositioning and altered modes of motion with respect to *rTrkA*-wt. We also demonstrate that *rTrkA*-K547N membrane dynamics is not due to an increased propensity of the receptor to self-aggregate (Fig. 2.10), but rather could be explained by new hetero-interactions with actin cytoskeleton (Fig. 2.12 A,B,C) leading to the observed confinement and immobilization at the cell surface detected by SPT.

On the other hand, a different membrane immobilization is experienced by TrkA after NGF stimulation, with D and L distributions changing considerably in the wt but not in the K547N case. Surprisingly we observed that all TrkA mutants assessed by SPT (included the one with impaired ubiquitination) show an impairment of this NGF-induced membrane immobilization, despite their conserved ability to bind NGF. Thus, both NGF-induced TrkA phosphorylation and ubiquitination account for it. Probably the shared tendency of all analyzed mutants to undergo only small reductions of diffusivity may simply be due to NGF binding to their ECD (Fig. 2.13), that in turn could induce their dimerization, but not the typical signaling-related immobilization. In any case, a second important conclusion that can be drawn by this study is that, since inhibition of TrkA ubiquitination by the P791S mutation, without perturbing kinase activity, is sufficient to impair NGF-induced immobilization of TrkA-wt, this PTM likely plays a crucial role in the regulation of its membrane trafficking. Accordingly, the abolishment of ubiquitination also slightly reduces the capability to induce differentiation in PC12-nnr5 cells (Fig. 2.14). Future investigations will be required in order to understand if the impaired differentiation is due to a compromised NGF-dependent immobilization or to an absence of ubiquitination, or to both. Finally, our data also suggest that understanding the effect of a TKD mutation may benefit from the analysis of its impact on the KD structure, in addition to its catalytic activity. This may be useful to understand the molecular basis of pathogenicity of the several inactivating mutations disseminated along TrkA, and more in general RTKs, sequence.

---

<sup>1</sup> Note that, throughout the text, *rTrkA* is simply called TrkA, and *hTrkA* was used when referring to the human receptor.

# 3. THE HSAN IV RELATED TRKA-R649W MUTANT: EVIDENCE FOR DELAYED DEGRADATION AND CYTOSOLIC ACCUMULATION OF AUTOPHAGOSOMAL VESICLES

---

## 3.1 BACKGROUND AND RATIONALE OF THE WORK

The study of K544N mutation on hTrkA, described in chapter 2, allowed us to set a combined, multidisciplinary workflow that could be in principle used for investigation of any mutation in a receptor. In this chapter, I report similar experiments that I performed for the kinase-inactivating mutation TrkA-R649W (numeration referred to mouse sequence, corresponding to *hR643W*, see Table 1.1 and paragraph 1.2.5). This mutation is responsible for the onset of the hereditary and sensory Neuropathy type 4 (HSAN IV), a recessive autosomal disease characterized by anhidrosis and insensibility to pain, and due to the impairment of nociceptive neuron development [215]. As widely described in paragraph 1.2.5, more than 105 mutations spread in the NTRK1 gene, encoding for TrkA receptor, are found related to the onset of this disease, most of them being kinase-inactivating [14]. TrkA-R649W is a missense mutation positioned in the coding region for the catalytic loop (residues 642-649), in particular in the HRD domain [216]. As mentioned in paragraph 1.1.2, this aspect is very important because the HRD domain is conserved among RTKs; indeed, a residue equivalent to R649 is located in the catalytic loop of the insulin receptor [217], [218]. In particular, it was reported that this mutated Arg has an important role because its substitution with a Trp residue causes the loss of the positive charge necessary for the coordination with phosphorylated Tyr residues of the A-loop; moreover it is also placed before the Asp544 residue, which acts as catalytic base [219]. It was previously reported that the mutated protein, although correctly translocated at the plasma membrane, was not phosphorylated upon NGF stimulation; equally, *hTrkA-R643W* mutant transfected in PC12-nnr5 cells was not able to induce differentiation [220]. Currently, the pathological mechanisms through which HSAN IV mutations act are still unknown and for these reasons a large number of works focusing on their characterization (see paragraph 1.2.5) have been published. Here we have characterized the TrkA-R649W mutant, focusing in particular on its membrane expression, internalization rate, ubiquitination and kinetics of degradation.

This chapter presents the results of a collaboration with the Bio@SNS group of prof. Antonino Cattaneo (Scuola Normale Superiore, Pisa). Experiments here reported were performed and analyzed by Rosy Amodeo. The S6-TrkA-R649W constructs in pcDNA3 plasmid and in lentiviral pTRE vector were prepared by Giovanna Testa (Bio@SNS, Pisa). DRG extraction was made with the help of Domenica Convertino (CNI@NEST, Pisa). Single Molecule Internalization assay was performed with the help of Lorenzo Ceccarelli (CNI@NEST, Pisa). Acquisitions of AVs at the confocal microscope were made by Gianmarco Ferri (NEST, Pisa).

### 3.2 MEMBRANE AND INTRACELLULAR TRAFFICKING OF TRKA-R643W IN DRG NEURONS

As already mentioned in paragraph 1.2, the TrkA receptor is highly expressed at the cell surface of sensory neurons of the dorsal root ganglia (DRG), where it regulates, through NGF binding, neuronal development and survival at PNS; this makes evident why DRG neurons represent one of the best model to study TrkA pathological mutations in *in-vitro* cultures. For the experiment, we extracted, dissociated and cultured DRG neurons from mice at post-natal day 3 (day 0 in Fig. 3.1); the day after, cultured neurons were transduced with S6TrkA-wt and -R649W; 48 hours later the transgene expression was induced adding 1  $\mu\text{g}/\text{ml}$  of doxycycline to the cell medium [168]. At day 4, neurons were starved for 1 hour, treated or not with 125 ng/ml of NGF, and then the TrkA membrane pool was labelled with Qdot655 [221]. Cells were fixed, immunostained with anti-TrkA antibody and finally stained with Alexa488-secondary antibody before the imaging step at TIRFm (Fig. 3.1). We finally measured the signal of Qdot labelled receptors (corresponding to the membrane signal) versus the signal of Alexa 488 (corresponding to the total TrkA) inside each neuron, in order to evaluate differences in the membrane expression of TrkA-R649W and -wt.

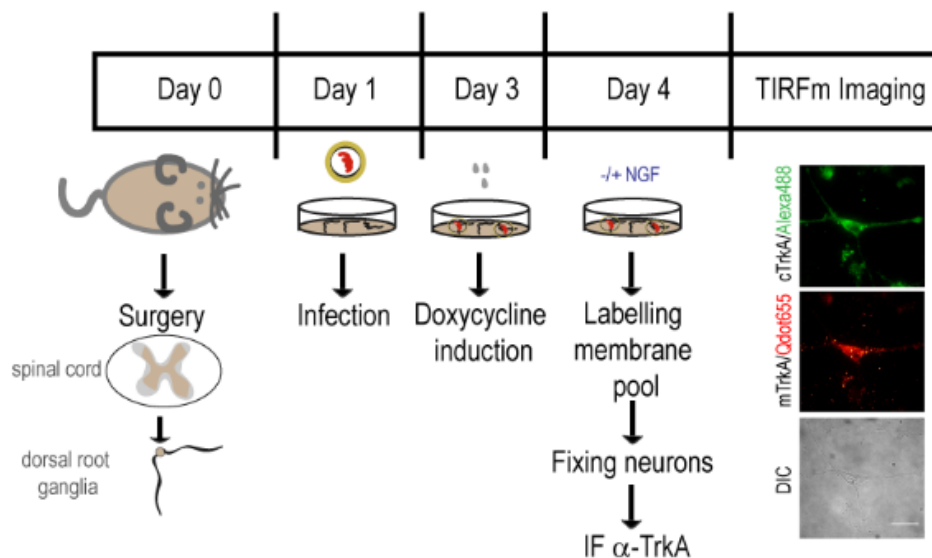


**Figure 3.1. Schematic of the experimental procedure for the detection of the membrane pool of TrkA.** At day 0, post-natal day 3 mice are sacrificed, and DRG neurons are extracted with surgery from the dorsal part of the spinal cord and seeded on a plate (see paragraph 4.2). At day 1, seeded DRG neurons are infected with lentiviral particles bearing S6-tagged TrkA-R649W or TrkA-wt transgenes. After 48 hours of integration (day 3) the transgene expression is induced with doxycycline administration. At day 4, after 1 hour of starvation, TrkA receptors are labelled with Qdots [168], fixed with 4% PFA and then immunostained against TrkA. After this step, DRG neurons are ready to be visualized at TIRFm. Scale bar: 20  $\mu\text{m}$ .

Interestingly we found that, in the absence of ligand stimulation, TrkA-R649W is more abundant at neuronal surface than the -wt counterpart when analyzing together cell somas and growth cones (GC), *e.g.* the motile structures positioned at the tips of the growing neurites. It must be noted however, that DRG neurons contain high levels of endogenous TrkA, which could have a not negligible role. For this reason, in order to validate the peculiar TrkA-R649W membrane expression in resting conditions, we transfected both TrkA-wt and -R649W in SHSY5Y cells (Fig. 3.2 B), a cell line insensitive to NGF stimulation for the lack of endogenous TrkA in plasma membrane [222]. We labelled the membrane pool of both constructs with Qdots and measured their membrane density (reported in number of spots per  $\mu\text{m}^2$ , as previously shown in Fig. 2.4), obtaining again an increased membrane density of TrkA-R649W, as in DRG neurons. This suggests that the signaling impairment responsible for the loss of sensory innervation, typical of the disease, is not ascribable to receptor downregulation at the cell surface (Fig. 3.2 A). Furthermore, the behavior of TrkA-R649W and -wt upon 1h of NGF stimulation displayed different features (Fig. 3.2 A,C). We did not observe a significant reduction of the membrane pool in the whole cell for TrkA-wt after NGF stimulation (Fig. 3.2 A). We hypothesize that this can be explained by: i) faster TrkA recycling, aimed at increasing NGF uptake from the extracellular environment during neuron development; ii) slower internalization rate of TrkA-NGF complexes, necessary to prepare the functional machinery for axonal growth. On the contrary, the higher number of TrkA-R649W exposed at plasma membrane displays a substantial decrease after NGF stimulation (Fig. 3.2 A). The same measure carried out at the GC (see rectangles highlighted in purple in Fig. 3.2 C, right panel) confirmed no marked differences in membrane density before and after NGF administration for TrkA-wt (Fig. 3.2 C). On the other hand, DRG neurons expressing TrkA-R649W showed an even more abrupt reduction of receptors at the surface of growth cones upon NGF administration. This aspect confirms that the R649W mutation is responsible for alterations of the membrane trafficking (possibly, an inhibition of the recycling pathway), and that the differences with the *wt* counterpart are more noticeable at the growth cones, where the internalization of TrkA-NGF complexes is more important.

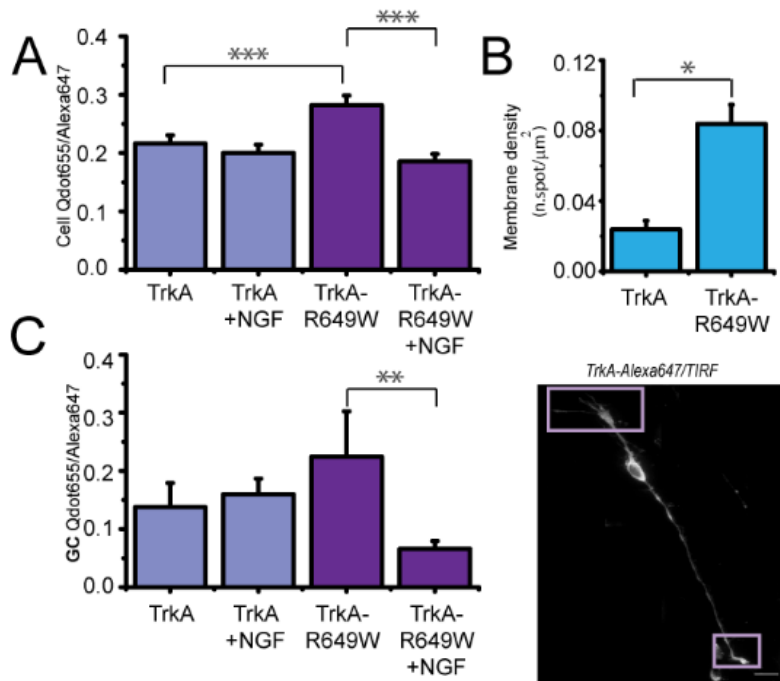


**Figure 3.2. A)** Quantification of the membrane pool fraction on the total pool of TrkA-wt and TrkA-R649W in DRG neurons before and after 1 h of stimulation with 125 ng/ml of mNGF. Quantification is obtained from the ratio between the intensity of Qdot signal (membrane receptors) against the intensity of Alexa488 (TrkA immunostaining) measured in the whole neuron (TrkA-wt, n=102 neurons; TrkA-wt+NGF, n=21 neurons; TrkA-R649W, n=87 neurons; TrkA-R649W+NGF, n=43 neurons). \*\*\*p<0.001 according to Kruskal-Wallis test. **B)** Quantification of density of labeled receptors per cell area (n.spots/μm<sup>2</sup>) in SHSY5Y cells, obtained from three experimental replicates (n=22 cells for TrkA-wt, n=12 cells for TrkA-R649W). \*p<0.05 according to two-tailed Mann-Whitney test. **C)** Membrane pool at growth cones responses after 1 h of 125 ng/ml of mNGF stimulation. Quantification of TrkA membrane pool at growth cones before (TrkA-wt, n=17 neurons and TrkA-R649W, n=11 neurons) after NGF stimulation (TrkA-wt, n=10 neurons and TrkA-R649W, n=10 neurons);

\*\*p<0.01 according to Kruskal-Wallis test. Right: Representative TIRFm image of a DRG neuron immunostained against TrkA with secondary antibody conjugated with Alexa488; growth cones are within the light purple boxes; scale bar: 20 nm).

In parallel we set-up a single molecule internalization assay (see paragraph 4.12) in neuroblastoma cells, in which we monitored with TIRFm the decrease of labelled membrane molecules during 1 hour of NGF stimulation, which confirmed that TrkA-wt and TrkA-R649W internalize with the same kinetics after ligand stimulation (Fig. 3.3).

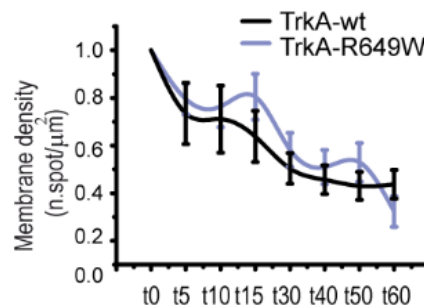


**Figure 3.3.** Membrane density quantification during NGF treatment in SHSY5Y cells for TrkA-wt (black line, n=33 cells) and TrkA-R649W (light purple line, n=52 cells): mean±sem from cells acquired at each time point normalized for the respective density at time 0 (time of NGF administration). Differences during time, but not between TrkA-wt and-R649W, are statistically significant according to two-way ANOVA test.

It is known that development and axonal growth depends on the organization and dynamics of the actin meshwork filling the growth cone [223]. The cytosol of the growth cone is highly compartmentalized: the *front domain* (or P-domain) is a region rich of actin organized in lamellipodia and filipodia, the *middle domain* is

characterized by membrane organelles and the *rear domain* by microtubules whose polymerization contributes to neurites elongation (Fig. 3.4 A, upper panel). It is well known that during the switch between stationary state and axonal elongation, the sensing of extracellular signals induces the loosening of actin filaments in the front domain of the growth cone, leading to its collapse, in favor of microtubule and membrane advance (Fig. 3.4 A) [224].

When analyzing the growth cone area in the presence of NGF stimulation, we found that neurons expressing TrkA-wt display growth cone areas that are smaller than in neurons expressing TrkA-R649W (Fig. 3.4 B). We expect that this difference could be even higher in a cell model devoid of endogenous TrkA, and it would be interesting to perform this experiment in future investigations. Indeed, for the explanation provided above, it could be that this failure to reduce the area could justify the deficiency in neurite outgrowth reported for neurons bearing this mutation [220]. Furthermore alterations of the area of growth cones, due to accumulation of vesicles and membrane organelles in the cytosol, were usually related to neurodegenerative axonal pathologies [224], [225]: experimental evidences obtained from neuronal culture revealed that larger growth cones tend to grow more slowly [224].

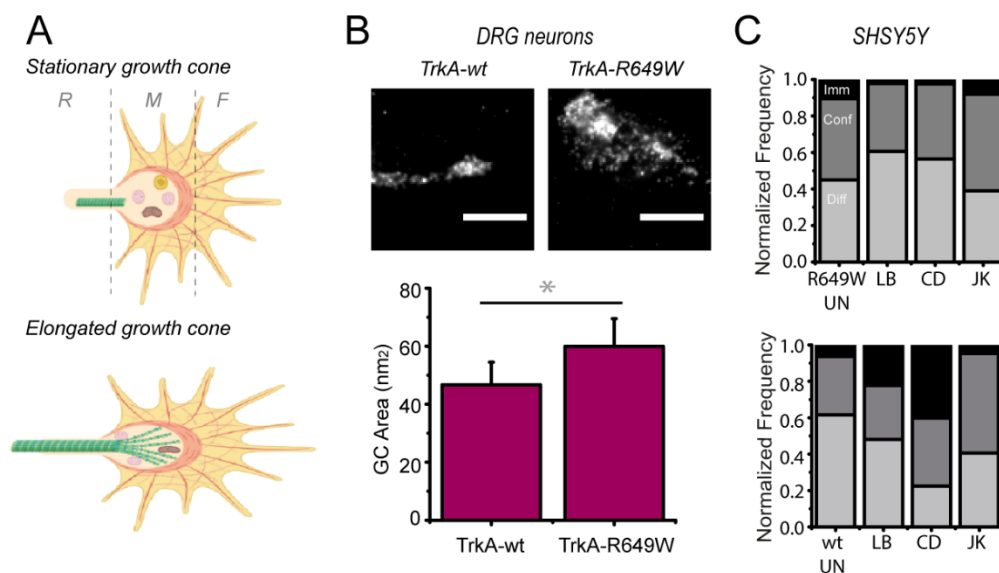


**Figure 3.4. A)** Schematic representation of a growth cone in stationary state (upper cartoon) and during the elongation step (lower cartoon); R represents the rear domain, M the middle domain and F the front domain. In the picture, we illustrated in green the microtubules, in brown mito.chondria, in yellow peroxisomes, in light pink lysosomes and in red the actin filaments. Figures are made using Biorender. **B)** Upper panel: representative TIRFm images of a growth cone for DRG neurons expressing TrkA-wt (left) and TrkA-R643W (right); scale bar: 10  $\mu$ m. Lower panel: corresponding quantification of growth cone area of DRG neurons at DIV 4 expressing TrkA-wt and TrkA-R649W in presence of NGF (TrkA-wt, n=23neurons; TrkA-R649W, n=23 neurons). \*p<0.05 according to two-tailed Mann-Whitney test. **C)** Upper panel: stack-column histogram plot for the distribution of diffusive (light grey), confined (grey) and immobile (black) TrkA-R649W receptors in untreated conditions and after CD, LB, JK treatments (UN, n=1331, CD, n=2558; LB, n=1815; JK, n=2149 trajectories) in SHSY5Y cells. All data are pools from 10-15 different cells collected in two independent replicas. Below: the same stack-column histogram plot for TrkA-wt of Fig. 2.13 D at paragraph 2.4, shown as reference.

The increased membrane pool of TrkA-R649W with respect to TrkA-wt at the growth cone (Fig. 3.2C) suggested us the possibility of an increased interaction of this receptor form with components of the cortical actin cytoskeleton, possibly with actin itself, as observed for the kinase inactive TrkA-K544N reported in paragraph 2.4 (Fig. 2.13). We therefore used the SPT approach in SHSY5Y cells in order to evaluate changes in the membrane dynamics of TrkA-R649W in response to three different drug treatments affecting the polymerization state of the actin meshwork. Obtained results indeed suggest an interaction between TrkA-R649W and some components of cortical actin: after actin depletion with latrunculin B (LB) and cytochalasin D (CD), we observe an increase of the diffusive population of TrkA-R649W and a decrease of its confined and immobile populations; on the contrary, the increased polymerization induced by jasplakinolide (JK) promotes a slight reduction of the diffusive population (Fig. 3.4 C, upper panel). For the TrkA-wt we did not observe the same features, as already shown in Fig. 2.13 and reported here as a reference (Fig. 3.4 C, lower panel).

### 3.3 INVOLVEMENT OF TRKA-R649W IN THE ALTERATION OF AUTOPHAGIC FLUX

HSAN IV disease is caused by several mutations randomly distributed along the TrkA sequence, which are responsible for the production of truncated and misfolded proteins; these are degraded by the autophagy pathway, which avoids the accumulation of proteotoxins, ensuring the maintenance of cellular homeostasis [225]. Several works reported the relation between TrkA overexpression and enhanced autophagy/cell death processes [226]–[228].

Considering the bulky membrane expression of TrkA-R649W, and its massive internalization at axon tips (see Fig. 3.2 A, C), we wanted to understand if this mutation could cause alterations of the autophagy machinery. Previously, another TrkA inactivating mutation related to HSAN IV, TrkA-L213P (characterized by a slower rate of internalization and degradation), was reported to increase the number of autophagosomal vesicles (AVs) when expressed in HeLa cells, triggering in this way the disruption of the autophagic flux [146]. This delayed degradation was reported to be responsible for the accumulation of misfolded proteins in the cytosol, thus for cell toxicity.

We co-transfected neuroblastoma cells with TrkA-wt or TrkA-R649W and a fusion construct bearing GFP fused to microtubule-associated protein light chain 3, LC3, known to be associated with autophagosome membrane [229] and for this reason commonly used to monitor the formation of AVs [222, 144]. Analysis at confocal microscope revealed cells expressing TrkA-R649W show higher number of AVs than the -wt, without NTs stimulation (Fig. 3.5).

The increased number of AVs found in the case of transfected TrkA-R649W indicates that the overexpression of the mutated protein causes surely an alteration in the autophagic flux, probably because of a reduced autophagosome turnover, as previously demonstrated for TrkA-L213P [146]. It is well known that when the autophagic pathway is compromised, cytoplasmic proteins and organelles included in the AVs cannot be degraded by the lysosomal pathway, inducing an accumulation of toxic products in the cell cytosol [230]. Further experiments will be needed to understand if this dysfunction was due to an impairment in the autophagosomes formation or in the fusion process of the autophagosomes with lysosomes; indeed, the loss of lysosome acidification and function is reported to be associated with AVs accumulation because autophagosomes do not fuse with dysfunctional lysosomes [231].

Furthermore, because autophagy regulates the physiological axonal homeostasis, further studies will be required to understand if the disruption of this process caused by TrkA-R649W mutation can contribute to an accumulation of toxic proteins and aggregates, responsible for neurodegeneration, as previously reported for TrkA-L213P [146].

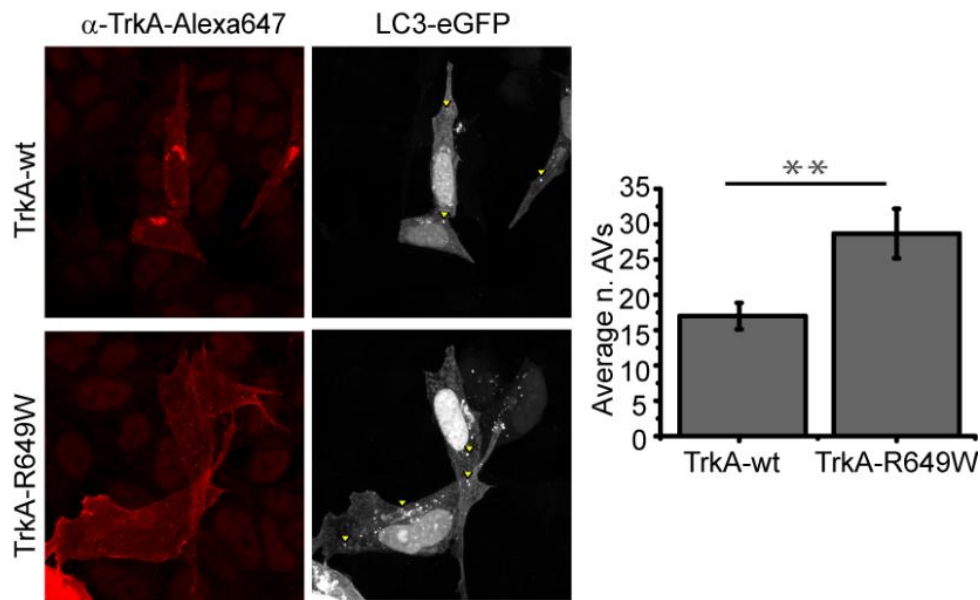


**Figure 3.5.** Left: Confocal microscopy images for SHSY5Y cells co-transfected with TrkA-wt and TrkA-R649W (red channel) and LC3-eFPF (grey channel). Right: number of AVs per cells (TrkA-wt, n= 16 cells; TrkA-R649W, n=26 cells); data are show as mean +/- sem; \*\*p<0.01 according to t-test.

### 3.4 CONCLUDING REMARKS

HSAN IV is a rare disease characterized by a wide spectrum of mutations inside the gene coding for TrkA receptor; among these, we focused on the TrkA-R649W mutation (R643W in human sequence), known to be associated to an impairment of kinase activity and differentiation [54]. Here we found that, in the absence of stimulation, TrkA-R649W is more exposed with respect to -wt at plasma membrane of DRG neurons transduced with either construct (Fig. 3.2 A,C). To overcome possible interferences due to the endogenous level of TrkA protein in DRG neurons from wild-type mice, we used also a cellular system with negligible levels of this protein (Fig. 3.2 B), finding the same trend. This result suggests that the loss of neuronal sensitivity responsible for the developmental alterations is not due to a reduced presence of mutated TrkA at plasma membrane. We then found that, despite its lack of kinase activity, TrkA-R649W is susceptible to NGF binding: indeed, after NGF binding, TrkA-R649W undergoes rapid internalization especially at growth cones (Figs. 3.2 C, 3.3). Furthermore, the increased growth cone area in TrkA-R649W expressing neurons suggests that TrkA-R649W/NGF complexes, even if they are internalized, could be less efficient to induce neurite outgrowth, as reported also in previous studies [232]. Our results allow us to speculate that TrkA-R649W mutation could affect the receptor intracellular fate, causing defects in terms of signaling and protein sorting. Interestingly, we found that cells overexpressing TrkA-R649W show also an higher number of AVs than cells overexpressing TrkA-wt (Fig. 3.5), confirming previous data demonstrating a relationship between HSAN IV TrkA mutants and autophagy alterations [146]. Further investigations will be required to understand if the increased number of AVS displayed by TrkA-R649W can be responsible, also in this case, for the accumulation of misfolded proteins, an aspect generally associated with neurodegenerative diseases [231]. In the future, it will be interesting to compare our in-vitro results with further studies on the knock-in mouse for TrkA-R649W that has been developed and is currently being investigated by the group of Prof. Cattaneo at Scuola Normale Superiore, with whom we started this collaboration. This combined approach should ultimately allow understanding deeper mechanisms behind the disease, ensuring to find, at the same time, common features with other HSAN IV mutations.

# 4. MATERIALS AND METHODS

This chapter contains the details of the methodological procedures of experiments described in Chapters 2 and 3 and in Appendix A. Contributions of Rosy Amodeo and other authors to these procedures have already been mentioned at the beginning of each of these sections. The procedures in whose optimization I was directly involved also appear in this publication: [195].

## 4.1 CONSTRUCTS

*Reference figures in chapters 2, 3 and Appendix A.*

ACP-tagged rat TrkA-wt construct has been previously described [160]. This construct was used as template to generate all rat TrkA mutants, using the QuikChange mutagenesis kit (Agilent) and a pair of specific oligonucleotides (Sigma) for each desired mutation. Multiple mutations of kinase and recruitment mutants (KM and RM) were introduced sequentially in the template sequence. S6-tagged human TrkA construct and S6-tagged P75<sup>NTR</sup> were previously described [183], [6]. Human cDNAs of TrkA-wt, TrkA-K544N, TrkA-R649W were also cloned in an “all-in-one” third generation Tet-on lentiviral pTRE vector, under an inducible promoter containing a Tet-responsive element (TRE) [168]. S6-VEGFR2 construct was obtained inserting the S6 tag sequence after the signal peptide of the murine cDNA of VEGFR2 through the GeneArt Synthesis service (Thermo Scientific) and cloning it into pSIN-TRE lentiviral vector [205]; VEGFR2-K866N and VEGFR2-K866R were prepared starting from the wt sequence using the QuikChange Site-Directed mutagenesis kit (Agilent) and a pair of specific oligonucleotides (Sigma) for each desired mutation. All mutations and relative primer sequences are reported in Table 4.1.

Construct	Mutation	Primers	
		Type	Sequence (5'→3')
rTrkA-K547N	K547N	FW	GCTGGTGGCTGTCAACGCACTGAAGGAGACATC
		RV	GATGTCTCCTTCAGTGC GTTGACAGCCACCAGC
rTrkA-RM	Y499F	FW	GGAGAACCCACAGTTCTTCAGTGATACCTGTGTC
		RV	GACACAGGTATCACTGAAGAACTGTGGGTTCTCC
	Y760F	FW	CTGCCCTCCTGATGTCTTCGCCATCATGGCGCGGC
		RV	GCCGCGCATGATGGCGAAGACATCAGGAGGGCAG
	Y794F	FW	CAGGCGCCACCGAGTTTCTGGACGTTCTGGGC
		RV	GCCCAGAACGTCCAGGAACTCGGTGGCGCCTG

rTrkA-KM	Y679F	FW	CATGAGCAGGGACATCTTCAGCACAGACTACTACC
		RV	GGTAGTAGTCTGTGCTGAAGATGTCCTGCTCATG
	Y683F	FW	CATCTACAGCACAGACTTCTACCGTGTGGGAGGTC
		RV	GACCTCCACACGGTAGAAGTCTGTGCTGTAGATG
	Y684F	FW	CTACAGCACAGACTACTTCCGTGTGGGAGGTCGG
		RV	CCGACCTCCACACGGAAGTAGTCTGTGCTGTAG
rTrkA-P791S	P791S	FW	CCTTGGCACAGGCGTCACCGAGTTACCTGG
		RV	CCAGGTAACCGGTGACGCCTGTGCCAAGG
rTrkA-K547R	K547R	FW	ATGCTGGTGGCTGTCAGGGCACTGAAGGAGAC
		RV	GTCTCCTTCAGTGCCCTGACAGCCACCAGCAT
hTrkA-K544N	K544N	FW	GCTGGTGGCTGTCAGGGCACTGAAGGAGGCG
		RV	CGCTCCTTCAGTGCGTTGACAGCCACCAGC
mVEGFR2- K866N	K866N	FW	ACTTGCAAACAGTAGCCGTC AACATGTTGAAAGAA GGAGCA
		RV	TGCTCCTTCTTTCAACATGTTGACGGCTACTGTTTTG CAAGT
mVEGFR2- K866R	K866R	FW	ACTTGCAAACAGTAGCCGTC CGGATGTTGAAAGA AGGAGCA
		RV	TGCTCCTTCTTTCAACATCCGGACGGCTACTGTTTTG CAAAGT
hTrkA- R643W	R643W	FFW	CAT TTT GTG CAC TGG GAC CTG GCC ACA CGC
		RRV	GCG TGT GGC CAG GTC CCA GTG CAC AAA ATG

**Table 4.1.** List of primers used in the mutagenesis procedure.

## 4.2 IMMORTALIZED AND PRIMARY CELL CULTURES AND TRANSFECTION

*Reference figures in chapters 2, 3 and Appendix A.*

SHSY5Y (a kind gift from Fondazione EBRI, Rome, Italy) were grown in DMEM/F-12 medium supplemented with 10% Fetal Bovine Serum, 1% Penicillin-Streptomycin and 1% L-Glutamine and 25 mM HEPES. HEK293T/17 cells (ATCC® CRL-11268™) were grown in DMEM High-Glucose (4.5 g/L) medium supplemented with 10% Fetal Bovine Serum, 1% Penicillin-Streptomycin, 1% L-Glutamine, 1% Sodium Pyruvate. Pc12-nnr5 cells and PC12 Crispr-Cas9

edited for TrkA knockout (a kind gift of Mario Costa, CNR-IN, Pisa) for TrkA were maintained in RPMI1640 medium supplemented with 10% horse serum, 5% fetal bovine serum and 1% Penicillin-Streptomycin (Gibco). Human umbilical vein ECs (HUVEC) cells were usually grown on substrates coated with porcine gelatin (Sigma-Aldrich) in M199 medium (Invitrogen, Carlsbad, CA) supplemented with 20% fetal calf serum (FCS) (Invitrogen), EC growth factor (100 g/mL) (Sigma-Aldrich), and porcine heparin (100 g/mL, Sigma-Aldrich). Fetal bovine aortic endothelial GM7373 cells [233] were grown in DMEM (Gibco, Life Technologies) containing 10% FCS, vitamins, essential and non-essential amino acids. GM7373 cells were transfected with a pcDNA3.1 expression vector harboring the mutated forms of murine VEGFR2 cDNA to generate stable GM7373-VEGFR2 transfectants: GM7373-K866N and -K866R. All animal procedures were approved by the Italian Ministry of Health (notification n°917) and were compliant with Italian (Ministry of Health guidelines, Legislative Decree n°26/2014) and European Union (Directive n°2010/63/UE) laws on animal research. The experiments were carried out in strict accordance with the approved guidelines. In addition, the principles of the Basel Declaration, including the “3R” concept, were followed throughout the whole project. The primary sensory neurons used in this study were obtained from the dorsal root ganglia of wild-type B6129 post-neonatal mice at day 3 (p3). For DRG extraction, the mouse is killed via cervical dislocation and pinned with the dorsal side facing up. First, we removed the skin on the back of the mouse with dissecting scissors. Then, we made two incisions along the dorsal side of the spinal cord and continued removing the spine until reaching the caudal part, removing also the spinal marrow. Using a stereo microscope, DRGs from all spinal levels were carefully removed and collected in a 6-cm petri dish placed on ice and filled with a solution of PBS and 50 units/ml of antibiotics (Penicillin/Streptomycin). After DRG extraction, we dissociated the neurons from ganglia as explained below: DRG were washed twice with PBS supplemented with 0.3% BSA (solution 1), then the culture was incubated at 37°C for 30 minutes with a solution of PBS with 15 mg of collagenase (Sigma Aldrich, C7657), 150 mg of dispase and 90 mg of glucose (solution 2). After cells centrifugation at 1000 rpm, we removed the supernatant and added to the cell culture the blocking solution of PBS supplemented with 0.3% BSA, 1.2 mg DNase (Sigma Aldrich, D5025) and 7.8 mg trypsin inhibitor (Sigma Aldrich, T9003) (solution 4). We centrifuged 2 minutes at 1000 rpm and added a solution of PBS supplemented with 1.2 mg DNase (Sigma Aldrich, D5025) and 7.8 mg trypsin inhibitor (Sigma, T9003) (solution 3). At this point, DRGs neurons were mechanically dissociated by pipetting through a fire-polished glass Pasteur pipet, until the suspension of dissociated cells was homogeneous. The cell suspension was left in a tube for 20 minutes for sedimentation and the superficial part of the cell suspension was collected in a new tube. We repeated the dissociation step for the remaining, not yet dissociated, DRGs. The cell suspension was centrifuged for 10 min at 1000 rpm, the supernatant was removed and the cells were resuspended in Primary Neuron Basal medium (PNBM, Lonza) supplemented with 1% L-glutamine (Lonza), 0.1% Gentamicin Sulfate/Amphotericin-B (Lonza), 2% NSF-1 (Lonza). In order to ensure neuronal survival, we added 100 ng/ml of NGF (Alomone Labs) to the cell

culture. 24 hours later we added 2.5 $\mu$ M AraC (Sigma-Aldrich) to inhibit glia proliferation and every three days we replaced 2/3 of the medium. For promoting cell adhesion, the glass bottom dishes, necessary for the microscopy acquisition of primary culture, had to be treated with 100 W O<sub>2</sub> 0.14 bar oxygen plasma for 2–3 min and then coated with 100 ng/mL poly-d-lysine and 2 $\mu$ g/ml of laminin at 37 °C overnight; substrates were then washed twice with sterile ddH<sub>2</sub>O and let dry under a sterile hood. Transfections were performed, if not differently specified, by using the reagent Lipofectamine™ 2000 (Thermo Fisher Scientific), according to the manufacturer's instructions, and transgene expression was typically monitored 24-48 h later.

### 4.3 PREPARATION OF VIRAL STOCKS FOR NEUROTROPHIN RECEPTORS

*Reference figures: 2.11, 3.1, 3.2, 3.4 and Appendix A.*

The day before transfection, HEK 293T/17 cells were seeded on a 10-cm diameter dish, in order to obtain a confluence of 45-50% the following day. Cells were incubated over night (ON) at 37°C in a 5% CO<sub>2</sub> humidified incubator. On the day of transfection, effectene (Effectene Trasfection Reagent, Quiagen) was mixed with an amount of (T × I)/L for each of the four packaging plasmids (pTRE-S6tagTrkA/p75<sup>NTR</sup>, pMD2.G, pMDLg/pRRE, pRSV-Rev), where T is the total amount of DNA to be used (determined on the basis of the surface of the dish where cells are plated; for example 0.5-2  $\mu$ g of DNA are recommended in 60 mm dishes), I is the length of each vector, and L is the sum of the lengths of the four vectors. The transfection mix was added to the cells following the manufacturer's instructions. We incubated the transfection mix with cells overnight and completely replaced medium with complete, fresh HEK293T cell culture medium the following day. After 48 h, we harvested culture medium containing virus-like particles (VLPs): first we centrifuged the medium at 500 × g for 10 min at 4°C in order to eliminate cell debris, we added 1/3 of total volume of Lenti-X™ Concentrator and incubate 1 hour at 4°C. We then centrifuge the concentrated VLPs at 1500 rpm for 45 min at 4°C, keeping the pellet on ice. The pellet is finally resuspended in 1/100 of the original packaging volume with PBS.

### 4.4 TRANSDUCTION OF IMMORTALIZED AND PRIMARY CELLS

*Reference figures: 2.11, 3.1, 3.2, 3.4 and Appendix A.*

One day before transduction, about 2 × 10<sup>6</sup> of SHSY5Y cells were seeded in a 30-mm-diameter culture dish, and cells incubated at 37 °C, 5% CO<sub>2</sub>. On the day of transduction, we prepared 0.36 mL of neuroblastoma infection medium, adding 35  $\mu$ L of viral stock, and vortexing the solution for few seconds. After the removal of all culture medium and two washes with PBS (supplemented with 1 mM CaCl<sub>2</sub>, 0.5 mM MgCl<sub>2</sub>) the infection mix was added to the cell layer. Cells were incubated at 37 °C, 5% CO<sub>2</sub> for 1 h, and gently shaken every 15 min to allow the VLPs to distribute homogeneously without drying in the middle of the plate. Finally we replaced infection medium

with complete neuroblastoma cell medium to allow transgene integration for 24–48 h. For DRG transduction, the day after plating, we prepared 1 mL of warm Neuron Growth Medium with 25- $\mu$ M glutamate and 4- $\mu$ g/mL polybrene, mixed with two aliquots of concentrated viral stock; and the solution was vortexed for few seconds to mix the viral particles. We then carefully removed medium from neuron cultures, washed once with warm HBSS, and gently added the new solution with the virus onto the cultures, before incubation at 37 °C in a 5% CO<sub>2</sub> humidified chamber for 2 h. After removal of the infection medium, we poured 1 mL of warm Neuron Growth Medium supplemented with 50 ng/ml of mNGF and 2.5- $\mu$ M cytosine  $\beta$ -d-arabinooside, which inhibits glia proliferation. Cells were maintained at 37 °C under 5% CO<sub>2</sub> humidified atmosphere for at least 48 h to let the transgene integration. Neuron culture medium needs to be refreshed every 3–4 days, removing about 1/3 of the volume and substituting it with warm, fresh Neuron Growth Medium.

## 4.5 IMMUNOBLOTTING AND IMMUNOPRECIPITATION

*Reference figures: 2.4, 2.9 A, 2.10 A, 2.14 and A.3.*

Both phosphorylation and ubiquitination of different TrkA constructs were monitored after TrkA immunoprecipitation. 24 to 48 h after transfection, SHSY5Y cells or HEK293T/17 (for the evaluation of the ubiquitination) were starved for two hours in DMEM/F-12 medium supplemented with 1% Penicillin-Streptomycin and 1% L-Glutamine and 25-mM HEPES (starvation medium). Then, cells were incubated for 10 minutes at 37°C in starvation medium, either in absence or presence of 125 ng/ml native mouse NGF (mNGF, Alomone Labs) and finally lysed in RIPA buffer (Sigma Aldrich) supplemented with phosphatase and protease inhibitor tablets (PhosSTOP™ cOmplete™, EDTA-free Protease Inhibitor Cocktail, Sigma Aldrich). Total cell extracts (500  $\mu$ g) were incubated with the pan-Trk antibody C-14 or B-3 overnight at 4°C under rotary shaking. The mixture of antibody and lysates were then incubated 30 minutes at room temperature with Dynabeads® protein A (10001D, Thermo Fisher Scientific), previously washed three times with phosphate buffer saline (PBS) solution with 0.002% Tween-20 (PBST). The resulting complexes in the mixture were then magnetically isolated and beads washed once with PBST. The Trk-antibody complexes were eluted from the beads by boiling samples in 2X Laemmli loading buffer at 95 °C for 10 minutes. Samples were then loaded on a gel (4-12 % pre-cast gradient gel, Biorad) and electrotransferred on a PVDF membrane (Immobilon®-P PVDF Membrane, Millipore). This membrane was blocked for 1 hour at RT with Tris Buffered Saline + 0.05% Tween-20 (TBST) supplemented with 5% w/v not-fat dry milk (Biorad) for the ubiquitination assay, and with TBST+ 5% w/v BSA (Sigma) for the phosphorylation assay. After blocking, membranes were blotted for 2.5 hours at RT with anti-P4D1 and anti-phosphotyrosine for ubiquitination and phosphorylation evaluation, respectively. The primary antibodies were detected by using an anti-mouse or rabbit secondary antibody horseradish peroxidase (HRP)-conjugated (diluted

1:2500). For the degradation assay the only difference was that, after the starvation, cells were incubated for 0, 15, 60 minutes at 37°C in starvation medium presence of 125 ng/ml native mNGF and finally lysed. To evaluate the total TrkA level in the degradation assay, total cell extracts (50 µg) were boiled in 2X Laemmli Sample at 95 °C for 10 minutes. Samples were loaded on a gel, electrotransferred on a PVDF membrane, blocked with TBST supplemented with 5% w/v not fat dry milk and then blotted with anti-TrkA antibody exactly as described above. Serum-starved sub-confluent wild type GM7373, GM7373-K866N and -K866R were stimulated with 30 ng/mL of VEGF-A for 5 minutes. Cells were then lysed in lysis buffer [50 mmol/L Tris-HCl buffer (pH 7.4) containing 150 mmol/L NaCl, 1% Triton X-100, 1 mmol/L Na<sub>3</sub>VO<sub>4</sub>, and protease and phosphatase inhibitors (Sigma)]. Next, 50 µg of total cell lysate were separated by SDS–PAGE and probed with anti-phospho-VEGFR2 antibody (pTyr1175, Cell Signaling Technology, Beverly, MA), and anti-VEGFR2 antibody (Santa Cruz Biotechnology) in a Western blot. The following are the primary antibodies used: anti-TrkA (06-574, dilution 1:1000), anti-phosphotyrosine (05-321, dilution 1:1000), anti-P75<sup>NTR</sup> (07-476, dilution 1:1000) were from Millipore, anti-Trk C-14 (sc-11, pan-Trk) and anti-P4D1 (sc-8017, multimonoubiquitin and polyubiquitin antibody, 2 µg/ml) were from Santa Cruz Biotechnology.

## 4.6 TRKA DETECTION BY IMMUNOFLUORESCENCE

*Reference figures: 2.12, 3.1, 3.2, 3.4 and 3.5.*

48 hours after transduction, neurons are starved at 37°C for 1 hour, then the membrane pool of receptors is biotinylated in two steps: first, 30 minutes at 37°C with 10 µM Coenzyme A-biotin, 10 mM MgCl<sub>2</sub> and 2µM of SFP synthase resuspended in cell medium and then, 60 minutes at 4°C with the same mix. Cells were eventually incubated with 125-ng/ml NGF at 37°C for 60 minutes for ligand treatment. After three washes with Hanks' Balanced Salt solution (HBSS, Sigma Aldrich-55021C), cells were labelled at 4° for 15 minutes with 10 nM of streptavidin-Qdot (Qdot® 655 streptavidin conjugate; Invitrogen) in borate buffer at pH 8.3, 0.5% BSA and 215 mM sucrose. Cells were washed five times with HBSS and then fixed at RT for 15 minutes in PBS with 2% paraformaldehyde (PFA) and 5% of sucrose. After four washes with HBSS, we permeabilized neurons at RT for 5 minutes with a solution of PBS supplemented with 2.5% BSA and 0.1% Triton-X100; we washed four times again and blocked at RT for 1 hour with a solution of 5% BSA resuspended in Phosphate Buffer Saline (PBS). Then, cells were incubated at RT for 2 hours with anti-TrkA (Millipore, 06-574, dilution 10 µg/ml) in PBS and 2.5% BSA. After three washes with PBS, cells were incubated at RT for 1 hour with anti-rabbit alexa647 antibody (Termofisher, dilution 1:100); finally, we washed three times with HBBS and once with ddH<sub>2</sub>O.

For image analysis of the total membrane pool, we used the ImageJ software: first, we subtracted the fluorescence value of the background in both channels, then we drew a mask around the cell and measured the

fluorescence intensity of Qdot655 ( $I_{\text{Qdot655}}$ ) and Alexa488 ( $I_{\text{Alexa488}}$ ). The fraction of labelled receptors exposed at neuronal cell surface is proportional to  $I_{\text{Qdot655}} / I_{\text{Alexa488}}$ , and was quantified with this value. For the image analysis of growth cones, we drew the mask only on the growth cones and then we measured both the  $I_{\text{Qdot655}} / I_{\text{Alexa488}}$  ratio and the area. For the evaluation of the AVs number, SHSY5Y cells were co-transfected with TrkA-wt or TrkA-R649W and LC3-GFP plasmid [234]; 24 hours later, cells were starved for two hours, washed two times with PBS and fixed at RT for 10 minutes in PBS with 4% of PFA. After three washes, cells were permeabilized at RT for 5 minutes with PBS with 2.5% BSA and 0.1% Triton-X, washed five times again and blocked at RT for 1 hour with PBS supplemented with 5% BSA. We then washed three times with PBS supplemented with 2.5% BSA and incubated cells at RT for 2 hours with a 1:50 dilution of anti-Trk receptor (B-3) resuspended in PBS with 2.5% BSA. Then, cells were incubated at RT for 1 hour with a 1:100 dilution of anti-mouse/Alexa647 and finally washed three times before imaging at the confocal microscope. We collected Z-stack images of fixed cells with Zeiss LSM800 Airy Scan microscope using a 63X oil immersion objective (N.A 1.4); TrkA-Alexa647 and LC3-eGFP were excited with the 633 and 488 nm laser lines and acquired in the ranges 650-700 nm and 500-600 nm, respectively. For the image analysis, we used ImageJ software: we applied a maximum intensity projection on the Z-stacks for LC3-eGFP corresponding to  $\alpha$ -TrkA/Alexa647 positive cells; finally, we averaged the number of AVs present in each cell and plotted the data as mean  $\pm$  sem.

## 4.7 DRUG TREATMENTS

*Reference figures: 2.12, 2.13 and 3.4 C.*

Different drug concentrations and incubation times were tested to calibrate the experimental conditions needed to affect actin polymerization in SHSY5Y cells.

24 hours after transfection, SHSY5Y cell were starved for 2 hours before or during the drug treatment; finally cell were fixed for 10 minutes at RT with 4% PFA. Cells were then washed twice with PBS, permeabilized for 4 minutes at RT with 0.1 % TritonX-100 in PBS (Sigma Aldrich), washed twice again with PBS and blocked for 20 minutes at RT with 1% Bovine Serum Albumin (Sigma Aldrich) in PBS. After blocking, cells were incubated with a dilution 1:40 of Alexa Fluor 647-Phalloidin (Invitrogen) resuspended in blocking solution. Finally, cells were washed twice with PBS, once with water (Millipore), dried and mounted in Fluoroshield mounting medium (Sigma Aldrich). Samples were acquired at the TIRFm, using a penetration depth of 150 nm, an HCX PL APO 100X (NA 1.47) objective and a ROI of 58.4 $\mu$ m x 58.4 $\mu$ m; excitation was done with the 488-nm laser line and emission was collected with a FF01-525/45-25 Semrock filter. Based on phalloidin staining, we defined as optimal the following incubations: i) 2h at 37 °C with 1 $\mu$ M cytochalasin D (Sigma-Aldrich) during serum starvation before labelling; ii) 15 min at 37 °C with 1  $\mu$ M latrunculin B (Sigma-Aldrich) in the last half of labelling; iii) 30 min at 37°C with 100

nM jasplakinolide (Sigma-Aldrich) during labelling. Cells were then labelled as described previously, washed eight times with PBS, and then imaged in medium devoid of drugs.

## 4.8 FLUONGF BINDING ASSAY

*Reference figures: 2.1. B and 2.6 A.*

SHSY5Y cells were transfected with TrkA constructs. 5 hours after transfection, cells were trypsinized and seeded on glass slides at a confluence as about 70-90%. Next day, cells were serum starved for 2 hours and then surface receptors were exposed for 30 minutes at 37°C to 100 ng/ml purified Alexa647-NGF conjugate (fluoNGF, prepared as in [173]). After five washes in PBS, cells were fixed for 30 minutes at room temperature in 4% PFA, 4% sucrose in PBS, washed three times with PBS and one time with deionized water. Glass slides were then mounted with Fluoroshield™ and imaged at the TIRF microscope set in epifluorescence mode. Quantification of the NGF signal was performed by calculating the mean intensity of Alexa647 channel for GFP-positive cells (i.e. TrkA-expressing cells).

## 4.9 DIFFERENTIATION ASSAY

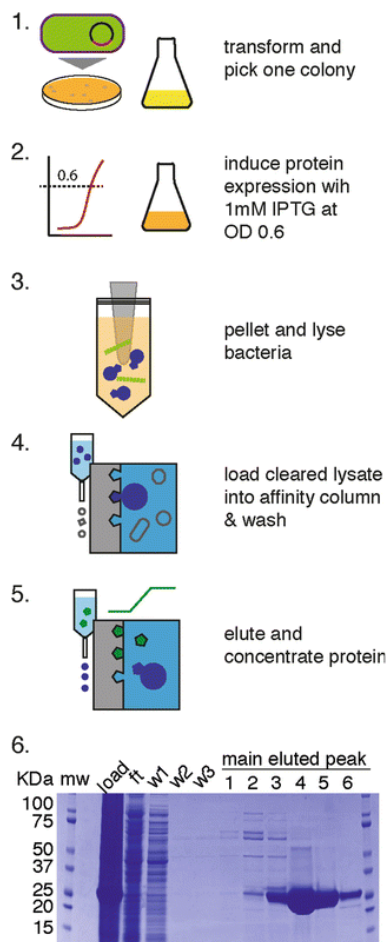
*Reference figures: 2.16.*

PC12-nnr5 cells [235] and PC12 Crispr-Cas9 edited for TrkA knockout (a kind gift of M. Costa, Institute of Neuroscience, CNR, Pisa, Italy) were transfected with TrkA constructs according to the manufacturer-recommended procedure of the Nucleofector™ technology by Lonza; they were then plated into 48-well tissue culture plates previously coated with a sufficient volume of PDL to cover the well surfaces. Cells were plated in pre-warmed RPMI containing 5% FBS, 10% Horse serum (HS), 1% Pen/Strep and L- glutamine, supplemented or not with 100 ng/ml of NGF and finally incubated at 37°C for 24 hours before imaging acquisition. After imaging at 24 h, the medium was refreshed with 100 ng/ml of NGF, cells incubated for other 24 hours at 37°C and imaged for the time point 48h. To evaluate differentiation at different time points we used an inverted microscope equipped with a 20 × /40 × magnification objective (Leica DMI4000B microscope). Morphometric analysis was performed on images taken with transmitted light. We collected 10 fields (with about 5-10 cells for field) for each construct; the number of differentiated cells, expressed as a percentage on the total transfected cells in the field, was obtained counting TrkA positive cells with at least one neurite with a length greater than the diameter of the cell body. The neurite length was measured manually tracing the length of neurites in differentiated cells with ImageJ software; we plotted the average value obtained. For PC12-nnr5 cells, data were obtained from two independent experimental replicates, while we analyzed only one experiment for PC12 Crispr-Cas9 edited for TrkA knockout.

## 4.10 SFP SYNTHASE PRODUCTION AND PURIFICATION

*Reference figures in chapters 2, 3 and Appendix A,B.*

We transformed 50- $\mu$ L of competent cells (BL21 star D3) with 7.5 ng of DNA plasmid coding for the PPTase enzyme (a kind gift of Yun Jin, Georgia State University), and then supplemented the mixture with SOC medium, and let it grow at 37 °C for 1 h in a shaking incubator. We plated transformed bacteria onto a LB agar plate containing 25- $\mu$ g/mL kanamycin (added from a 25-mg/mL stock) and incubated it at 37 °C for 14–16 h. Then we picked 1–3 colonies from the LB agar plate to prepare starter cultures inoculating each bacterial clone in 10 mL of LB containing 25- $\mu$ g/mL kanamycin; we grew the culture for 14–16 h with orbital shaking at 250 cycles per minute at 37 °C (step 1 in Fig. 4.1). 4.5 mL of the starter culture were transferred into 500 mL of LB medium containing 25- $\mu$ g/mL kanamycin and incubate at 37 °C at 250 rpm until the optical density at 600 nm of the bacterial suspension reaches a value of approximately 0.6. At this point we induced protein expression adding 1 mM isopropyl  $\beta$ -D-thiogalactopyranoside (IPTG) to the bacterial suspension, then incubated at 30 °C with orbital shaking at 250 cycles per minute for 18 hours (step 2 in Fig. 4.1). After this we pelleted cells at 6000 g, 4 °C for 20 min and resuspended the pellet in 10 mL of lysis solution; the suspension was sonicated on ice with six pulses of 30 s, separated by 60-s pauses. To remove the cellular debris from the lysate we spin down the solution by two subsequent centrifugations at 13,000 g at 4 °C for 30 min. It was important to filter the cleared lysate through a 0.45- $\mu$ m syringe filter before loading the lysate in the column for fast protein liquid chromatography (FPLC) purification (step 3 in Fig. 4.1). Before loading the lysate, we washed the column with 3–5 column volumes of distilled water, and then equilibrate it with 5 column volumes of binding buffer. The lysate was loaded in the FPLC system using a syringe, and then injected into the column. We collected fractions corresponding to the flowthrough, washed the column with 10–15 column volumes of binding buffer (until the measured absorbance reached a stable baseline), collecting fractions corresponding to the washing (step 4 in Fig. 4.1). We eluted the protein of interest applying a linear gradient from 0 to 100% of elution buffer in 30 column volumes and collected 2 ml of each eluted fractions in separate tubes (step 5 in Fig. 4.1). In order to analyze the collected fractions we ran an SDS-PAGE gel; we first stained the gel for 30 min at RT, and then destained it for a few hours to overnight (step 6 in Fig. 4.1). We pooled fractions displaying at least 90% protein purity, dialyzing the protein against an appropriate volume of dialysis buffer. After dialysis, we concentrated the protein to 100–200  $\mu$ M by ultrafiltration using a membrane with a 3.5 kDa cutoff (this is sufficient to get rid of imidazole and excess salt,



without losing protein). To quantify the obtained purified protein, we ran by SDS-PAGE serial dilutions of the concentrated protein solution together with known amounts of purified lysozyme as standard. As previously described, we stained and destained the gel to detect the results, comparing the enzyme lanes with the standard ones to estimate the purified enzyme concentration. Finally we resuspended the concentrated protein in a storage buffer composed by 20 mM Tris-HCl (pH 7.5), 150 mM NaCl, and 25% glycerol, preparing ~100- $\mu$ L aliquots of the protein solution to be stored at  $-80^{\circ}\text{C}$ .

**Figure 4.1.** Schematic representation of PPTase production in *E. coli*. PPTase-coding plasmid is transformed in BL21 bacteria and plated to obtain single colonies (1), then one colony is selected, grown, and protein expression induced with IPTG (2). Bacteria are pelleted and resuspended in lysis buffer and sonicated (gray tip in the falcon tube) to break bacterial walls (green) (3). The clarified supernatant is loaded on a HiTrap affinity column and washed to remove unspecific column binders (4). Finally, the purified protein is eluted from the column with imidazole gradient (green) and concentrated before long-term storage (5). Evaluation of all fractions collected during the procedure by SDS-PAGE allows one to identify and pool fractions containing purified protein (fractions 4–6 of the main eluted peak). ft column flowthrough, w1,2,3 column wash fractions (6).

## 4.11 SINGLE MOLECULE LABELING AND IMAGING OF SURFACE RECEPTORS

*Reference figures in chapters 2, 3 and Appendix A.*

5 hours after transfection, cells were trypsinized and transferred into Willco-dish<sup>®</sup> glass-bottom chambers (at a density of  $2\text{-}3 \times 10^5$  cells per 22-mm-diameter glass-bottom WillCo dish). Next day, cells were serum starved for 2 hours and surface TrkA, VEGFR2, P75<sup>NTR</sup> receptors were labeled with quantum dot probes or directly with CoA-fluorophores as described previously [162], [183], [221]. Briefly for the labelling with Qdot, cells were first biotinylated with an incubation of 30 minutes at  $37^{\circ}\text{C}$  in 0.5% Bovine Serum Albumin (BSA),  $1\ \mu\text{M}$  SFP synthase,  $10\ \text{mM}$   $\text{MgCl}_2$  and  $2\ \mu\text{M}$  of coenzyme A-biotin resuspended in starvation medium. After two washes in PBS, cells were incubated for 2 minutes at room temperature (RT) with  $2\ \text{nM}$  S-Qdot (Qdot<sup>®</sup> 655 streptavidin conjugate; Invitrogen) in borate buffer at pH 8.3, 0.5% BSA and  $215\ \text{mM}$  sucrose. Cells were washed eight times with PBS, ensuring a minimal non-specific adhesion of S-Qdots to the glass surface, and then stimulated with  $125\ \text{ng/ml}$  mNGF diluted in starvation medium. Ligand addition was performed directly on the dish at the TIRF microscope: in order to perturb as little as possible the position of the petri at the microscope stage, a  $250\ \text{ng/ml}$  mNGF

solution in starvation medium was added drop by drop to an equal volume of medium in the dish. Unless otherwise stated, cells were always imaged for a maximum of 15 minutes after ligand addition.

For the labelling with fluorophores, cells were incubated for 30 minutes at 37°C with a mix containing 2  $\mu$ M SFP synthase, 10 mM MgCl<sub>2</sub> and 500 nM CoA-fluorophores in starvation medium. Cells were then washed five times with PBS, and imaged in starvation medium with TIRFm. In light of the better performance displayed by Abberior 635P (see Appendix A), we performed single step photobleaching assay of S6TrkA-wt, S6TrkA-K544N and S6TrkA-K544R labelled with CoA-Abberior 635P. 24 hours after doxycycline induction, SHSY5Y cells expressing TrkA -wt, -K544N, -K544R were starved for 2 hours. Then all constructs were labelled for 30 minutes at 37°C with 20 nM CoA-Abberior635P, 1  $\mu$ M SFP synthase, 10 mM MgCl<sub>2</sub> in starvation medium; cells were treated for 15 min at 37°C with 125 ng/ml mouse NGF (Alomone Labs), diluted in starvation medium, before the next steps.

## 4.12 SINGLE MOLECULE INTERNALIZATION ASSAY

*Reference figures: 2.5 and 3.3.*

Transfected or transduced SHSY5Y cells seeded in glass-bottom WillCo dishes were starved for 2 hours, receptors were biotinylated and labelled with 2 nm of S-Qdot, then the cells were imaged at the TIRF microscope. The automatized stage was used for saving the position of 4-5 fields in which a sizeable number of cells displayed Qdot moving particles. We then added 125-ng/ml NGF to the medium and followed the cells in the selected fields in a time course of eight points (0, 5, 10, 15, 30, 40, 50 and 60 min); as control, we repeated a similar experiment without adding NGF. For each cell and time point, we quantified the membrane density as the number of labelled receptors within cell area (as deduced from the relative DIC image), in order to measure enrichment or depletion of surface TrkA-wt and -K547N receptors in the presence or absence of NGF stimulation. For comparing the internalization time-course of different cells, we normalized the spot density of each cell to its value at time 0. Cells with a similar (average) transgene expression levels were chosen, excluding those with a number of moving labelled receptors below 3.

## 4.13 SINGLE STEP PHOTOBLEACHING ASSAY

*Reference figures: 2.11.*

After labelling with 20 nM CoA-Abberior635P, cells expressing S6-TrkA, S6TrkA-K544N and S6TrkA-K544R were washed twice with PBS, fixed for 90 min at room temperature with 4% PFA/2% Sucrose/0.1% Glutaraldehyde in PBS (GA, Electron Microscopy Sciences), then washed five times with PBS and imaged. We acquired a 3000-frame movie (needed to achieve exhaustive fluorophore photobleaching) in a 144 x 144 pixels (32.68 x 32.68  $\mu$ m) ROI, with 21-ms integration time. Time series were then analyzed following the procedure reported in [169]: briefly,

the background fluorescence was subtracted using the ImageJ software rolling ball algorithm (with a 6 pixel radius) on the whole movie. Then the first 20 frames were averaged and a mask was calculated using a threshold lower bound set as four times the mean intensity of a region without fluorescent spots. Single spots were identified and detected as isolated fluorescent signals falling within a 3 x 3 pixels ROI, so that the number of photobleaching steps therein could be quantified. As reported in [169], we applied precise criteria to identify particles: i) spots needed to be clearly distinguishable and not belonging to areas of clustered receptors; ii) number of photobleaching steps was calculated only for profiles whose intensity reached background by the end of the movie; iii) spots whose intensity step up during the movie were discarded; iv) spots whose intensity trajectories were very scattered were discarded; v) the first step before photobleaching must be at least 5 frames long; vi) when blinking occurs, pre-blink intensity must be equal to post-blink one; vii) blinking must in any case not exceed 20% of the time the particle is observed; viii) when more than one photobleaching events are observed, their relative steps must be similar.

## 4.14 TIRF MICROSCOPY

*Reference figures in chapters 2, 3 and Appendix A,B.*

Labelled cells were imaged at 37°C, 5% CO<sub>2</sub> with a Leica DM6000 microscope equipped with a TIRF-AM module, incubator chamber, electron multiplying charge-coupled-device (CCD) camera (ImagEM C9100-13, Hamamatsu), and 100× oil immersion objective (NA 1.47). For live cell imaging, time series were acquired on a region of interest (ROI) with constant size of 32.7×34.5 μm within the basal membrane of each cell; Qdot655 was imaged using the 488 nm laser line, FF01-655/15 Semrock emission filter and a penetration depth of 110 nm. For single step photobleaching assay, we used a ROI of 32.68 x 32.68 μm and Abberior635 was excited using the 635 nm laser line with a penetration depth of 90 nm. The integration time per frame, corresponding to the lag time between two consecutive frames, was set at 21 ms and typical time series lasted 3000 frames.

For the comparative study of S6-TrkA labelling with different CoA-fluorophores (see appendix A.2), Abberior635P, Alexa647 and Atto633 were imaged using the 635-nm laser line with a 110-nm penetration depth for excitation and a Cy5 Leica1152303 emission filter. Atto550 and Alexa568 were imaged using the 561-nm laser line with a 350-nm penetration depth and a RFP Leica513894 filter cube. Abberior488, Alexa488 and Atto488 were imaged using the 488 nm laser line with 90 nm penetration depth for excitation, a 482-510 excitation filter and a BP 525/20 Leica emission filter. Laser power, gain and EM gain values were kept constant within different groups to allow quantitative comparisons; exposure times were 45 msec for Abberior488, Alexa488 and Atto488; 60 msec for Atto550 and Alexa568; and 40 msec for Abberior635, Alexa647 and Atto633.

## 4.15 SPT DATA ANALYSIS

*Reference figures: 2.1, 2.2, 2.3, 2.6, 2.9, 2.10, 2.13, 2.14 C, 2.15 and 3.4 C.*

Membrane dynamics of both TrkA and VEGFR2 single particles was analyzed as previously described [160], [162]. Briefly, Imaris software 7.6.5 (Bitplane Scientific Software) was used to detect and localize single Qdot-labelled TrkA spots and to generate the relative trajectories. Spots of Qdots non-specifically adhered to the glass outside the cell were discarded by considering the superposition of the TIRF and DIC images. The obtained trajectories were finally exported in MATLAB-compatible files using the Imaris XT module. Exported trajectories were analyzed with the custom MatLab algorithms described previously [161], with minor modifications. Briefly, complex trajectories switching between diffusive and confined regimes were segmented into the relative subtrajectories and separated into simple, self-similar trajectories. The pool of all (sub)trajectories was analyzed to compute the following parameters: i) the short-lag-time average diffusion coefficient  $D$  ( $\pm$ sem), calculated from the first two points of the mean square displacement (MSD) curve; ii) the confinement length  $L$  ( $\pm$ sem), i.e. the diameter of the area explored by “non mobile” trajectories; iii) the  $\gamma$  coefficient ( $\pm$ sem), calculated from the moment scaling spectrum (MSS) curve, similar to the “anomalous diffusion parameter” ( $\gamma <, \sim, > 0.5$  for subdiffusive, Brownian, and superdiffusive trajectories, respectively) [181]. The experimental distributions of  $\gamma$  versus  $D$  values obtained for all trajectories revealed the existence of several different motion types for both TrkA and VEGFR2, as previously shown ([161] and Fig. S6). Here, for the sake of simplicity, we identified three distinct motion macro-categories: diffusive, confined and immobile, and pooled both TrkA and VEGFR2 trajectories accordingly, on the basis of their relative  $D$  and gamma values. We plotted the experimental distributions of  $L$  for non-mobile trajectories, of  $D$  for mobile ones, and of  $\gamma$  versus  $D$  for all trajectories (considering always the number of spots in each trajectory, and also the parameter uncertainties in the last two cases; see also § 2.13). Especially the last kind of plot revealed the existence of several different motion types for both TrkA and VEGFR2, as also previously discussed [162]. Accordingly, the fraction of TrkA and VEGFR2 receptors in these three categories was calculated and used to generate the stack-column histogram plots.

## 4.16 STRUCTURAL MD SIMULATIONS

*Reference figures: 2.7, 2.8 and 2.10 B.*

We performed Molecular Dynamics (MD) simulations of the *h*TrkA-wt TKD and of its K544N, K544R, K544P and K544A mutants, and of *h*VEGFR2 TKD and its K868N and K868R mutants. The structure of *h*TrkA TKD was taken from the X-ray structure with PDB code 4f0i (starting with Cys501 and ending with Val790; [208]) and that of VEGFR2 from PDB code 6gqq (Leu814 to Asn1168; [237]). For TrkA, two protein chains are present in the PDB file and we chose chain B as the starting structure because residues 535 and 536 are missing in chain A. The

Reduce software [238] was used together with Whatif [239] to fix the orientation of Asn/Gln/His amino acids and detect the protonation of histidine residues. The two software packages gave the same results concerning the histidine buried inside the protein while they differed for some solvent exposed histidine. We considered an  $\epsilon$  protonation (protonation at  $\epsilon$ -nitrogen of the His) for His 569, 594, 645, 648 and 772 in TrkA, and 816, 876, 879, 891, 895, 1004, 1026 and 1144 in VEGFR2, and  $\delta$  protonation (protonation at  $\delta$ -nitrogen of the His) for all the other His residues. Mutations of Lys 544 (Lys868 in VEGFR2) to Asn, Arg, Pro and Ala were performed using the Rosetta software [240]. All proteins were solvated in a  $\sim 9$  nm truncated octahedron box of  $\sim 17000$  water molecules with a 0.1 M concentration of NaCl. The Amber ff99SB\*-ILDN [241], [242] was used with TIP3P force field parameters for water. Within a periodic boundary condition set up, the system was subjected to geometry optimization by minimizing its total potential energy and then equilibrated with short MD simulations at constant temperature and pressure, applying restraints of decreasing strength to keep the non-hydrogen atoms of the protein close to the starting structure (20ps with 5000 kcal/mol  $\text{\AA}^{-2}$ , 50ps with 3000 kcal/mol  $\text{\AA}^{-2}$  and 200ps with 1000 kcal/mol  $\text{\AA}^{-2}$ ). The equilibrated structures were used as starting points for 800ns-long production runs (600ns for VEGFR2). In the case of *h*TrkA-wt, -K544N and -K544R, three different MD runs starting from the same geometry but different randomly assigned velocities were performed. Production runs employed a 2 fs time step (LINCS was used to constraint bonds involving H atoms), v-rescale thermostat (with a coupling of  $\tau_T = 0.2$  ps) and Parrinello-Rahman barostat ( $\tau_P = 5$  ps) to maintain a constant 300 K temperature and 1 bar pressure respectively. Snapshots were saved each 10 ps and the first 100 ns of each MD trajectory were discarded in the analysis. Simulations and analyses were performed with the Gromacs 5 package [243].

## 4.17 STATISTICAL ANALYSIS

*Reference figures in chapters 2, 3 and Appendix A, B.*

Statistical analysis was performed with OriginPro v8.50 and GraphPad Prism 6 softwares, or with algorithms implemented in MatLAB. For most of the experiments, we used a one-way ANOVA, with Bonferroni's means comparison. The time course of *r*TrkA-wt versus *r*TrkA-K547N internalization was analyzed with a two-way ANOVA. Non-parametric tests for analysis of two samples were performed with the Mann-Whitney test, of more than two samples with the Kruskal-Wallis test followed by Dunn's means comparison. Significance was set at  $\alpha=0.05$ . For testing differences in D and L distributions we evaluated the error in each bin  $j$  considering the different weight  $w_{ji}$  in it for each trajectory  $i$ : the frequency  $f_j$  and its variance  $\sigma_{f_j}^2$  was calculated as  $f_j = \sum_{i=1}^n w_{ji}$ ,  $\sigma_{f_j}^2 = \frac{n}{n-1} \left( \sum_{i=1}^n w_{ji}^2 - \frac{(\sum_{i=1}^n w_{ji})^2}{n} \right)$  as in [244], where  $n$  is the total number of trajectories. For L,  $w_{ji}$  was 0 if the trajectory parameter L was not in the bin  $j$ , else the number of spots in the trajectory. For D,  $w_{ji}$  was

calculated considering the integral within the bin  $j$  of a Gaussian centered on the diffusivity  $D_i$  of the trajectory  $i$ , with width given by its uncertainty and integrated area given by the number of spots in the trajectory.

Normalized frequencies and their error bars were calculated dividing  $f_j$  and  $\sigma_{f_j}$  by  $\Delta \sum_j f_j$ , where  $\Delta$  is the bin width and the sum is over all bins. Differences in frequency counts in single-step photobleaching assay and in L and D distributions were analyzed using  $\chi^2$  tests, differences for the D shown with box-plots were analyzed as described in [169].

For  $\chi^2$  tests, the  $\chi^2$  statistic is

$$\chi^2 = \sum_{k=1}^2 \sum_{j=1}^N \frac{(f_j^{(k)} - E_j^{(k)})^2}{\sigma_{E_j^{(k)}}^2},$$

where  $k$  refers to the two distributions,  $E_j^{(k)}$  is the expected value in the bin  $j$  with variance  $\sigma_{E_j^{(k)}}^2$ ,  $N$  is the total number of bins considered. This statistic follows a  $\chi^2$  distribution with  $N - 1$  degrees of freedom. For unweighted histograms,  $E_j^{(k)}$  is the expected frequency count in bin  $j$  and  $\sigma_{E_j^{(k)}}^2 = E_j^{(k)}$ ; in general,  $E_j^{(k)}$  and  $\sigma_{E_j^{(k)}}^2$  can be calculated by pooling together the data from the two populations/distributions, weighting them according to the fraction of the total numbers of observations (for unweighted histograms) or of the total weights  $W^{(k)}$  (for weighted histograms) for each distribution.

In the case of D or L distribution, in order to increase the test strength, we pooled together consecutive bins (eventually, with the previous or following one) for bins with expected values (in at least one of the two distributions) less than a threshold; this threshold was set at 25 times the average number of spots in a trajectory. After this, every considered bin  $j$  had at least such expected value.

Each experiment was independently repeated at least twice, as indicated in detail in each figure caption or in the relative methods along with the  $p$  values obtained.

# Appendix A FLUOROLABELLING OF THE PPTASE-RELATED CHEMICAL TAGS: COMPARATIVE STUDY OF DIFFERENT MEMBRANE RECEPTORS AND DIFFERENT FLUOROPHORES IN THE LABELLING REACTIONS

---

The choice of the right labelling strategies to monitor molecules of interest in living specimens represents a focal point when planning imaging measurements. In particular, the set-up of SMI experiments requires fluorophores with peculiar photophysical properties as high photostability, brightness, emissions in a wavelength range where autofluorescence is low, possibly the ability to photoactivate or to photoswitch [245]. Accordingly, several novel classes of organic dyes have been developed in the last years [246]–[248], along with the parallel development of chemical tags [249]–[251] or alternative strategies [252] to achieve labelling of membrane and intracellular proteins with the desired organic dye. Despite the recognized advantages offered by these methodological approaches, there are still challenges to overcome. The most notable is probably non-specific interactions of the dyes with lipid bilayers, which can cause both alteration of labelling specificity and generation of false signals due to the fluorophore attachment to the plasma membrane [253]. Therefore, the choice of the correct fluorophores for SMI experiments typically benefits from, and often requires, a preliminary step of optimization. For example, considerations about the physiological expression level of the protein to be labelled, and to what extent its conjugation to a peculiar fluorophore can produce a signal higher than the background must be taken into account. Similarly, fluorophores need to be chosen depending on the experimental setups available in the microscope. An interesting report, using a SNAP-tag fusion construct of the EGF receptor, showed that not all dyes are suitable for the same purposes, because of their different photostability and specificity in the conjugates required for SNAP-tag labelling [254]. Another group screened nine different fluorophores to understand the best fluorophores-lipid combination to study changes in the conformation of proteins embedded in lipid vesicles with SM resolution [255]. In the last years, our group has exploited chemical tags derived from the acyl and peptidyl carrier proteins (ACP and PCP), applied to the labelling of neurotrophins and their receptors, acting on the purified protein and in a living cell context, respectively [160], [168], [169], [205]. This is also the labelling strategy presented and used in this thesis (see paragraph 1.4.1.1). Using the same strategy reported here for neurotrophin receptors, we also achieved the first fluorophore labelling with definite stoichiometry for the Nerve Growth Factor (NGF) [168], [172], [256].

In this appendix, I report the rational optimization process that guided our experimental choices, some of which appear in the previous chapters, as for example the use of Abberior635P in the single-step photobleaching experiment (see paragraph 1.4.1.3, Fig. 2.10 and [169], [205]). In particular, the experiments reported in the following paragraph focus on two different aspects related to chemical tag labelling. First, we asked what is the performance of the same chemical tag when this is fused to structurally or functionally different single-pass transmembrane receptors; accordingly, we compared the labelling performance of a S6 tag fused to the N-terminal sequences of TrkA, P75<sup>NTR</sup> and VEGFR2 receptors. Second, we analyzed how the labelling of a single membrane receptor is influenced by the use of different CoA-fluorophore conjugates in the labelling reaction, by testing eight different CoA-fluorophore substrates for labelling of S6-TrkA receptor.

---

This appendix presents experimental data contained in the manuscript *“Fluorolabelling of the PPTase-related chemical tags: comparative study of different membrane receptors and different fluorophores in the labelling reactions”* with authors **R. Amodeo\***, D. Convertino, M. Calvello, L. Ceccarelli, F. Bonsignore, C. Ravelli, A. Cattaneo, C. Martini, S. Luin, S. Mitola, G. Signore, L. Marchetti. Under revision on Frontiers Molecular Biosciences. Experiments and data analysis shown in the appendix were performed by Rosy Amodeo, Giovanni Signore and Laura Marchetti, with contributions from other coauthors. S6-VEGFR2 construct was given by the group of Prof. Stefania Mitola (Department of Molecular and Translational Medicine, University of Brescia). All CoA-derivatives used were provided by G. Signore (Fondazione Pisana per la Scienza Onlus, Pisa).

## A.1 COMPARATIVE QDOT- AND FLUOROPHORE- LABELLING OF DIFFERENT S6-TAGGED MEMBRANE RECEPTORS

TrkA, VEGFR2 and P75<sup>NTR</sup> are single-pass transmembrane receptors differing at the structural and functional levels. TrkA and VEGFR2 belong to the family of receptor tyrosine kinases (RTKs) [1], while P75<sup>NTR</sup> belongs to the family of tumor necrosis factor receptors (TNFRs) [257] (Fig A.1 A). Also, TrkA and p75<sup>NTR</sup> are master regulators of the neurotrophic responses in neuronal cells (see paragraph 1.2) [182], while VEGFR2 is a pro-angiogenic receptor of endothelial cells (see paragraph 1.3) [258]. From the chemical labelling perspective, their ECDs have different lengths, with p75<sup>NTR</sup> displaying the shortest and VEGFR2 the longest distance from cell surface. Cloning of the S6 tag sequence at the ECD of the three of them allowed for their labelling and imaging with SM resolution on the cell surface in living cells (see chapter 2 and [169], [205]). This labelling strategy has always given good performance for applications in which cells are directly imaged after the labelling reaction, as we can observe in Fig. A.1: we measured a significant higher number of moving spots in cell positive for ACP-TrkA and S6-TrkA receptors (see paragraph 1.4.1.1.) respect to cells not expressing them.

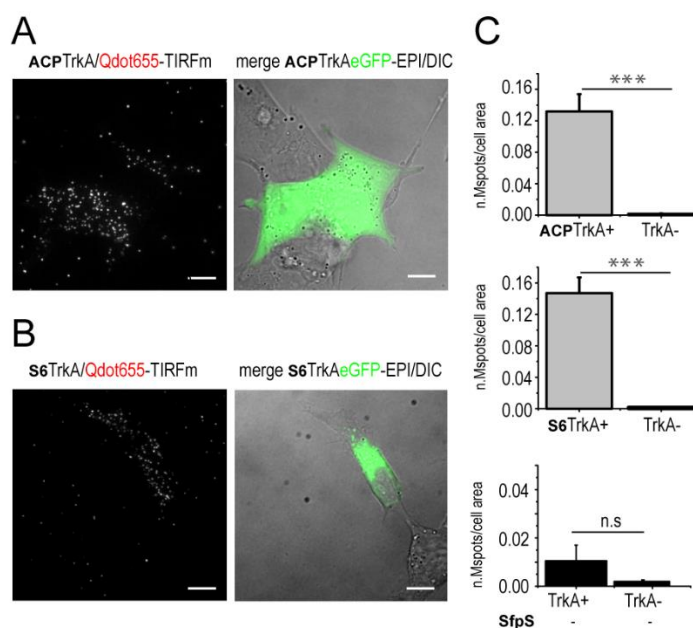


**Figure A.1.** On the left, typical TIRF images of Qdot655 and corresponding merge of green epifluorescence (EPI) and DIC images of SH5Y5Y cells expressing human S6-tagged TrkA (A) and rat ACP-tagged TrkA (B), carrying also an EGFP directly fused to the receptor (A) or coexpressed by the same plasmid (B). The images show the presence of Qdot-labelled receptor spots selectively on EGFP positive cells; scale bar: 10  $\mu$ m. C) quantification of the average receptor spot density, calculated as the number of moving spots (n.Mspots) at cell surface divided by the cell area, for: top, cell expressing ACPTrkA (ACPTrkA+, n=14 cells) and cells not expressing ACPTrkA (ACPTrkA-, n=14 cells); middle and bottom, cells expressing [(S6)TrkA+] and cells not expressing S6TrkA [(S6)TrkA-], in presence (S6TrkA+, n=24 cells; S6TrkA-, n=24 cells) and absence (TrkA+, n=13 cells; TrkA-, n=13 cells) of SFP Synthase. n.s.: non-significant at the 0.05 level, \*\*\* P<0.001 according to One-Way Anova test (A) and Mann-Whitney test (B).

Here, we compared how the same labelling reactions perform on these three moieties, considering also their different exposure from the cell membrane, which may be relevant for enzymatic recognition of the tag. S6-tagged TrkA, P75<sup>NTR</sup> and VEGFR2 were expressed in SHSY5Y cells, and S6 tag was either biotinylated and then coupled to streptavidin-coated Qdots, or directly conjugated to Alexa647 [168]. In both cases, labelled cells were quantitatively analysed by TIRF microscopy. We found a significant, ~ 7- to 10- fold higher fluorescence signal for both labelling reactions on p75<sup>NTR</sup> compared to TrkA and VEGFR2 expressing cells (Fig A.2 C). This may possibly be due to a lower surface abundance of RTKs (TrkA and VEGFR2) with respect to TNFRs (p75<sup>NTR</sup>). This in turn may depend on different expression levels for P75<sup>NTR</sup> and the RTKs. However, we worked in transient overexpression conditions, obtaining a comparable good expression for all three constructs (Fig A.3). We thus do not exclude that there may be also a relevant difference between the relative localization of the receptors, caused *e.g.* by the fact that a considerable amount of membrane RTKs might reside in early/recycling endosomes proximal to the membrane bilayer, where they are less available for the PPTase labelling reaction [259]. These considerations are particularly important for TrkA and p75<sup>NTR</sup> receptors, which have been known to cooperate to transduce neurotrophin signals [260]. When thinking on possible complexes involving the two receptors in neuronal cells [168], it should be considered that there may be different relative levels of p75<sup>NTR</sup> versus TrkA available for neurotrophin binding.

In any case, the previous data indicate that labelling by PPTase enzymes on cell surface receptors is not limited by the length of the ECD, provided that the S6 tag is fused at its distal portion from the membrane; indeed, p75<sup>NTR</sup> ECD is the shortest one used in our experiments (Fig A.2 A), but is also the one displaying the highest amount of labelled moieties. Surely, we have a lower limit of 230 amino acids on the ECD length and do not take possible ECD curvatures into account; however, successful S6-labelling previously reported for constructs of the Atypical Receptor CCRL2, whose extracellular portion is long 43 amino acids, suggests that this limit can be further scaled down [261].

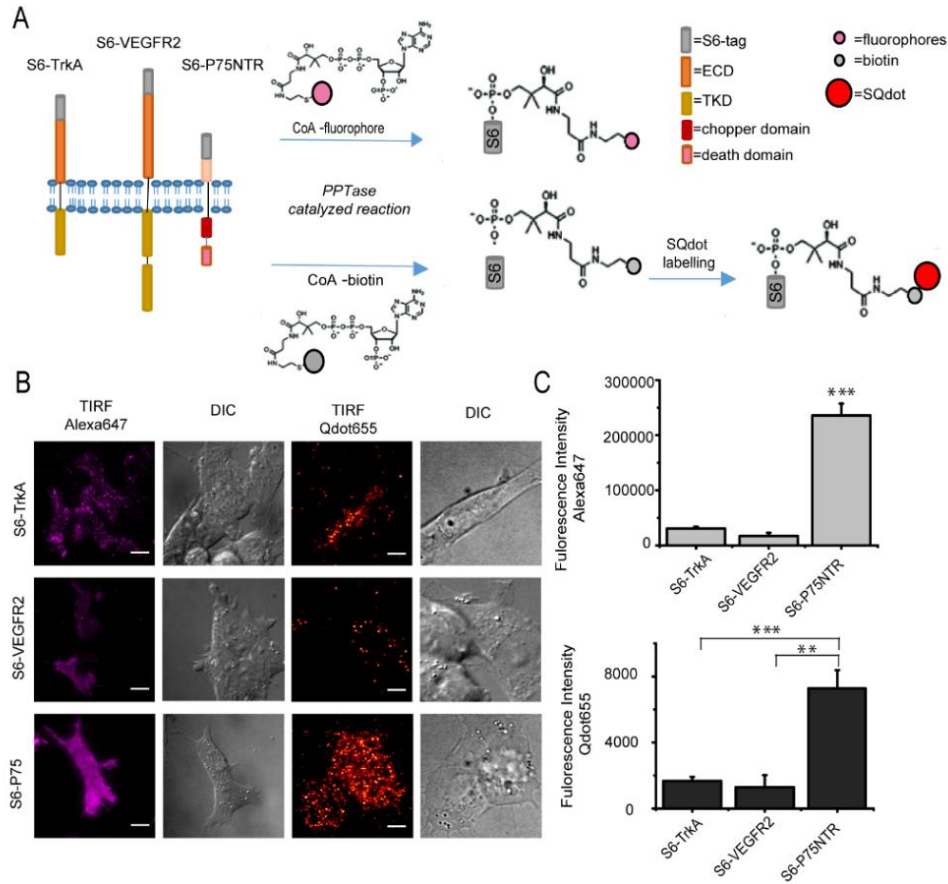


**Figure A.2.** **A)** Scheme of the PPTase-based labelling of S6-tagged TrkA, VEGFR2 and P75<sup>NTR</sup> receptors by CoA-conjugates. S6 tag exhibits the hydroxyl group of a serine residue recognized by the PPTase. Top: conjugation of the PPant arm of CoA-fluorophore conjugate at serine -OH group; bottom: conjugation of the PPant arm of CoA-biotin at serine -OH group; biotinylation precedes the labelling step with streptavidin-coated Qdots (S-Qdot). **B)** TIRF and corresponding DIC microscopy images of SHSY5Y cells expressing S6-TrkA (top), S6-VEGFR2 (middle) and S6-P75<sup>NTR</sup> (bottom), after fluorolabelling by PPTases. On the left, S6-tagged receptors labelled with 500 nM CoA-Alexa647; on the right, labelling with 10 nM S-Qdot; scale bar: 10 μm. **C)** Quantification of labelling efficiency of experiments like the ones shown in panel B. Top: plot of mean fluorescence intensity (±s.e.m.) of Alexa647-labelled S6-TrkA (n=49 cells), S6-VEGFR2 (n=7 cells) and S6-P75<sup>NTR</sup> (n=80 cells). Bottom: plot of mean fluorescence intensity (±s.e.m.) of S-Qdot-labelled S6-TrkA (n=17 cells), S6-VEGFR2 (n=6 cells) and S6-P75<sup>NTR</sup> (n=18 cells). \*\*\* P<0.001, \*\* P<0.01 following one-way ANOVA test, with Bonferroni's comparison of means.

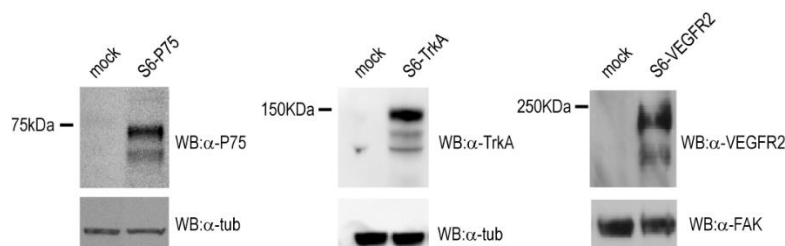


**Figure A.3.** Western blot of SHSY5Y cells transduced with S6-P75<sup>NTR</sup> or S6-TrkA and of CHO cells transduced with S6-VEGFR2; transgene expression was induced adding 1 μg/ml doxycycline to the cell medium; mock samples are shown for comparison [1]. Cell lysates were run on an SDS-PAGE, transferred to a PVDF membrane and blotted with anti-P75<sup>NTR</sup>, anti-TrkA and anti-VEGFR2 antibodies, respectively.

Membranes were stripped and re-blotted using an anti-tubulin antibody for S6-P75<sup>NTR</sup> and S6-TrkA, and anti-FAK for S6-VEGFR2, as loading controls.

## A.2 COMPARATIVE STUDY OF S6-TRKA LABELLING BY DIFFERENT COA-FLUOROPHORE SUBSTRATES IN THE PPTASE LABELLING REACTION

To understand the effect of different fluorophore dyes on S6 tag labelling efficiency, we screened the labelling performance of S6-tagged TrkA in living cells by eight different CoA-fluorophores, whose main photophysical features appear in Table A.2.1. SHSY5Y cells were either left untreated or transduced with a lentiviral vector carrying S6-TrkA, whose expression was induced adding 1  $\mu\text{g/ml}$  doxycycline to the cell medium for 24 hours [168]. We first investigated the level of non-specific interaction of the different CoA-fluorophore substrates with cells not expressing S6-TrkA receptor [254]; cells were incubated with 500 nM of each fluorophore for the same time required for SFPS labelling and were imaged by TIRF microscopy (Fig A.4). Results, shown as mean intracellular fluorescence intensity normalized to the relative cell autofluorescence intensity, show that all green fluorophores (CoA-Abberior488, CoA-Alexa488, CoA-Atto488) and two of the far-red fluorophores tested (CoA-Abberior635STAR-P, CoA-Alexa647) show negligible levels of non-specific internalization or interaction with cells (Fig A.4). Conversely, we detected appreciable levels of fluorescence on cells incubated with CoA-Atto550 and CoA-Alexa568, and a  $\approx$  4-fold increase of cellular fluorescence for cells incubated with CoA-Atto633 (Fig A.4). We argue that, for the Atto550 and Atto633 cases, this unspecific signal is a direct consequence of the unspecific interaction of the fluorophore *per se* with cell membranes, as reported by other studies [253], [254]. Note that these two fluorophores bring a net positive charge in physiological conditions (Table A.1), which could promote adhesion to cell membrane. As for CoA-Alexa568, given its low interaction factor with membranes [253], we hypothesize that other mechanisms depending on Alexa568 conjugation to CoA may account for the observed unspecific intracellular signal.

Fluorophore	Excitation wavelength (nm)	Emission wavelength (nm)	$\epsilon$ ( $\text{M}^{-1} \text{cm}^{-1}$ )	Quantum Yield	Net charge at pH7.4	Mass added to the protein upon S6 conjugation (g/mol)
<b>Abberior 488</b>	501	524	86000	0.89	-2	1133.6
<b>Alexa 488</b>	495	519	73000	0.92	-3	981
<b>Atto 488</b>	501	523	90000	0.80	-1	1405
<b>Alexa 568</b>	578	603	88000	0.69	-2	1130
<b>Atto 550</b>	554	576	120000	0.80	+1	1154
<b>Abberior 635P</b>	633	653	75000	0.92	-1	1681
<b>Alexa 647</b>	650	665	270000	0.33	-3	1493
<b>Atto 633</b>	629	657	130000	0.64	+1	1112

**Table A.1.** List of organic dyes investigated in our study.

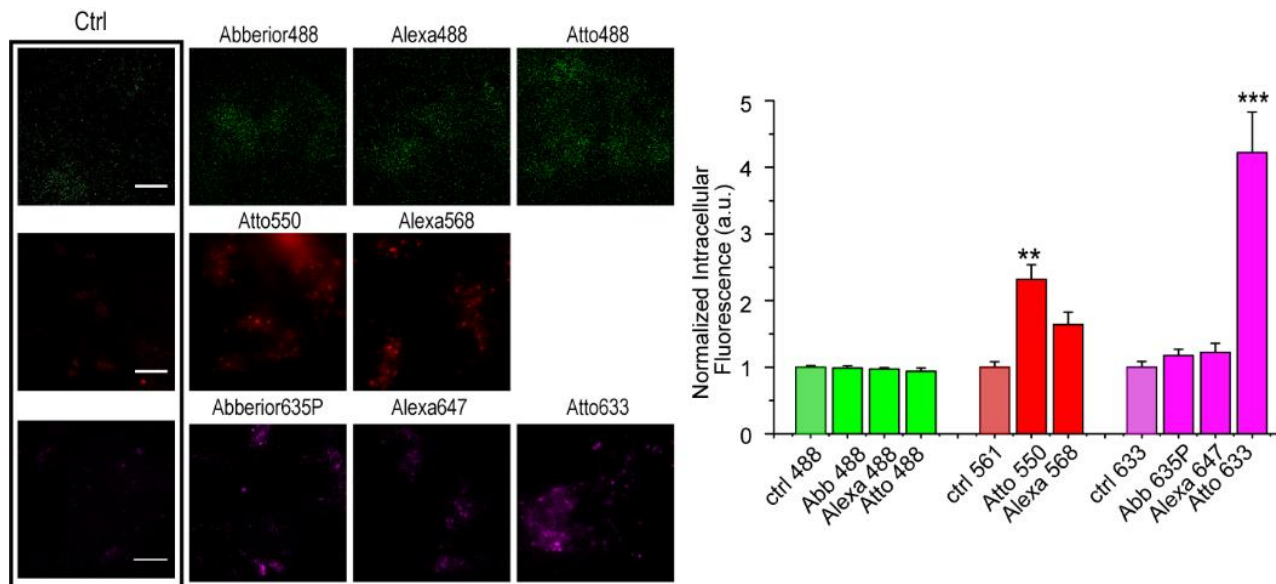
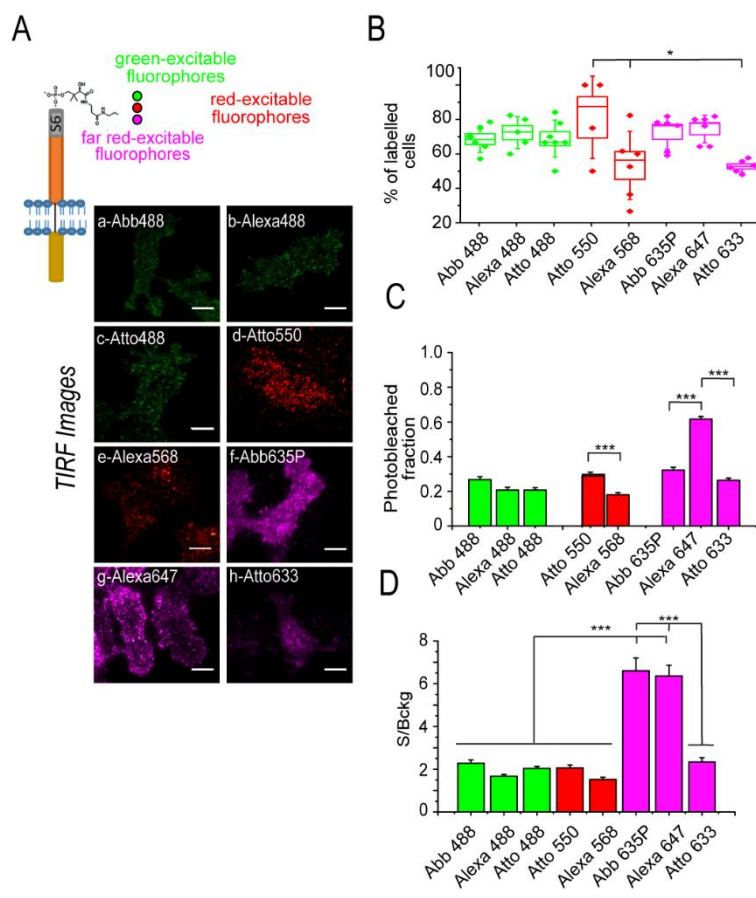


**Figure A.4.** Representative epifluorescence images of SHSY-5Y cells not transduced with S6-TrkA construct, incubated with 500 nM of each CoA-fluorophore for 30 min at 37°C. On top, the box highlights the intensity images derived for cells not incubated with any CoA-dye and acquired at the same microscope set-up. Scale bar: 10  $\mu$ m. Below, the corresponding quantification of intracellular fluorescence intensity (mean $\pm$ s.e.m.) of non-transduced SHSY5Y cells incubated with the eight different CoA-fluorophores, normalized for cell autofluorescence intensity (ctrl) in the same emission channel, to which each fluorophore was compared (n=5 fields, comprising at least 20 cells for each sample). \*\*\* P<0.001, \*\*P<0.01 following one-way ANOVA test, with Bonferroni's comparison of means.

We next performed the full labelling reaction on S6-TrkA transduced cells (Fig A.5 A) (see methods in paragraph 4.11) and evaluated the percentage of labelled versus total cells in the analyzed fields for the eight fluorophores (Fig A.5 B). We observed high labelling percentages for all CoA-fluorophores tested, mostly ranging from  $\approx$ 60 to  $\approx$ 80%. However, for Alexa568, Atto550 and Atto633, we found that the number of labelled cells were slightly lower or displayed higher variability, when compared to the other samples; this could be due to the non-specific internalization of the CoA-fluorophore described above, competing or interfering with the labelling performance. On similar samples, we determined the photostability of each analyzed fluorophore when conjugated to S6-TrkA: we measured the photobleached fraction after a 500-frame series for each fluorophore (Fig A.5 C), by averaging the value  $[1-(I_{\text{post}}/I_{\text{pre}})]$  obtained for 5 different cells in different selected fields ( $I_{\text{post}}$  and  $I_{\text{pre}}$  are the mean intensity of the cell in the last and first frame of a 500-frame time serie of the selected field, respectively). We concluded that, in our experimental conditions, all green-excitable fluorophores display similar bleaching. In the red region, performance of Atto550 is by far superior to that of Alexa568. Alexa647 shows significantly more extensive degradation than the two other far-red excitable fluorophores.

Finally, we evaluated the signal to background ratio (S/Bckg) for each fluorophore (Fig A.5 D): this parameter was empirically defined as the ratio of cell specific signal versus signal stemming from fluorophores not-specifically adhered to the glass, the latter being an unavoidable event occurring during PPTase labelling reactions. In these conditions, we found that only Abberior635P and Alexa647 display S/Bckg significantly higher than the other

ones. Overall, these data indicate that Abberior635P is the best candidate for experiments for SMI of TrkA receptor, explaining the choice of this fluorophore in previous experiments [205]. Indeed, this fluorophore ensures optimal labelling efficiency and signal to background ratio while having relatively low photobleaching percentage and non-specific cell internalization. We do not exclude that, for labelling of other receptors displaying considerably higher membrane densities, as is the case of p75<sup>NTR</sup> (Fig A.1), other fluorophores may also be suitable, pointing to the need to optimize labelling procedures in a case-by-case manner.



Bonferroni's comparison of means.

Despite a recent work described some limits reported for this technique in protocols involving cell detachment by scraping after labelling [169], our data confirm that the employment of chemical tags in PPTase catalyzed reactions is highly suitable for the imaging of membrane proteins directly after the labelling reaction; the use of this method after optimization for the chosen fluorophore (Fig. A.4 and Fig. A.5) delivers an optimal performance in terms of specificity, which, at least for the TrkA case, is shared from the long versions of these tags, like ACP, to the smaller ones like S6 tag (Fig. A.1).

In conclusion, we propose a systematic approach that may serve as a guideline for the chemical biology community to allow a robust, quantitative evaluation of fluorolabelling efficiency and behavior of chemical tags in high sensitivity microscopy setups.

# Appendix B AN OPTIMIZED PROCEDURE TO SCALE UP SAMPLING IN SMI EXPERIMENTS

Research in the biomedical field represents a fundamental mean to unveil causes of various biological phenomena and solutions to different biological questions, as well as a powerful method to develop medicines and therapies to treat diseases. Experimental procedures in biomedicine includes competences in biological, chemical and physical fields. The importance of the scientific validation in biological methods as we understand it today dates back to Galileo Galilei and its “Scientific method”, with which we assist for the first time to the appearance of the modern word of “experiment”. The bases of the scientific method are currently used in scientific field: science is based on observations, formulation of a hypothesis that can be verified with experiments; the result of an experiment must be repeatable and verified before assuming a conclusion. The repeatability of an experiment is in fact a critical point of this approach, because changing experimental conditions and/or operators could modify the final result; for this reason sampling in biological field is a fundamental point to consider. Furthermore, when you want to compare different samples or treatments, you need to maintain equal experimental conditions for all of them, in order to exclude that differences in results are due to any change in them. For the experiments reported in this thesis, most of which were performed in living cell systems, some crucial aspects to ensure reproducibility of the experiments were: i) the time duration of cell starvation, that corresponds to a period of nutrient deprivation responsible for the increase of receptors exposition at plasma membrane; the comparison among cells with similar time of starvation avoid differences caused by difference in constitutive processes; ii) the time required for transgene expression: this corresponds to the time required for a transgene to be expressed by the cell in which it is transfected or transduced with the viral vector (see paragraphs 4.2 and 4.4), and it is important to control it to avoid to compare different experiments in which the protein levels are different among each other. However, for the SMI experiments in particular, there was another crucial aspect to control. Differently from the acquisition of targets genetically-fused to fluorescent proteins, a SMI measure of membrane proteins tagged with chemical tags requires an additional time for the labelling reaction. In detail, for the PPTase labelling system (see Paragraphs 4.12, A.1), cells must be incubated at least 30 minutes with an enzymatic reaction that ensures the conjugation of the dye with the target protein before imaging can start. Furthermore, several wash steps must be performed after labelling to remove the excess of free fluorophore, also in light of its non-specific adhesion to the glass (Paragraph A.2). It is also important that labelled and washed cell samples are imaged with the same timing at the microscope. Indeed, as only the membrane pool of receptors is labelled, it is important that the impact of

membrane turnover is controlled during the experiment. This practically means that a labelled dish cannot be prepared with great advance with respect to imaging, otherwise the constitutive recycling processes will deplete the labelled membrane pool and also likely influence its lateral mobility. These experimental needs unavoidably limit the number of samples/replicates that can be processed during a day (thus reducing the sampling of the experiment) or the possibility to compare different samples in the same condition during a day (thus impairing the reproducibility).

During my thesis work, I optimized an experimental procedure that ensures the maximization of samples that can be labelled and imaged in a day, thus ensuring evaluation of as many samples as possible in the same experimental conditions. This optimized procedure was adopted in the work described in thesis (see Chapter 2: Figures 2.1, 2.2, 2.5, 2.8, 2.12 and 2.14 and [205]) and in others in which I collaborated [169]. In this Appendix, I report two examples of this procedure, applied to: i) the study of membrane dynamics of TrkA-wt and -K547N in response to pharmacological treatments on actin cytoskeleton, as reported in paragraph 2.3 and [205]; ii) the study of the membrane dynamics of p75<sup>NTR</sup> in response to pharmacological treatments affecting the content of membrane cholesterol [169].

---

*This appendix presents the optimization of experimental procedures, entirely developed by Rosy Amodeo.*

## B.1 SCHEMATIC TIMELINE FOR INVESTIGATION OF TRKA-WT AND TRKA-K547N

### MEMBRANE DYNAMICS IN RESPONSE TO ACTIN CYTOSKELETON ALTERATIONS.

This section presents details for experiments whose results are reported in paragraph 2.3, figures 2.11 and 2.12. To perform those experiments, as schematized in Fig. B.1, I devised a protocol in which the labelling of each WillCo dish plate is postponed with respect to the previous one, in a way that biotin-addition reaction in a dish overlaps temporally with the Qdot labelling, washing and imaging steps of the previous one. This allows sparing time, and finally analyzing a higher number of samples, with respect to an experimental protocol in which labelling of the a dish follows the end of imaging of the previous one. Of course, this protocol benefits from the presence of two users, one at the microscope and the other one performing the scheduled labelling reactions. In alternative, one user can work alone if the labelling mixes are prepared at most ten minutes before the use and kept on ice in absence of the SFP Synthase, which is supplemented to the mix immediately before its addition to cells. The application of this protocol allowed me to process about eight WillCo dishes (w1 in Fig. B.1) in 6 hours, while if I would have treated samples independently, putting them in starvation at the same time, I would have needed double the time to complete the experiment. Furthermore, in the latter case I would have compared samples with different time of starvation, meaning that the experimental conditions were not maintained. Contrariwise, if I would have put each WillCo in starvation medium one at the time, it would not have been possible to acquire all these samples during the same day.

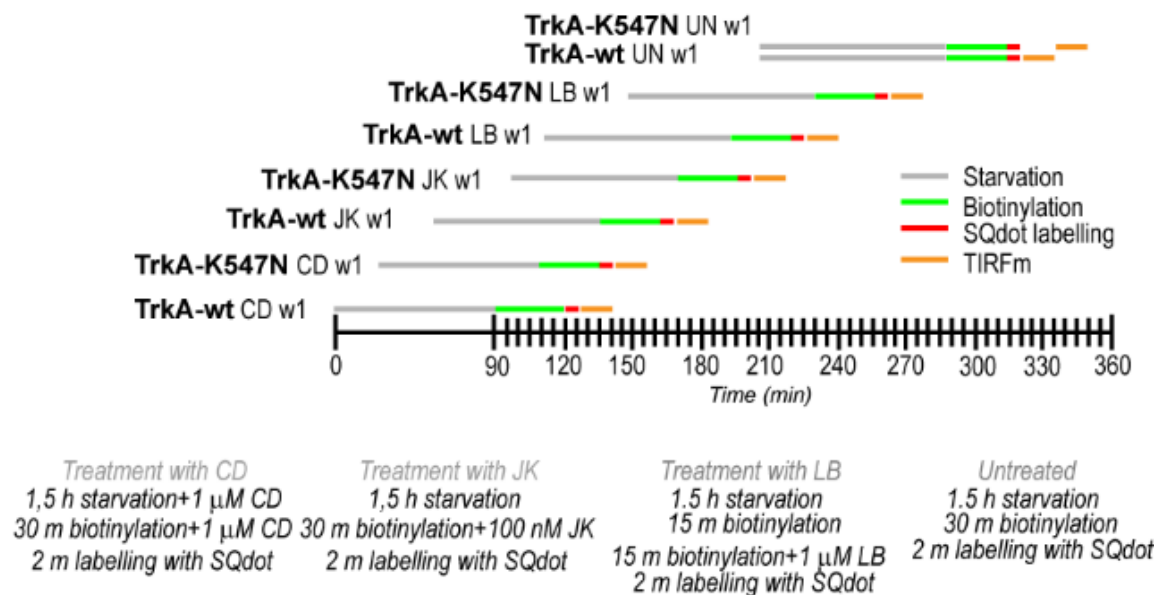


**Fig. B.1.** Schematic timeline of a SMI experiment in which we compare TrkA-wt and TrkA-K547N membrane dynamics in response to CD (Cytocalasin D) and LB (Latrunculin B), which depolymerize the actin cytoskeleton, and in response to JK (Jasplakinolide), which on contrary promotes actin synthesis; UN: untreated dish. w1 indicates WillCo number 1 for each treatment; here we reported only w1 to simplify

the experimental scheme. The time between 0 and 90 minutes is the starvation period for the first processed w1. Below the timeline, details of corresponding reaction mixes are reported. The time duration of TIRF imaging was always 15 minutes.

## B.2 SCHEMATIC TIMELINE FOR INVESTIGATION OF p75<sup>NTR</sup> MEMBRANE DYNAMICS IN RESPONSE TO MEMBRANE CHOLESTEROL MODULATION.

This section presents details for experiments on the different membrane partitioning, in response to NGF stimulation, of p75<sup>NTR</sup> in its wild-type form (wt p75<sup>NTR</sup>) and in a mutated form (mut p75<sup>NTR</sup>) bearing some mutations at the juxtamembrane and transmembrane domains, as reported in [169]. Here, I describe the optimized protocol for measuring, by SPT, the changes in membrane diffusivity for both constructs in SKN-BE(2) cells after membrane cholesterol modulation with: i) overnight incubation with mevastatin (causing cholesterol depletion) prior to the labelling reaction or ii) 30-minute incubation with cholesterol:Methyl- $\beta$ -cyclodextrin (M $\beta$ CD) plus free cholesterol (causing cholesterol overload), during the labelling reaction. Ligand stimulation was performed by addition of 150 ng/ml NGF in the cell medium prior to TIRF imaging. To perform this experiment, as schematized in Fig. B.2, I devised a protocol in which the labelling of each WillCo dish started about 10 minutes before the end of the labelling reaction of the previous one. In this case as well, the protocol benefits from the presence of two users but one user can work alone, provided that the labelling mixes are prepared before and kept on ice in absence of the SFP Synthase, which is supplemented immediately before its addition to cells. The application of this protocol allowed us to acquire 12 WillCo dishes in about 5 hours; on the contrary, the separate preparation and acquisition of each sample would have needed at least 9 hours for completing the experiment.

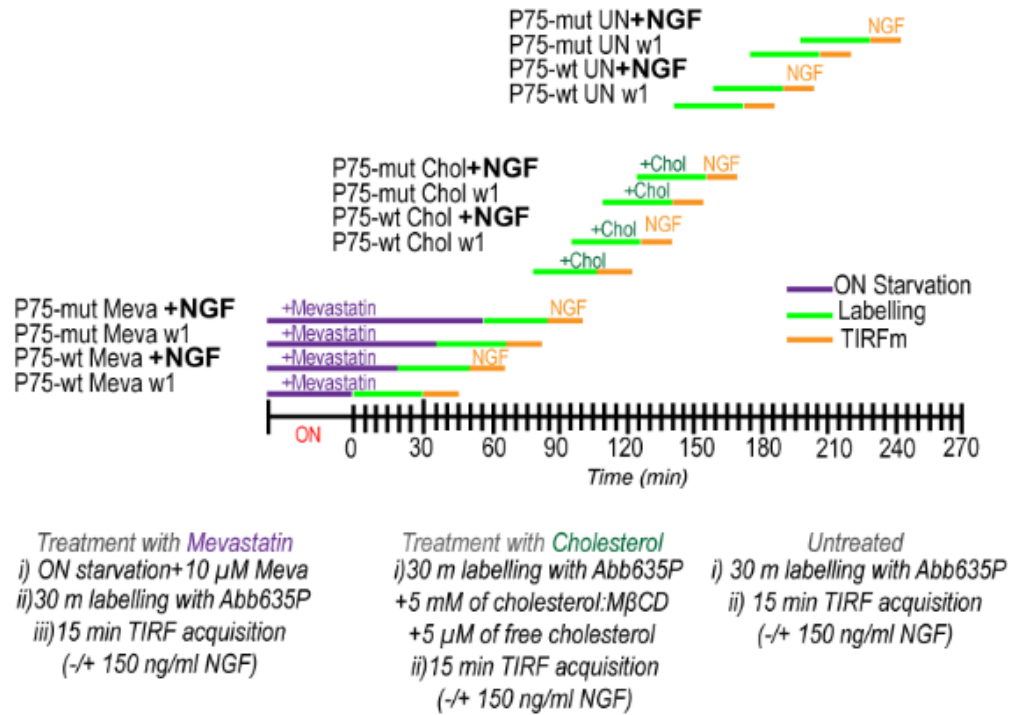


**Fig. B.2.** Schematic timeline of a SMI experiment made on wt P75<sup>NTR</sup> and mut P75<sup>NTR</sup> in response to 10  $\mu$ M mevastatin (Meva) or 5mM cholesterol: MbCD + 5  $\mu$ M free cholesterol (Chol), in the presence or absence of 150 ng/ml NGF during the imaging step, which lasted 15 minutes. UN indicates the untreated sample, ON the overnight starvation and w1 indicates the WillCo number 1 for each treatment; here we reported only w1 to simplify the experimental scheme. Bottom: details of corresponding reaction mixes.

# BIBLIOGRAPHY

- 
- [1] S. R. Hubbard and W. T. Miller, "Receptor tyrosine kinases: mechanism of activation and signalling," *Curr. Opin. Cell Biol.*, vol. 19, no. 2, pp. 117–123, 2008.
  - [2] M. A. Lemmon and J. Schlessinger, "Cell signaling by receptor tyrosine kinases," *Cell*, vol. 141, no. 7, pp. 1117–1134, 2010.
  - [3] P. Blume-Jensen and T. Hunter, "Oncogenic kinase signalling : Abstract : Nature," *Nature*, vol. 411, no. 6835, pp. 355–365, 2001.
  - [4] G. Giamas *et al.*, "Kinases as targets in the treatment of solid tumors," *Cell. Signal.*, vol. 22, no. 7, pp. 984–1002, 2010.
  - [5] L. M. McDonnell, K. D. Kernohan, K. M. Boycott, and S. L. Sawyer, "Receptor tyrosine kinase mutations in developmental syndromes and cancer: Two sides of the same coin," *Hum. Mol. Genet.*, vol. 24, no. R1, pp. R60–R66, 2015.
  - [6] S. C. Robertson, J. A. Tynan, and D. J. Donoghue, "RTK mutations and human syndromes - When good receptors turn bad," *Trends Genet.*, vol. 16, no. 6, pp. 265–271, 2000.
  - [7] L. K. Shawver, D. Slamon, and A. Ullrich, "Smart drugs: Tyrosine kinase inhibitors in cancer therapy," *Cancer Cell*. 2002.
  - [8] F. Grimminger, R. T. Schermuly, and H. A. Ghofrani, "Targeting non-malignant disorders with tyrosine kinase inhibitors," *Nature Reviews Drug Discovery*. 2010.
  - [9] M. Kelley, "Learning to play the game of unhappy families: Sympathetic reading and sentimental ownership in 'Uncle tom and little eva,' a Card game adaptation of uncle tom's cabin," *J. Midwest Mod. Lang. Assoc.*, vol. 45, no. 2, pp. 127–151, 2012.
  - [10] R. T. Bossi *et al.*, "Crystal structures of anaplastic lymphoma kinase in complex with ATP competitive inhibitors," *Biochemistry*, vol. 49, no. 32, pp. 6813–6825, 2010.
  - [11] J. B. Casaletto and A. I. McClatchey, "Spatial regulation of receptor tyrosine kinases in development and cancer," *Nature Reviews Cancer*. 2012.
  - [12] G. Hamilton, B. Rath, L. Klameth, and M. Hochmair, "Receptor tyrosine kinase expression of circulating tumor cells in small cell lung cancer," vol. 2, no. 7, pp. 629–634, 2015.
  - [13] J. Yu *et al.*, "The EPHB6 Receptor Tyrosine Kinase Is a Metastasis Suppressor That Is Frequently Silenced by Promoter DNA Hypermethylation in Non – Small Cell Lung Cancer," pp. 2275–2284, 2010.
  - [14] Y. Indo, "Molecular basis of congenital insensitivity to pain with anhidrosis (CIPA): Mutations and polymorphisms in TRKA (NTRK1) gene encoding the receptor tyrosine kinase for nerve growth factor,"

*Human Mutation*. 2001.

- [15] Z. Du and C. M. Lovly, "Mechanisms of receptor tyrosine kinase activation in cancer," *Mol. Cancer*, vol. 17, no. 1, pp. 1–13, 2018.
- [16] S. Cohen and R. Levi-Montalcini, "Purification and Properties of a Nerve Growth-promoting Factor Isolated from Mouse Sarcoma 180," *Cancer Res.*, 1957.
- [17] G. Carpenter, L. King, and S. Cohen, "Epidermal growth factor stimulates phosphorylation in membrane preparations in vitro [21]," *Nature*. 1978.
- [18] R. Roskoski, "A historical overview of protein kinases and their targeted small molecule inhibitors," *Pharmacol. Res.*, vol. 100, pp. 1–23, 2015.
- [19] M. A. Lemmon and J. Schlessinger, "( ALL STRUCTURES) NIH Public Access," vol. 141, no. 7, pp. 1117–1134, 2011.
- [20] A. Gschwind, O. M. Fischer, and A. Ullrich, "The discovery of receptor tyrosine kinases: Targets for cancer therapy," *Nature Reviews Cancer*. 2004.
- [21] S. R. Hubbard, "Structural analysis of receptor tyrosine kinases," *Prog. Biophys. Mol. Biol.*, vol. 71, no. 3–4, pp. 343–358, 1999.
- [22] E. Li and K. Hristova, "Receptor tyrosine kinase transmembrane domains," *Cell Adh. Migr.*, vol. 4, no. 2, pp. 249–254, 2010.
- [23] A. Ullrich and J. Schlessinger, "Signal transduction by receptors with tyrosine kinase activity," *Cell*. 1990.
- [24] C. W. Ward, M. C. Lawrence, V. A. Streltsov, T. E. Adams, and N. M. McKern, "The insulin and EGF receptor structures: new insights into ligand-induced receptor activation," *Trends Biochem. Sci.*, vol. 32, no. 3, pp. 129–137, 2007.
- [25] W. A. Barton *et al.*, "Crystal structures of the Tie2 receptor ectodomain and the angiopoietin-2-Tie2 complex," *Nat. Struct. Mol. Biol.*, vol. 13, no. 6, pp. 524–532, 2006.
- [26] J. P. Himanen and D. B. Nikolov, "Eph signaling: A structural view," *Trends Neurosci.*, vol. 26, no. 1, pp. 46–51, 2003.
- [27] T. W. J. Gadella and T. M. Jovin, "Oligomerization of epidermal growth factor receptors on A431 cells studied by time-resolved fluorescence imaging microscopy. A stereochemical model for tyrosine kinase receptor activation," *J. Cell Biol.*, vol. 129, no. 6, pp. 1543–1558, 1995.
- [28] A. H. A. Clayton *et al.*, "Ligand-induced dimer-tetramer transition during the activation of the cell surface epidermal growth factor receptor-A multidimensional microscopy analysis," *J. Biol. Chem.*, vol. 280, no. 34, pp. 30392–30399, 2005.
- [29] L. E. Locascio and D. J. Donoghue, "KIDs rule: Regulatory phosphorylation of RTKs," *Trends in Biochemical Sciences*. 2013.

- [30] A. I. Ségaliny, M. Tellez-Gabriel, M. F. Heymann, and D. Heymann, "Receptor tyrosine kinases: Characterisation, mechanism of action and therapeutic interests for bone cancers," *J. Bone Oncol.*, vol. 4, no. 1, pp. 1–12, 2015.
- [31] G. Gógl, A. P. Kornev, A. Reményi, and S. S. Taylor, "Disordered Protein Kinase Regions in Regulation of Kinase Domain Cores," *Trends Biochem. Sci.*, vol. 44, no. 4, pp. 300–311, 2019.
- [32] J. Beenstock, N. Mooshayef, and D. Engelberg, "How Do Protein Kinases Take a Selfie (Autophosphorylate)?," *Trends Biochem. Sci.*, vol. 41, no. 11, pp. 938–953, 2016.
- [33] S. S. Taylor, A. S. Shaw, N. Kannan, and A. P. Kornev, "Integration of signaling in the kinome: Architecture and regulation of the  $\alpha$  Helix," *Biochim. Biophys. Acta - Proteins Proteomics*, vol. 1854, no. 10, pp. 1567–1574, 2015.
- [34] J. M. M. Mendrola, F. Shi, J. H. H. Park, and M. A. A. Lemmon, "Receptor tyrosine kinases with intracellular pseudokinase domains," *Biochem. Soc. Trans.*, vol. 41, no. 4, pp. 1029–1036, Aug. 2013.
- [35] P. Kinases, R. Playing, B. Kobe, and B. E. Kemp, "Protein Kinase Domain Learn more about Protein Kinase Domain Volume 2," 2010.
- [36] B. Nolen, S. Taylor, and G. Ghosh, "Regulation of protein kinases: Controlling activity through activation segment conformation," *Mol. Cell*, vol. 15, no. 5, pp. 661–675, 2004.
- [37] M. Huse and J. Kuriyan, "The conformational plasticity of protein kinases.," *Cell*, 2002.
- [38] S. R. Hubbard, "Juxtamembrane autoinhibition in receptor tyrosine kinases," *Nature Reviews Molecular Cell Biology*. 2004.
- [39] T. Pawson, G. D. Gish, and P. Nash, "SH2 domains, interaction modules and cellular wiring," *Trends in Cell Biology*. 2001.
- [40] R. Butti, S. Das, V. P. Gunasekaran, A. S. Yadav, D. Kumar, and G. C. Kundu, "Receptor tyrosine kinases (RTKs) in breast cancer: Signaling, therapeutic implications and challenges," *Molecular Cancer*. 2018.
- [41] C. Wiesmann, M. H. Ultsch, and S. H. Bass, "Nature, 1999, 401, 184.pdf," vol. 401, no. SEPTEMBER, pp. 1–5, 1999.
- [42] C. Wiesmann, G. Fuh, H. W. Christinger, C. Eigenbrot, J. A. Wells, and A. M. De Vos, "Science(10)," vol. 91, pp. 1–10, 1997.
- [43] H. Liu, X. Chen, P. J. Focia, and X. He, "Structural basis for stem cell factor-KIT signaling and activation of class III receptor tyrosine kinases," *EMBO J.*, 2007.
- [44] S. Yuzawa, Y. Opatowsky, Z. Zhang, V. Mandiyan, I. Lax, and J. Schlessinger, "Structural Basis for Activation of the Receptor Tyrosine Kinase KIT by Stem Cell Factor," *Cell*, 2007.
- [45] J. Schlessinger *et al.*, "Crystal structure of a ternary FGF-FGFR-heparin complex reveals a dual role for heparin in FGFR binding and dimerization," *Mol. Cell*, 2000.

- [46] H. Ogiso *et al.*, "Crystal structure of the complex of human epidermal growth factor and receptor extracellular domains," *Cell*, 2002.
- [47] C. L. Corless and M. C. Heinrich, "Molecular Pathobiology of Gastrointestinal Stromal Sarcomas," *Annu. Rev. Pathol. Mech. Dis.*, 2007.
- [48] J. H. Bae, E. D. Lew, S. Yuzawa, F. Tomé, I. Lax, and J. Schlessinger, "The Selectivity of Receptor Tyrosine Kinase Signaling Is Controlled by a Secondary SH2 Domain Binding Site," *Cell*, vol. 138, no. 3, pp. 514–524, 2009.
- [49] J. Griffith *et al.*, "The Structural Basis for Autoinhibition of FLT3 by the Juxtamembrane Domain," *Mol. Cell*, vol. 13, no. 2, pp. 169–178, 2004.
- [50] J. H. Till *et al.*, "Crystal structure of the MuSK tyrosine kinase: Insights into receptor autoregulation," *Structure*, vol. 10, no. 9, pp. 1187–1196, 2002.
- [51] L. E. Wybenga-Groot, B. Baskin, S. H. Ong, J. Tong, T. Pawson, and F. Sicheri, "Structural basis for autoinhibition of the EphB2 receptor tyrosine kinase by the unphosphorylated juxtamembrane region," *Cell*, vol. 106, no. 6, pp. 745–757, 2001.
- [52] L. M. Shewchuk *et al.*, "Structure of the Tie2 RTK domain - Self-inhibition by the nucleotide binding loop, activation loop, and C-terminal tail," *Structure*, vol. 8, no. 11, pp. 1105–1113, 2000.
- [53] G. M. Brodeur *et al.*, "Trk receptor expression and inhibition in neuroblastomas," *Clinical Cancer Research*. 2009.
- [54] C. Miranda, G. Zanotti, S. Pagliardini, C. Ponzetto, M. A. Pierotti, and A. Greco, "Gain of function mutations of RTK conserved residues display differential effects on NTRK1 kinase activity," *Oncogene*, 2002.
- [55] N. V. Sergina and M. M. Moasser, "The HER family and cancer: emerging molecular mechanisms and therapeutic targets," *Trends in Molecular Medicine*. 2007.
- [56] G. Manning, D. B. Whyte, R. Martinez, T. Hunter, and S. Sudarsanam, "Materials and Methods for 'The protein kinase complement of the human genome,'" *Science*, vol. 298, no. December, 2002.
- [57] A. Gentile, L. Lazzari, S. Benvenuti, L. Trusolino, and P. M. Comoglio, "Ror1 is a pseudokinase that is crucial for met-driven tumorigenesis," *Cancer Res.*, 2011.
- [58] J. Boudeau, D. Miranda-Saavedra, G. J. Barton, and D. R. Alessi, "Emerging roles of pseudokinases," *Trends in Cell Biology*. 2006.
- [59] E. Zehiraj and D. M. F. van Aalten, "Pseudokinases-remnants of evolution or key allosteric regulators?," *Current Opinion in Structural Biology*. 2010.
- [60] M. B. Berger, J. M. Mendrola, and M. A. Lemmon, "ErbB3/HER3 does not homodimerize upon neuregulin binding at the cell surface," *FEBS Lett.*, vol. 569, no. 1–3, pp. 332–336, 2004.
- [61] T. Holbro, R. R. Beerli, F. Maurer, M. Koziczak, C. F. Barbas, and N. E. Hynes, "The ErbB2/ErbB3

heterodimer functions as an oncogenic unit: ErbB2 requires ErbB3 to drive breast tumor cell proliferation," *Proc. Natl. Acad. Sci.*, vol. 100, no. 15, pp. 8933–8938, 2003.

- [62] H. Luo *et al.*, "EphB6 -null mutation results in compromised T cell function Find the latest version : EphB6 -null mutation results in compromised T cell function," vol. 114, no. 12, pp. 1762–1773, 2004.
- [63] M. H. Cobb, J. L. Wilsbacher, J. M. English, B. Xu, S. Stippec, and E. J. Goldsmith, "WNK1, a Novel Mammalian Serine/Threonine Protein Kinase Lacking the Catalytic Lysine in Subdomain II," *J. Biol. Chem.*, vol. 275, no. 22, pp. 16795–16801, 2002.
- [64] R. LEVI-MONTALCINI, "Effects of mouse tumor transplantation on the nervous system.," *Ann. N. Y. Acad. Sci.*, 1952.
- [65] G. R. Lewin, "Physiology of the Neurotrophins," *Annu. Rev. Neurosci.*, 1996.
- [66] S. Korsching, "The neurotrophic factor concept: A reexamination," *J. Neurosci.*, vol. 13, no. 7, pp. 2739–2748, 1993.
- [67] M. Vilar and H. Mira, "Regulation of neurogenesis by neurotrophins during adulthood: Expected and unexpected roles," *Front. Neurosci.*, vol. 10, no. FEB, pp. 1–9, 2016.
- [68] J. Baik, "Neurotrophins and neuropathic pain in patients with traumatic brain injury," *Korean J. Pain*, vol. 33, no. 1, pp. 1–2, 2020.
- [69] B. L. Hempstead, "The many faces of p75NTR," *Current Opinion in Neurobiology*. 2002.
- [70] R. Klein, S. Jing, V. Nanduri, E. O'Rourke, and M. Barbacid, "The trk proto-oncogene encodes a receptor for nerve growth factor," *Cell*, 1991.
- [71] R. Levi-Montalcini, "The nerve growth factor 35 years later," *Science (80-. )*, 1987.
- [72] D. M. Holtzman *et al.*, "NIH Public Access," vol. 15, no. 2, pp. 1567–1576, 2009.
- [73] D. R. Kaplan *et al.*, "The trk Proto-Oncogene Product : A Signal Transducing Receptor for Nerve Growth Factor Published by : American Association for the Advancement of Science Stable URL : <http://www.jstor.org/stable/2875484> on The The trk trk Proto-Oncogene Proto-Oncogene Pro," vol. 252, no. 5005, pp. 554–558, 2016.
- [74] D. R. Kaplan, D. Martin-Zanca, and L. F. Parada, "Tyrosine phosphorylation and tyrosine kinase activity of the trk proto-oncogene product induced by NGF," *Nature*, vol. 350, no. 6314, pp. 158–160, 1991.
- [75] H. Munetaka, "REVIEW ARTICLE NGF / TrkA Signaling as a Therapeutic Target for Pain," vol. 16, no. 800, pp. 175–182, 2016.
- [76] A. Kruttgen, S. Saxena, M. E. Evangelopoulos, and J. Weis, "Neurotrophins and neurodegenerative diseases: Receptors stuck in traffic?," *J. Neuropathol. Exp. Neurol.*, vol. 62, no. 4, pp. 340–350, 2003.
- [77] S. Capsoni, C. Tiveron, D. Vignone, G. Amato, and A. Cattaneo, "Dissecting the involvement of tropomyosin-related kinase A and p75 neurotrophin receptor signaling in NGF deficit-induced

- neurodegeneration," *Proc. Natl. Acad. Sci. U. S. A.*, vol. 107, no. 27, pp. 12299–12304, 2010.
- [78] J. A. Hernández, R. C. López-Sánchez, and A. Rendón-Ramírez, "Lipids and Oxidative Stress Associated with Ethanol-Induced Neurological Damage," *Oxidative Medicine and Cellular Longevity*. 2016.
- [79] D. Martin-Zanca, S. H. Hughes, and M. Barbacid, "A human oncogene formed by the fusion of truncated tropomyosin and protein tyrosine kinase sequences," *Nature*, 1986.
- [80] H. Hondermarck, "Neurotrophins and their receptors in breast cancer," *Cytokine and Growth Factor Reviews*. 2012.
- [81] Y. Hayakawa *et al.*, "Nerve Growth Factor Promotes Gastric Tumorigenesis through Aberrant Cholinergic Signaling," *Cancer Cell*, 2017.
- [82] Y. Lei *et al.*, "Gold nanoclusters-assisted delivery of NGF siRNA for effective treatment of pancreatic cancer," *Nat. Commun.*, 2017.
- [83] E. Cocco, M. Scaltriti, and A. Drilon, "NTRK fusion-positive cancers and TRK inhibitor therapy," *Nat. Rev. Clin. Oncol.*, vol. 15, no. 12, pp. 731–747, 2018.
- [84] H. U. G. Weier, A. P. Rhein, F. Shadravan, C. Collins, and D. Polikoff, "Rapid physical mapping of the human *trk* protooncogene (NTRK1) to human chromosome 1q21-q22 by P1 clone selection, fluorescence in situ hybridization (FISH), and computer-assisted microscopy," *Genomics*, vol. 26, no. 2, pp. 390–393, 1995.
- [85] M. Barbacid, "The *Trk* family of neurotrophin receptors," *J. Neurobiol.*, 1994.
- [86] D. O. Clary and L. F. Reichardt, "An alternatively spliced form of the nerve growth factor receptor *TrkA* confers an enhanced response to neurotrophin 3," *Proc. Natl. Acad. Sci. U. S. A.*, 1994.
- [87] D. Martin-Zanca, R. Oskam, G. Mitra, T. Copeland, and M. Barbacid, "Molecular and biochemical characterization of the human *trk* proto-oncogene," *Mol. Cell. Biol.*, vol. 9, no. 1, pp. 24–33, 1989.
- [88] J. C. Arevalo, B. Conde, B. I. Hempstead, M. V. Chao, D. Martín-Zanca, and P. Pérez, "A novel mutation within the extracellular domain of *TrkA* causes constitutive receptor activation," *Oncogene*, vol. 20, no. 10, pp. 1229–1234, 2001.
- [89] L. Zaliauskiene, S. Kang, C. G. Brouillette, J. Lebowitz, R. B. Arani, and J. F. Collawn, "Down-Regulation of Cell Surface Receptors Is Modulated by Polar Residues within the Transmembrane Domain," vol. 11, no. August, pp. 2643–2655, 2000.
- [90] M. L. Franco, K. D. Nadezhdin, S. A. Goncharuk, K. S. Mineev, A. S. Arseniev, and M. Vilar, "Structural basis of the transmembrane domain dimerization and rotation in the activation mechanism of the TRKA receptor by nerve growth factor," *J. Biol. Chem.*, 2020.
- [91] I. Maruyama, "Mechanisms of Activation of Receptor Tyrosine Kinases: Monomers or Dimers," *Cells*, vol. 3, no. 2, pp. 304–330, 2014.
- [92] S. O. Yoon, S. P. Soltoff, and M. V. Chao, "A dominant role of the juxtamembrane region of the *TrkA* nerve

- growth factor receptor during neuronal cell differentiation," *J. Biol. Chem.*, vol. 272, no. 37, pp. 23231–23238, 1997.
- [93] S. Favellyukis, J. H. Till, S. R. Hubbard, and W. T. Miller, "Structure and autoregulation of the insulin-like growth factor 1 receptor kinase," *Nat. Struct. Biol.*, 2001.
- [94] J. C. Arévalo *et al.*, "Cell Survival through Trk Neurotrophin Receptors Is Differentially Regulated by Ubiquitination," *Neuron*, vol. 50, no. 4, pp. 549–559, 2006.
- [95] H. Kaihola, J. Olivier, I. S. Poromaa, and H. Åkerud, "The effect of antenatal depression and selective serotonin reuptake inhibitor treatment on nerve growth factor signaling in human placenta," *PLoS One*, vol. 10, no. 1, pp. 1–15, 2015.
- [96] N. F. Endres, T. Barros, A. J. Cantor, and J. Kuriyan, "Emerging concepts in the regulation of the EGF receptor and other receptor tyrosine kinases," *Trends in Biochemical Sciences*. 2014.
- [97] S. Jing, P. Tapley, and M. Barbacid, "Nerve growth factor mediates signal transduction through trk homodimer receptors," *Neuron*, vol. 9, no. 6, pp. 1067–1079, 1992.
- [98] P. S. Mischel, J. A. Umbach, S. Eskandari, S. G. Smith, C. B. Gundersen, and G. A. Zampighi, "Nerve growth factor signals via preexisting TrkA receptor oligomers," *Biophys. J.*, vol. 83, no. 2, pp. 968–976, 2002.
- [99] F. Ahmed and K. Hristova, "Dimerization of the Trk receptors in the plasma membrane: Effects of their cognate ligands," *Biochem. J.*, vol. 475, no. 22, pp. 3669–3685, 2018.
- [100] S. Sarabipour, K. Ballmer-Hofer, and K. Hristova, "VEGFR-2 conformational switch in response to ligand binding," *Elife*, vol. 5, no. APRIL2016, pp. 1–23, 2016.
- [101] M. L. Grimes *et al.*, "Anexo:CIE-10 Capítulo VII: Enfermedades del ojo y sus anexos - Wikipedia, la enciclopedia libre," vol. 16, no. 24, pp. 7950–7964, 1996.
- [102] Y. Zhang, D. B. Moheban, B. R. Conway, A. Bhattacharyya, and R. A. Segal, "Cell surface Trk receptors mediate NGF-induced survival while internalized receptors regulate NGF-induced differentiation.," *J. Neurosci.*, vol. 20, no. 15, pp. 5671–8, 2000.
- [103] E. C. Beattie, "NGF signals through TrkA to increase clathrin at the plasma membrane and enhance clathrin-mediated membrane trafficking.," *J. Neurosci.*, vol. 20, no. 19, pp. 7325–7333, 2000.
- [104] J. Jullien, V. Guili, L. F. Reichardt, and B. B. Rudkin, "Molecular kinetics of nerve growth factor receptor trafficking and activation," *J. Biol. Chem.*, 2002.
- [105] G. J. Doherty and H. T. McMahon, "Mechanisms of endocytosis.," *Annu. Rev. Biochem.*, 2009.
- [106] P. Paolo, D. Fiore, and P. De Camilli, "Endocytosis and Signaling: Minireview An Inseparable Partnership," *Cell*, vol. 106, pp. 1–4, 2001.
- [107] H. Stenmark, "Rab GTPases as coordinators of vesicle traffic," *Nat. Rev. Mol. Cell Biol.*, vol. 10, no. 8, pp. 513–525, 2009.

- [108] M. Miaczynska *et al.*, “APPL Proteins Link Rab5 to Nuclear Signal Transduction via an Endosomal Compartment view, signal transduction is initiated at the plasma membrane and, via a series of protein-protein interactions and kinase cascades, transmitted through the cytoplasm,” *Cell*, vol. 116, pp. 445–456, 2004.
- [109] D. L. Senger and R. B. Campenot, “Rapid retrograde tyrosine phosphorylation of trkA and other proteins in rat sympathetic neurons in compartmented cultures,” *J. Cell Biol.*, vol. 138, no. 2, pp. 411–421, 1997.
- [110] F. C. Bronfman, O. M. Lazo, C. Flores, and C. A. Escudero, “Spatiotemporal intracellular dynamics of neurotrophin and its receptors. Implications for neurotrophin signaling and neuronal function,” *Handb. Exp. Pharmacol.*, 2015.
- [111] R. B. Campenot, “Local control of neurite development by nerve growth factor Cell Biology : Campenot,” vol. 74, no. 10, pp. 4516–4519, 1977.
- [112] B. L. MacInnis and R. B. Campenot, “Retrograde support of neuronal survival without retrograde transport of nerve growth factor,” *Science (80-. )*, vol. 295, no. 5559, pp. 1536–1539, 2002.
- [113] C. B. Vaegter *et al.*, “NIH Public Access,” vol. 14, no. 1, pp. 1–23, 2013.
- [114] B. Hausott and L. Klimaschewski, “Membrane turnover and receptor trafficking in regenerating axons,” vol. 43, pp. 309–317, 2016.
- [115] M. Terenzio, G. Schiavo, and M. Fainzilber, “Compartmentalized Signaling in Neurons: From Cell Biology to Neuroscience,” *Neuron*, vol. 96, no. 3, pp. 667–679, 2017.
- [116] A. Ciehanover, Y. Hod, and A. Hershko, “A heat-stable polypeptide component of an ATP-dependent proteolytic system from reticulocytes,” *Biochem. Biophys. Res. Commun.*, 1978.
- [117] L. Sun and Z. J. Chen, “The novel functions of ubiquitination in signaling,” *Curr. Opin. Cell Biol.*, vol. 16, no. 2, pp. 119–126, 2004.
- [118] J. Sánchez-Sánchez and J. C. Arévalo, “A review on ubiquitination of neurotrophin receptors: Facts and perspectives,” *International Journal of Molecular Sciences*. 2017.
- [119] V. G. Bhoj and Z. J. Chen, “Ubiquitylation in innate and adaptive immunity,” *Nature*. 2009.
- [120] K. N. Swatek and D. Komander, “Ubiquitin modifications,” *Cell Res.*, vol. 26, no. 4, pp. 399–422, 2016.
- [121] M. J. M. Bertrand *et al.*, “cIAP1 and cIAP2 Facilitate Cancer Cell Survival by Functioning as E3 Ligases that Promote RIP1 Ubiquitination,” *Mol. Cell*, vol. 30, no. 6, pp. 689–700, 2008.
- [122] N. Mailand *et al.*, “RNF8 Ubiquitylates Histones at DNA Double-Strand Breaks and Promotes Assembly of Repair Proteins,” *Cell*, vol. 131, no. 5, pp. 887–900, 2007.
- [123] S. Adhikary *et al.*, “The ubiquitin ligase HectH9 regulates transcriptional activation by Myc and is essential for tumor cell proliferation,” *Cell*, vol. 123, no. 3, pp. 409–421, 2005.
- [124] D. Shi and S. R. Grossman, “Emerging roles of ubiquitin ligases and deubiquitinases in tumorigenesis and

as therapeutic targets Ubiquitin becomes ubiquitous in cancer,” pp. 737–747, 2010.

- [125] G. Wang *et al.*, “K63-linked ubiquitination in kinase activation and cancer,” vol. 2, no. January, pp. 1–13, 2012.
- [126] T. Geetha, J. Jiang, and M. W. Wooten, “Lysine 63 polyubiquitination of the nerve growth factor receptor TrkA directs internalization and signaling,” *Mol. Cell*, vol. 20, no. 2, pp. 301–312, 2005.
- [127] T. Yu *et al.*, “In Vivo Regulation of NGF-Mediated Functions by Nedd4-2 Ubiquitination of TrkA,” *J. Neurosci.*, vol. 34, no. 17, pp. 6098–6106, 2014.
- [128] R. Singh *et al.*, “TRAF4-mediated ubiquitination of NGF receptor TrkA regulates prostate cancer metastasis,” *J. Clin. Invest.*, vol. 128, no. 7, pp. 3129–3143, 2018.
- [129] Y. Takahashi *et al.*, “Ligand-induced downregulation of TrkA is partly regulated through ubiquitination by Cbl,” *FEBS Lett.*, vol. 585, no. 12, pp. 1741–1747, 2011.
- [130] T. Jadhav, T. Geetha, J. Jiang, and M. W. Wooten, “Identification of a consensus site for TRAF6/p62 polyubiquitination,” *Biochem. Biophys. Res. Commun.*, vol. 371, no. 3, pp. 521–524, 2008.
- [131] R. Kuruvilla *et al.*, “A neurotrophin signaling cascade coordinates sympathetic neuron development through differential control of TrkA trafficking and retrograde signaling,” *Cell*, 2004.
- [132] J. P. S. Makkerh, C. Ceni, D. S. Auld, F. Vaillancourt, G. Dorval, and P. A. Barker, “p75 neurotrophin receptor reduces ligand-induced Trk receptor ubiquitination and delays Trk receptor internalization and degradation,” *EMBO Rep.*, vol. 6, no. 10, pp. 936–941, 2005.
- [133] T. Geetha, M. L. Seibenhener, L. Chen, K. Madura, and M. W. Wooten, “Biochemical and Biophysical Research Communications p62 serves as a shuttling factor for TrkA interaction with the proteasome,” vol. 374, pp. 33–37, 2008.
- [134] C. B. F. Thien and W. Y. Langdon, “c-Cbl and Cbl-b ubiquitin ligases: substrate diversity and the negative regulation of signalling responses,” *Biochem. J.*, vol. 391, no. 2, pp. 153–166, 2006.
- [135] M. V. Georgieva, Y. De Pablo, D. Sanchis, J. X. Comella, and M. Llovera, “Ubiquitination of TrkA by Nedd4-2 regulates receptor lysosomal targeting and mediates receptor signaling,” *J. Neurochem.*, vol. 117, no. 3, pp. 479–493, 2011.
- [136] E. Kiris *et al.*, “TrkA In Vivo Function Is Negatively Regulated by Ubiquitination,” *J. Neurosci.*, vol. 34, no. 11, pp. 4090–4098, 2014.
- [137] A. E. Dubin and A. Patapoutian, “Nociceptors: The sensors of the pain pathway,” *Journal of Clinical Investigation*. 2010.
- [138] M. Hirose, Y. Kuroda, and E. Murata, “NGF/TrkA Signaling as a Therapeutic Target for Pain,” *Pain Pract.*, vol. 16, no. 2, pp. 175–182, 2016.
- [139] S. Mardy *et al.*, “Congenital insensitivity to pain with anhidrosis: Novel mutations in the TRKA

- (NTRK1)gene encoding a high-affinity receptor for nerve growth factor," *Am. J. Hum. Genet.*, vol. 64, no. 6, pp. 1570–1579, 1999.
- [140] I. Wilmut, "© 19 9 7 Nature Publishing Group," *Nature*, vol. 385, pp. 810–813, 1997.
- [141] A. Beigelman *et al.*, "Abnormal neutrophil chemotactic activity in children with congenital insensitivity to pain with anhidrosis (CIPA): The role of nerve growth factor," *Clin. Immunol.*, vol. 130, no. 3, pp. 365–372, 2009.
- [142] X. Geng *et al.*, "Novel NTRK1 mutations in Chinese patients with congenital insensitivity to pain with anhidrosis," *Mol. Pain*, vol. 14, 2018.
- [143] S. S. Shaikh *et al.*, "A Comprehensive Functional Analysis of NTRK1 Missense Mutations Causing Hereditary Sensory and Autonomic Neuropathy Type IV (HSAN IV)," *Hum. Mutat.*, 2017.
- [144] N. Verpoorten *et al.*, "Novel frameshift and splice site mutations in the neurotrophic tyrosine kinase receptor type 1 gene (NTRK1) associated with hereditary sensory neuropathy type IV," *Neuromuscul. Disord.*, vol. 16, no. 1, pp. 19–25, 2006.
- [145] R. Altassan *et al.*, "Exome sequencing identifies novel NTRK1 mutations in patients with HSAN-IV phenotype," *Am. J. Med. Genet. Part A*, vol. 173, no. 4, pp. 1009–1016, 2017.
- [146] M. L. Franco *et al.*, "Mutations in TrkA causing congenital insensitivity to pain with anhidrosis (CIPA) induce misfolding, aggregation, and mutation-dependent neurodegeneration by dysfunction of the autophagic flux," *J. Biol. Chem.*, 2016.
- [147] M. A. McTigue *et al.*, "Crystal structure of the kinase domain of human vascular endothelial growth factor receptor 2: A key enzyme in angiogenesis," *Structure*, vol. 7, no. 3, pp. 319–330, 1999.
- [148] K. . Pajusola, O. . Aprelikova, G. . Pelicci, H. . Weich, L. . Claesson-Welsh, and K. . Alitalo, "Signalling properties of FLT4, a proteolytically processed receptor tyrosine kinase related to two VEGF receptors," *Oncogene*, 1994.
- [149] J. Kendrew *et al.*, "An Antibody Targeted to VEGFR-2 Ig Domains 4-7 Inhibits VEGFR-2 Activation and VEGFR-2-Dependent Angiogenesis without Affecting Ligand Binding," *Mol. Cancer Ther.*, vol. 10, no. 5, pp. 770–783, 2011.
- [150] D. Dell'Era Dosch and K. Ballmer-Hofer, "Transmembrane domain-mediated orientation of receptor monomers in active VEGFR-2 dimers," *FASEB J.*, vol. 24, no. 1, pp. 32–38, 2010.
- [151] C. Ruch, G. Skiniotis, M. O. Steinmetz, T. Walz, and K. Ballmer-Hofer, "Structure of a VEGF-VEGF receptor complex determined by electron microscopy," *Nat. Struct. Mol. Biol.*, vol. 14, no. 3, pp. 249–250, 2007.
- [152] C. A. C. Hyde *et al.*, "Targeting extracellular domains D4 and D7 of vascular endothelial growth factor receptor 2 reveals allosteric receptor regulatory sites.," *Mol. Cell. Biol.*, vol. 32, no. 19, pp. 3802–13, 2012.
- [153] K. Matsumoto *et al.*, "Prognostic Significance of Plasma Placental Growth Factor Levels in Renal Cell

- Cancer: An Association with Clinical Characteristics and Vascular Endothelial Growth Factor Levels," *Anticancer Res.*, vol. 23, no. 6 D, pp. 4953–4958, 2003.
- [154] S. A. Cunningham, M. P. Arrate, T. A. Brock, and M. N. Waxham, "Interactions of FLT-1 and KDR with phospholipase C  $\gamma$ : Identification of the phosphotyrosine binding sites," *Biochem. Biophys. Res. Commun.*, vol. 240, no. 3, pp. 635–639, 1997.
- [155] C. J. Hastie, H. J. McLauchlan, and P. Cohen, "Assay of protein kinases using radiolabeled ATP: A protocol," *Nat. Protoc.*, 2006.
- [156] Y. Li, W. Xie, and G. Fang, "Fluorescence detection techniques for protein kinase assay," *Anal. Bioanal. Chem.*, 2008.
- [157] F. Sizaire and M. Tramier, "FRET-Based Biosensors: Genetically Encoded Tools to Track Kinase Activity in Living Cells," in *Protein Phosphorylation*, 2017.
- [158] M. R. Clutter, G. C. Heffner, P. O. Krutzik, K. L. Sachen, and G. P. Nolan, "Tyramide signal amplification for analysis of kinase activity by intracellular flow cytometry," *Cytom. Part A*, 2010.
- [159] H. Steen, J. A. Jebanathirajah, J. Rush, N. Morrice, and M. W. Kirschner, "Phosphorylation analysis by mass spectrometry: Myths, facts, and the consequences for qualitative and quantitative measurements," *Mol. Cell. Proteomics*, vol. 5, no. 1, pp. 172–181, 2006.
- [160] A. Callegari, S. Luin, L. Marchetti, A. Duci, A. Cattaneo, and F. Beltram, "Single particle tracking of acyl carrier protein (ACP)-tagged TrkA receptors in PC12nr5 cells," *J. Neurosci. Methods*, vol. 204, no. 1, pp. 82–86, 2012.
- [161] L. Marchetti *et al.*, "Ligand signature in the membrane dynamics of single TrkA receptor molecule:file:///C:/Users/ramodeo/Desktop/immagini\_papers/bibliografia/1-s2.0-S0022283612006456-main.pdfules," *J. Cell Sci.*, vol. 126, no. 19, pp. 4445–4456, 2013.
- [162] L. Marchetti *et al.*, "Ligand signature in the membrane dynamics of single TrkA receptor molecules," *J. Cell Sci.*, vol. 126, no. 19, pp. 4445–4456, 2013.
- [163] I. Chung, R. Akita, R. Vandlen, D. Toomre, J. Schlessinger, and I. Mellman, "Spatial control of EGF receptor activation by reversible dimerization on living cells.," *Nature*, 2010.
- [164] G. S. Ali, K. V. S. K. Prasad, I. Day, and A. S. N. Reddy, "Ligand-dependent reduction in the membrane mobility of Flagellin sensitive2, an Arabidopsis receptor-like kinase," *Plant Cell Physiol.*, vol. 48, no. 11, pp. 1601–1611, 2007.
- [165] P. W. Winter, A. K. Van Orden, D. A. Roess, and B. G. Barisas, "Actin-dependent clustering of insulin receptors in membrane microdomains," *Biochim. Biophys. Acta - Biomembr.*, vol. 1818, no. 3, pp. 467–473, 2012.
- [166] K. G. N. Suzuki, R. S. Kasai, T. K. Fujiwara, and A. Kusumi, *Single-Molecule Imaging of Receptor-Receptor*

*Interactions*, 1st ed., vol. 117. Elsevier Inc., 2013.

- [167] I. Barde *et al.*, “Efficient control of gene expression in the hematopoietic system using a single Tet-on inducible lentiviral vector,” *Mol. Ther.*, 2006.
- [168] F. Gobbo, F. Bonsignore, R. Amodeo, A. Cattaneo, and L. Marchetti, “Site-specific direct labeling of neurotrophins and their receptors: From biochemistry to advanced imaging applications,” in *Methods in Molecular Biology*, vol. 1727, 2018, pp. 295–314.
- [169] L. Marchetti *et al.*, “Fast-diffusing p75 NTR monomers support apoptosis and growth cone collapse by neurotrophin ligands,” *Proc. Natl. Acad. Sci.*, 2019.
- [170] M. J. Hinner and K. Johnsson, “How to obtain labeled proteins and what to do with them,” *Curr. Opin. Biotechnol.*, vol. 21, no. 6, pp. 766–776, 2010.
- [171] U. Kubitscheck, O. Kuckmann, T. Kues, and R. Peters, “Imaging and Tracking of Single GFP Molecules in Solution,” *Biophys. J.*, vol. 78, no. 4, pp. 2170–2179, 2000.
- [172] T. De Nadai *et al.*, “Precursor and mature NGF live tracking: One versus many at a time in the axons,” *Sci. Rep.*, vol. 6, no. February, pp. 1–12, 2016.
- [173] P. Di Matteo, M. Calvello, S. Luin, L. Marchetti, and A. Cattaneo, “An Optimized Procedure for the Site-Directed Labeling of NGF and proNGF for Imaging Purposes,” *Front. Mol. Biosci.*, vol. 4, no. February, pp. 1–9, 2017.
- [174] N. Johnsson, N. George, and K. Johnsson, “Protein chemistry on the surface of living cells,” *ChemBioChem*, 2005.
- [175] K. Kisler, “Fluorescently-Labeled Estradiol Internalization and Membrane Trafficking in Live N-38 Neuronal Cells Visualized with Total Internal Reflection Fluorescence Microscopy,” *J. Steroids Horm. Sci.*, 2013.
- [176] I. Chung, “Optical measurement of receptor tyrosine kinase oligomerization on live cells,” *Biochim. Biophys. Acta - Biomembr.*, vol. 1859, no. 9, pp. 1436–1444, 2017.
- [177] A. Yildiz, J. N. Forkey, S. A. Mckinney, T. Ha, Y. E. Goldman, and P. R. Selvin, “Myosin V Walks Hand-Over-Hand : Single Fluorophore Imaging with 1.5-nm Localization,” *Science (80-. )*, vol. 300, no. 5628, pp. 2061–2065, 2003.
- [178] C. Manzo and M. F. Garcia-Parajo, “A review of progress in single particle tracking: From methods to biophysical insights,” *Reports Prog. Phys.*, vol. 78, no. 12, p. 124601, 2015.
- [179] M. J. Saxton and K. Jacobson, “SINGLE-PARTICLE TRACKING:Applications to Membrane Dynamics,” *Annu. Rev. Biophys. Biomol. Struct.*, 2002.
- [180] K. Burnecki, E. Kepten, Y. Garini, G. Sikora, and A. Weron, “Estimating the anomalous diffusion exponent for single particle tracking data with measurement errors - An alternative approach,” *Nat. Publ. Gr.*, no. May, pp. 1–11, 2015.

- [181] H. Ewers, A. E. Smith, I. F. Sbalzarini, H. Lilie, P. Koumoutsakos, and A. Helenius, "Single-particle tracking of murine polyoma virus-like particles on live cells and artificial membranes.," *Proc. Natl. Acad. Sci. USA*, 2005.
- [182] L. Marchetti, S. Luin, F. Bonsignore, T. de Nadai, F. Beltram, and A. Cattaneo, "Ligand-induced dynamics of neurotrophin receptors investigated by single-molecule imaging approaches," *Int. J. Mol. Sci.*, vol. 16, no. 1, pp. 1949–1979, 2015.
- [183] L. Marchetti *et al.*, "Site-specific labeling of neurotrophins and their receptors via short and versatile peptide tags," *PLoS One*, vol. 9, no. 11, pp. 1–18, 2014.
- [184] M. Odawara *et al.*, "Human Diabetes Associated with a Mutation in the Tyrosine Kinase Domain of the Insulin Receptor Akanuma , Fumimaro Takaku , Simeon I . Taylor and Masato Kasuga Published by : American Association for the Advancement of Science Stable URL : <http://www.jsto>," 2016.
- [185] K. A. E. Stenberg, P. T. Riikonen, and M. Vihinen, "KinMutBase, a database of human disease-causing protein kinase mutations," *Nucleic Acids Res.*, vol. 27, no. 1, pp. 362–364, 1999.
- [186] M. V. Chao, "Neurotrophins and their receptors: A convergence point for many signalling pathways," *Nat. Rev. Neurosci.*, vol. 4, no. 4, pp. 299–309, 2003.
- [187] A. W. Harrington and D. D. Ginty, "Long-distance retrograde neurotrophic factor signalling in neurons," vol. 14, no. March, pp. 177–187, 2013.
- [188] A. Vaishnavi, A. T. Le, and R. C. Doebele, "TRKing down an old oncogene in a new era of targeted therapy," *Cancer Discovery*. 2015.
- [189] S. Capsoni, "From genes to pain: nerve growth factor and hereditary sensory and autonomic neuropathy type V," *Eur. J. Neurosci.*, 2014.
- [190] M. E. Cunningham and L. A. Greene, "A function – structure model for NGF-activated TRK," vol. 17, no. 24, pp. 7282–7293, 1998.
- [191] R. A. Segal *et al.*, "Differential utilization of Trk autophosphorylation sites," *J. Biol. Chem.*, vol. 271, no. 33, pp. 20175–20181, 1996.
- [192] J. Biarc, R. J. Chalkley, A. L. Burlingame, and R. A. Bradshaw, "Dissecting the roles of tyrosines 490 and 785 of TrkA protein in the induction of downstream protein phosphorylation using chimeric receptors," *J. Biol. Chem.*, vol. 288, no. 23, pp. 16606–16618, 2013.
- [193] N. Inagaki, H. Thoenen, and D. Lindholm, "TrkA Tyrosine Residues Involved in NGF-induced Neurite Outgrowth of PC12 Cells," *Eur. J. Neurosci.*, vol. 7, no. 6, pp. 1125–1133, 1995.
- [194] A. Obermeier, H. Halfter, K. H. Wiesmüller, G. Jung, J. Schlessinger, and A. Ullrich, "Tyrosine 785 is a major determinant of Trk--substrate interaction.," *EMBO J.*, vol. 12, no. 3, pp. 933–41, 1993.
- [195] F. Gobbo, F. Bonsignore, R. Amodio, A. Cattaneo, and L. Marchetti, "Site-Specific Direct Labeling of

Neurotrophins Imaging Applications," *Methods Mol. Biol.*, vol. 1727, pp. 295–314, 2018.

- [196] S. Jing, P. Tapley, and M. Barbacid, "Nerve growth factor mediates signal transduction through trk homodimer receptors," *Neuron*, vol. 9, no. 6, pp. 1067–1079, 1992.
- [197] R. M. Stephens, D. M. Loeb, T. D. Copeland, T. Pawson, L. A. Greene, and D. R. Kaplan, "Trk receptors use redundant signal transduction pathways involving SHC and PLC- $\gamma$ 1 to mediate NGF responses," *Neuron*, vol. 12, no. 3, pp. 691–705, 1994.
- [198] H. Yano, F. Cong, R. B. Birge, S. P. Goff, and M. V. Chao, "Association of the Abl tyrosine kinase with the Trk nerve growth factor receptor," *J. Neurosci. Res.*, 2000.
- [199] H. Yano *et al.*, "Association of Trk neurotrophin receptors with components of the cytoplasmic dynein motor.," *J. Neurosci.*, 2001.
- [200] L. Harel *et al.*, "CCM2 Mediates Death Signaling by the TrkA Receptor Tyrosine Kinase," *Neuron*, 2009.
- [201] J. Jullien, V. Guili, E. A. Derrington, J. L. Darlix, L. F. Reichardt, and B. B. Rudkin, "Trafficking of TrkA-green fluorescent protein chimerae during nerve growth factor-induced differentiation," *J. Biol. Chem.*, vol. 278, no. 10, pp. 8706–8716, 2003.
- [202] S. J. Dixon, J. I. S. MacDonald, K. N. Robinson, C. J. Kubu, and S. O. Meakin, "Trk receptor binding and neurotrophin/fibroblast growth factor (FGF)-dependent activation of the FGF receptor substrate (FRS)-3," *Biochim. Biophys. Acta - Mol. Cell Res.*, vol. 1763, no. 4, pp. 366–380, 2006.
- [203] J. C. Arevalo *et al.*, "Cell survival through Trk neurotrophin receptors is differentially regulated by ubiquitination," *Neuron*, vol. 50, no. 4, pp. 549–559, 2006.
- [204] L. C. Schecterson *et al.*, "Trk activation in the secretory pathway promotes Golgi fragmentation," *Mol. Cell. Neurosci.*, vol. 43, no. 4, pp. 403–413, 2010.
- [205] R. Amodeo *et al.*, "BBA - Molecular Cell Research Molecular insight on the altered membrane trafficking of TrkA kinase dead mutants," *BBA - Mol. Cell Res.*, vol. 1867, no. 2, p. 118614, 2020.
- [206] A. Disanza, E. Frittoli, A. Palamidessi, and G. Scita, "Endocytosis and spatial restriction of cell signaling," *Mol. Oncol.*, vol. 3, no. 4, pp. 280–296, 2009.
- [207] J. Jullien, V. Guili, E. A. Derrington, J. L. Darlix, L. F. Reichardt, and B. B. Rudkin, "Trafficking of TrkA-green fluorescent protein chimerae during nerve growth factor-induced differentiation," *J. Biol. Chem.*, 2003.
- [208] T. Bertrand *et al.*, "The Crystal Structures of TrkA and TrkB Suggest Key Regions for Achieving Selective Inhibition," *J. Mol. Biol.*, vol. 423, no. 3, pp. 439–453, 2012.
- [209] A. Kusumi, K. G. N. Suzuki, R. S. Kasai, K. Ritchie, and T. K. Fujiwara, "Hierarchical mesoscale domain organization of the plasma membrane," *Trends Biochem. Sci.*, vol. 36, no. 11, pp. 604–615, 2011.
- [210] W. S. Trimble and S. Grinstein, "Barriers to the free diffusion of proteins and lipids in the plasma membrane," *J. Cell Biol.*, vol. 208, no. 3, pp. 259–271, 2015.

- [211] K. G. N. Suzuki, T. K. Fujiwara, F. Sanematsu, R. Iino, M. Edidin, and A. Kusumi, "GPI-anchored receptor clusters transiently recruit Lyn and G?? for temporary cluster immobilization and Lyn activation: Single-molecule tracking study 1," *J. Cell Biol.*, vol. 177, no. 4, pp. 717–730, 2007.
- [212] A. Kusumi and Y. Sako, "Cell surface organization by the membrane skeleton Akihiro Kusumi \* and Yasushi Sakot," *Cell*, vol. 8, no. 4, pp. 566–574, 1996.
- [213] B. Anta *et al.*, "Ubiquitin-specific protease 36 (USP36) controls neuronal precursor cell-expressed developmentally down-regulated 4-2 (Nedd4-2) actions over the neurotrophin receptor TrkA and potassium voltage-gated channels 7.2/3 (kv7.2/3)," *J. Biol. Chem.*, vol. 291, no. 36, pp. 19132–19145, 2016.
- [214] A. C. Carrera, K. Alexandrov, and T. M. Roberts, "The conserved lysine of the catalytic domain of protein kinases is actively involved in the phosphotransfer reaction and not required for anchoring ATP.," *Proc. Natl. Acad. Sci.*, vol. 90, no. 2, pp. 442–446, 1993.
- [215] F. Lallemand and P. Ernfors, "Molecular interactions underlying the specification of sensory neurons," *Trends in Neurosciences*. 2012.
- [216] S. Mardy, "Congenital insensitivity to pain with anhidrosis (CIPA): effect of TRKA (NTRK1) missense mutations on autophosphorylation of the receptor tyrosine kinase for nerve growth factor," *Hum. Mol. Genet.*, vol. 10, no. 3, pp. 179–188, 2001.
- [217] S. R. Hubbard, L. Wei, and W. A. Hendrickson, "Crystal structure of the tyrosine kinase domain of the human insulin receptor," *Nature*, 1994.
- [218] S. R. Hubbard, "Crystal structure of the activated insulin receptor tyrosine kinase in complex with peptide substrate and ATP analog," *EMBO J.*, 1997.
- [219] M. E. Cunningham and L. A. Greene, "A function-structure model for NGF-activated TRK," *EMBO J.*, 1998.
- [220] C. Miranda *et al.*, "Novel pathogenic mechanisms of congenital insensitivity to pain with anhidrosis genetic disorder unveiled by functional analysis of neurotrophic tyrosine receptor kinase type 1/nerve growth factor receptor mutations," *J. Biol. Chem.*, vol. 277, no. 8, pp. 6455–6462, 2002.
- [221] F. Gobbo, F. Bonsignore, R. Amodio, A. Cattaneo, and L. Marchetti, "Site-Specific Direct Labeling of Neurotrophins Imaging Applications," vol. 1727, pp. 295–314.
- [222] D. L. Baker *et al.*, "Analysis of Nerve Growth Factor Receptor Expression in Human Neuroblastoma and Neuroepithelioma Cell Lines," *Cancer Res.*, 1989.
- [223] T. M. Gomez and P. C. Letourneau, "Actin dynamics in growth cone motility and navigation," *Journal of Neurochemistry*. 2014.
- [224] Y. Ren and D. M. Suter, "Increase in Growth Cone Size Correlates with Decrease in Neurite Growth Rate," *Neural Plast.*, vol. 2016, pp. 20–22, 2016.

- [225] S. Maday, "Mechanisms of neuronal homeostasis: Autophagy in the axon," *Brain Res.*, vol. 1649, pp. 143–150, 2016.
- [226] K. Mnich, L. A. Carleton, E. T. Kavanagh, K. M. Doyle, A. Samali, and A. M. Gorman, "Nerve growth factor-mediated inhibition of apoptosis post-caspase activation is due to removal of active caspase-3 in a lysosome-dependent manner," *Cell Death Dis.*, vol. 5, no. 5, pp. e1202-13, 2014.
- [227] T. W. Bodnarchuk, S. Napper, N. Rapin, V. Misra, and M. Á. Brna, "Mechanism for the induction of cell death in ONS-76 medulloblastoma cells by Zhangfei / CREB-ZF," pp. 485–501, 2012.
- [228] S. K. Kaasinen, L. Harvey, A. J. Reynolds, and I. A. Hendry, "Autophagy generates retrogradely transported organelles : a hypothesis," vol. 26, pp. 625–634, 2008.
- [229] Y. Kabeya, "LC3, a mammalian homologue of yeast Apg8p, is localized in autophagosome membranes after processing," *EMBO J.*, 2000.
- [230] D. C. Rubinsztein, T. Shpilka, and Z. Elazar, "Mechanisms of autophagosome biogenesis," *Current Biology*. 2012.
- [231] R. A. Frake *et al.*, "Autophagy and neurodegeneration Find the latest version : Autophagy and neurodegeneration," *J. Clin. Invest.*, vol. 125, no. 1, pp. 65–74, 2015.
- [232] H. U. Saragovi *et al.*, "A TrkA-selective , Fast Internalizing Nerve Growth Factor-Antibody Complex Induces Trophic but Not Neuritogenic Signals \*," vol. 273, no. 52, pp. 34933–34940, 1998.
- [233] J. B. Grinspan, S. N. Mueller, and E. M. Levine, "Bovine endothelial cells transformed in vitro by benzo(a)pyrene," *J. Cell. Physiol.*, 1983.
- [234] W. T. Jackson *et al.*, "Subversion of cellular autophagosomal machinery by RNA viruses," *PLoS Biol.*, 2005.
- [235] S. H. Green, R. E. Rydel, J. L. Connolly, and L. A. Greene, "PC12 cell mutants that possess low- but not high-affinity nerve growth factor receptors neither respond to nor internalize nerve growth factor," *J. Cell Biol.*, 1986.
- [236] L. Marchetti *et al.*, "Ligand signature in the membrane dynamics of single TrkA receptor molecules," *J. Cell Sci.*, vol. 126, no. 19, pp. 4445–4456, 2013.
- [237] J. G. Kettle *et al.*, "Discovery of N-(4-([5-Fluoro-7-(2-methoxyethoxy)quinazolin-4-yl]amino}phenyl)-2-[4-(propan-2-yl)-1 H-1,2,3-triazol-1-yl]acetamide (AZD3229), a Potent Pan-KIT Mutant Inhibitor for the Treatment of Gastrointestinal Stromal Tumors," *J. Med. Chem.*, vol. 61, no. 19, pp. 8797–8810, 2018.
- [238] J. M. Word *et al.*, "Visualizing and quantifying molecular goodness-of-fit: Small-probe contact dots with explicit hydrogen atoms," *J. Mol. Biol.*, vol. 285, no. 4, pp. 1711–1733, 1999.
- [239] G. Vriend, "WHAT IF: A molecular modeling and drug design program," *J. Mol. Graph.*, 1990.
- [240] S. J. Fleishman *et al.*, "of Influenza Hemagglutinin," *Science (80- )*, vol. 979, no. May, pp. 816–822, 2011.
- [241] K. Lindorff-Larsen *et al.*, "Improved side-chain torsion potentials for the Amber ff99SB protein force field,"

*Proteins Struct. Funct. Bioinforma.*, vol. 78, no. 8, pp. 1950–1958, 2010.

- [242] R. B. Best and G. Hummer, “Optimized molecular dynamics force fields applied to the helix-coil transition of polypeptides,” *J. Phys. Chem. B*, 2009.
- [243] M. J. Abraham *et al.*, “Gromacs: High performance molecular simulations through multi-level parallelism from laptops to supercomputers,” *SoftwareX*, vol. 1–2, pp. 19–25, 2015.
- [244] N. D. Gagunashvili, “Chi-square goodness of fit tests for weighted histograms. Review and improvements,” *J. Instrum.*, vol. 10, no. 5, 2015.
- [245] M. Fernández-Suárez and A. Y. Ting, “Fluorescent probes for super-resolution imaging in living cells,” *Nature Reviews Molecular Cell Biology*. 2008.
- [246] H. Li and J. C. Vaughan, “Switchable Fluorophores for Single-Molecule Localization Microscopy,” *Chem. Rev.*, vol. 118, no. 18, pp. 9412–9454, 2018.
- [247] J. B. Grimm *et al.*, “Bright photoactivatable fluorophores for single-molecule imaging.,” *Nat. Methods*, vol. 13, no. 12, pp. 985–988, 2016.
- [248] Q. Zheng *et al.*, “Ultra-stable organic fluorophores for single-molecule research,” *Chem. Soc. Rev.*, vol. 43, no. 4, pp. 1044–1056, 2014.
- [249] C. Jing and V. W. Cornish, “Living Cells,” *Lancet*, vol. 294, no. 7627, p. 943, 2003.
- [250] A. Keppler, S. Gendreizig, T. Gronemeyer, H. Pick, H. Vogel, and K. Johnsson, “A general method for the covalent labeling of fusion proteins with small molecules in vivo,” *Nat. Biotechnol.*, 2003.
- [251] A. Gautier *et al.*, “An Engineered Protein Tag for Multiprotein Labeling in Living Cells,” *Chem. Biol.*, vol. 15, no. 2, pp. 128–136, 2008.
- [252] K. W. Teng *et al.*, “Labeling proteins inside living cells using external fluorophores for microscopy,” *Elife*, 2016.
- [253] L. D. Hughes *et al.*, “Choose Your Label Wisely : Water-Soluble Fluorophores Often Interact with Lipid Bilayers,” vol. 9, no. 2, 2014.
- [254] P. J. Bosch *et al.*, “Evaluation of fluorophores to label SNAP-Tag fused proteins for multicolor single-molecule tracking microscopy in live cells,” *Biophys. J.*, vol. 107, no. 4, pp. 803–814, 2014.
- [255] Z. Zhang, D. Yomo, and C. Gradinaru, “Biochimica et Biophysica Acta Choosing the right fluorophore for single-molecule fluorescence studies in a lipid environment,” *BBA - Biomembr.*, vol. 1859, no. 7, pp. 1242–1253, 2017.
- [256] D. Convertino *et al.*, “Graphene promotes axon elongation through local stall of Nerve Growth Factor signaling endosomes,” 2020.
- [257] M. Vilar, “Structural Characterization of the p75 Neurotrophin Receptor: A Stranger in the TNFR Superfamily,” in *Vitamins and Hormones*, 2017.

- [258] V. Damioli, A. Salvadori, G. P. Beretta, C. Ravelli, and S. Mitola, "Multi-physics interactions drive VEGFR2 relocation on endothelial cells," *Sci. Rep.*, 2017.
- [259] H. M. Jopling, G. J. Howell, N. Gamper, and S. Ponnambalam, "The VEGFR2 receptor tyrosine kinase undergoes constitutive endosome-to-plasma membrane recycling," *Biochem. Biophys. Res. Commun.*, vol. 410, no. 2, pp. 170–176, 2011.
- [260] B. L. Hempstead, D. Martin-Zanca, D. R. Kaplan, L. F. Parada, and M. V. Chao, "High-affinity NGF binding requires coexpression of the trk proto-oncogene and the low-affinity NGF receptor," *Nature*, 1991.
- [261] C. Mazzotti *et al.*, "The atypical receptor CCRL2 (C-C Chemokine Receptor-Like 2) does not act as a decoy receptor in endothelial cells," *Front. Immunol.*, 2017.